ABSTRACT

HOU, GUOJING. Development of Sensor Physics for a Nuclear Oil Well Logging Tool. (Under the direction of Robin P. Gardner.)

In the oil industry, oil well logging is a practice that utilizes a measuring apparatus to characterize the rock formations traversed by the measuring device against the depth of the oil well. Different well logging devices make uses of different physical principles, such as acoustics, nuclear physics, electrical science, etc., to measure the properties of the rocks and their contained fluids. One unique type of logging is geochemical logging, which estimates the elemental compositions of the rock matrices by measuring the gamma spectral responses from the rocks, stimulated by energetic neutrons. Such a tool measures the gammas produced by (n, γ) reactions, natural radiations, decay gammas of radioactive isotopes produced by neutron activation, and sometimes (n, n'γ) reactions. Since its introduction in late 1980s, geochemical logging has become an important means for log analysts to understand the mineralogy of the oil wells.

The core components of a geochemical logging tool include a neutron source and a gamma spectroscopy detector. In recent years, the successful commercialization of $LaBr_3$ scintillation crystal illuminates a new possibility for the industry. The $LaBr_3$ crystal has some favorable properties compared to the NaI and BGO crystals, which are commonly used. It has better energy resolution and better resolution temperature stability than the BGO detector, as well as higher density than the NaI detector.

This dissertation is devoted to the sensor physics of a geochemical well logging tool, which is equipped with a D-T pulsed neutron generator and a $LaBr_3$ detector. In this study, the logging tool is characterized by developing a full set of elemental standards and elemental sensitivity factors. In addition, a numerical method based on the Levenberg-Marquardt method is also developed. The standards, sensitivity factors, and deconvolution method constitute a full tool set that allows calculations of elemental weight concentrations from the tool measurements.

Preliminary tests show promising results. The spectral deconvolution algorithm proved to be capable of efficiently deconvolving the composite spectra, while accounting for both spectral misalignments and resolution degradations. When applied in conjunction with the elemental standards and the sensitivity factors, the algorithm calculated the elemental dry weights with good accuracy.

© Copyright 2017 by Guojing Hou

All Rights Reserved

Development of Sensor Physics for a Nuclear Oil Well Logging Tool

by
Guojing Hou

A dissertation submitted to the Graduate Faculty of
North Carolina State University
in partial fulfillment of the
requirements for the Degree of
Doctor of Philosophy

Nuclear Engineering

Raleigh, North Carolina

2017

APPROVED BY:

Richard R. Pemper	Dmitriy Y. Anistratov
Yousry Y. Azmy	Ralph C. Smith

Robin P. Gardner
Chair of Advisory Committee

BIOGRAPHY

Guojing Hou was born and raised in Tianjin, China. He received a Bachelor of Engineering in Nuclear Engineering in 2008. In the summer of 2012, he began pursuing his doctorate degree under the direction of Dr. Robin P. Gardner at NC State University.

ACKNOWLEDGEMENTS

I would like to thank my advisor, Dr. Gardner, for his mentorship, continuous support, and for leading me into the wonderful field of radiation detection. Without him, I would have had no chance of completing this project. I would also like to thank Dr. Pemper for his guidance during every step of this project. It has been my privilege and great fortune to have been able to work with them. As scientists, they have set extraordinarily high standards, which I will strive to reach for the rest of my life. I am also highly appreciative of Dr. Anistratov, Dr. Azmy, and Dr. Smith for their many insightful suggestions on this project.

My sincere gratitude also goes to my friends, with whom I have shared many unforgettable memories.

Finally, I would like to thank my parents and wife, who have always been unconditionally supportive.

TABLE OF CONTENTS

LIST OF TABLES . . . . . **vi**

LIST OF FIGURES . . . . . **vii**

Chapter 1 Introduction **1**
1.1 Background 1
1.2 Overview 3

Chapter 2 Nuclear Reactions **7**
2.1 Neutron transport 7
2.1.1 Elastic scattering 7
2.1.2 Neutron capture (n, γ) 8
2.1.3 Inelastic scattering (n, n'γ) 8
2.1.4 Probabilities of reactions 10
2.2 Photon transport and detector Response 10
2.2.1 Photon reactions 10
2.2.2 Probabilities of reactions 14
2.2.3 Detector response 14
2.3 Data Sources 22

Chapter 3 Spectral Acquisition and Preprocessing **25**
3.1 Spectral acquisition 25
3.1.1 Neutron source 25
3.1.2 Measuring spectra 26
3.2 Noticeable spectral features 29
3.3 Spectra preprocessing 37
3.3.1 Alignment 37
3.3.2 Background subtraction 47

Chapter 4 Spectral Analysis **50**
4.1 Overview 50
4.2 Elemental standards 51
4.2.1 Definition 51
4.2.2 Generation 53
4.2.3 Considerations 56
4.3 Deconvolution algorithms 58
4.3.1 Overview 58
4.3.2 Weighted linear least squares 60
4.3.3 Non-negative least squares 64
4.3.4 Levenberg-Marquardt 66

4.3.5 Modifications of LM for spectral deconvolution 72
4.4 Elemental concentrations 78
4.4.1 Sensitivity factor 78
4.4.2 Oxide closure model 87

Chapter 5 Complete Example 91
5.1 Sample measurements 91
5.2 Spectral preprocessing 92
5.3 Spectral deconvolution 93
5.4 Weight calculation 95

Chapter 6 Discussion and Conclusions 100

BIBLIOGRAPHY 103

LIST OF TABLES

Table 1.1 Current geochemical well logging devices. 3

Table 2.1 Inelastic scattering threshold energies of isotopes commonly found in the earth formations. 9

Table 3.1 Peaks used for the alignment, and their centroids before and after the alignment. Based on these peaks, $M = 1.0678$, $A = -1.879$. . . 46

Table 4.1 Numerical results of the deconvolutions. 64
Table 4.2 Numerical results of the deconvolution of dolomite capture spectrum using different methods. 66
Table 4.3 XRF measurement of quartz+calcite sample 84
Table 4.4 Deconvolution results of the quartz + calcite sample. 87
Table 4.5 Mineral commonly associated with hydrocarbon-bearing formations 89
Table 4.6 Oxidation factors of elements commonly found in earth formations 90

Table 5.1 XRF analyzed elemental concentrations of the dolomite block. . . . 91
Table 5.2 Gain setting calibration parameters. 94
Table 5.3 Calculated capture elemental yields. 96
Table 5.4 Calculated inelastic elemental yields. 97
Table 5.5 Elemental concentrations of the formation matrix calculated using the capture standard. 98
Table 5.6 Elemental concentrations of the formation matrix calculated using the inelastic standard. 98
Table 5.7 Elemental concentrations of the formation matrix averaged over the capture and inelastic spectra. 99

LIST OF FIGURES

Figure 1.1 Block diagram of the Tool. 4
Figure 1.2 A prototype of the Tool. 4
Figure 1.3 Flow chart of data acquisition and processing of the Tool. 5

Figure 2.1 Level scheme of ^{28}Si, up to 6880 KeV[13]. 11
Figure 2.2 Ratios of microscopic cross sections of individual reactions to the total microscopic cross section of ^{28}Si. Cross section data extracted from ENDF data file[14]. 12
Figure 2.3 Maximum percentage of energy transferable to the recoil electron as a function of incident photon energy. 13
Figure 2.4 Macroscopic cross sections of $LaBr_3$ between 100 KeV and 20 MeV. Calculated based on NIST XCOM database. 15
Figure 2.5 Ratios of three types of photon reactions for $LaBr_3$ between 100 KeV and 20MeV. 15
Figure 2.6 Cross section of the geometry set up used for MCNP modeling. Figure shows a cross section perpendicular to the Y axis. 16
Figure 2.7 3D presentation of the geometry set up used for MCNP modeling. 17
Figure 2.8 MCNP F8 tally result of the geometry shown in Figure 2.6. 17
Figure 2.9 FWHM fitted to Equation 2.9 and Equation 2.10 respectively. The measurements are made using a $LaBr_3$ detector. 22
Figure 2.10 Energy spectrum as shown in Figure 2.8 broadened using realistic broadening parameters. 23

Figure 3.1 Firing sequence of the Tool. The yellow blocks represent the neutron emission sub-cycles of Period 1, the green block represents Period 2, and the purple block represent Period 3. 28
Figure 3.2 Count rate time spectrum of a water tank measurement. 28
Figure 3.3 Unprocessed gamma spectra of a water tank measurement shown in raw counts. 30
Figure 3.4 Unprocessed gamma spectra of a water tank measurement shown in count rates. 30
Figure 3.5 (n, p) reaction ratio of ^{16}O. Data from ENDF data files. 32
Figure 3.6 ^{16}N decay scheme. The chart also shows the energy levels and de-excitation gamma energies of ^{16}O. Data from ENSDF data files. 33
Figure 3.7 Background spectrum of a sandstone measurement. 34
Figure 3.8 Decay scheme of $^{28}_{13}$Al. Data from ENSDF data files. 34
Figure 3.9 (n, p) reaction ratio of ^{28}Si. Data from ENDF data files. 35
Figure 3.10 Background spectrum of an aluminum block measurement. 35

Figure 3.11 $^{138}_{57}$La β^- decays to $^{138}_{58}$Ce. The branching ratio is 34.4%. Data from ENSDF data files. 36
Figure 3.12 $^{138}_{57}$La electron capture decays to $^{138}_{56}$Ba. The branching ratio is 65.6%. Data from ENSDF data files. 37
Figure 3.13 Unprocessed capture spectra of two separate water tank measurements. 2216A and 2216B are measurement IDs. 38
Figure 3.14 The Gaussian filter used for smoothing the measurement spectrum. The FWHM$\approx$ 4.43. 39
Figure 3.15 Comparison of the raw capture spectrum of water tank measurement (2216A) and after the Gaussian filter is applied. 40
Figure 3.16 The background removal filter used for removing the positive component of the spectrum. 41
Figure 3.17 Comparison of the raw capture spectrum of water tank measurement (2216A) and after application of the Gaussian filter and background removal filters. 41
Figure 3.18 Figure 3.17 zoomed to channel 130 to channel 190 to show the details. 42
Figure 3.19 Water tank capture spectrum measurement zoomed to channel 130 to channel 190 showing shapes of the spectrum after each filter is applied. The dashed lines mark the three peaks identified by the algorithm in this range. 42
Figure 3.20 Oxygen peak of the capture spectrum of the water tank measurement fitted to Equation 3.2. 44
Figure 3.21 By definition, the i^{th} channel ranges from point $i-1$ to point i on the continuous scale. 45
Figure 3.22 Capture spectrum of sandstone with water borehole measurement before and after spectral alignment. The dotted lines indicate the peaks used for the alignment, and their centroids before and after the alignment. 47
Figure 3.23 Subtraction of the background radiation spectrum from the capture spectrum. The yellow circles highlight some significant changes after the subtraction. 49
Figure 3.24 Subtraction of the background radiation spectrum from the burst spectrum. 49

Figure 4.1 Overview of the spectral analysis process. 51
Figure 4.2 Comparison of Al capture standards measured under different environment. 52
Figure 4.3 Capture spectrum of a sandstone sample with water in the borehole. Spectrum has been aligned and background subtracted. . . . 55
Figure 4.4 Hydrogen capture standard. 55

Figure 4.5 Snapshot of the SpeStripping code. The blue curve is the capture spectrum of the sandstone measurement. The red curve is the hydrogen capture standard. The yellow curve is the residue curve after subtracting the H standard from the measurement, after the adjustments characterized by the parameters shown on top of the plot. 57
Figure 4.6 Elemental standards of (n, γ) capture reaction. The amplitudes are artificially adjusted to show the details of each standard. . . . 62
Figure 4.7 Comparison of measured dolomite capture spectrum and fit spectrum using two sets of standards. 'Limited Set' refers to the set with H, Ca, and Mg. 'w/ Interference' refers to the set with H, Ca, Mg, and Si, which is not present in the sample. 63
Figure 4.8 Iteration and convergence of τ calculated using LM method. . . . 68
Figure 4.9 Change of χ^2 in each iteration of the fitting shown in Figure 4.8. The red curve is χ^2 computed using different τ values between 5 and 14. 69
Figure 4.10 Iteration of fitting a normal distribution using the LM method. . . 70
Figure 4.11 χ^2 as a function of ω for the model $y = \sin(1.1 \cdot x)$. Multiple local minimum χ^2 exists between -10 and 10. Whether the LM fitting can find the global optimum ω depends on the initial guess. 71
Figure 4.12 Two artificially generated component spectra. 76
Figure 4.13 Comparison of the ideal composite spectrum, and the distorted and Poisson randomized composite spectrum. The ideal composite spectrum is Gaussian broadened by $\sigma = 3$, contracted by 5%, and shifted to the right by 5 channels to create the distorted spectrum. 76
Figure 4.14 Comparison of the distorted and randomized composite spectrum and the fitted spectrum. The reduced χ^2 of the deconvolution is 0.7, which suggests a good fit. 77
Figure 4.15 Comparison of the spectral deconvolution performed using the regular LM method and the modified LM method. The reduced χ^2 for both cases is ~ 15.1, with a difference of smaller than 10^{-3}. . . 79
Figure 4.16 Capture sensitivity factors of the Tool. 83
Figure 4.17 Inelastic sensitivity factors of the Tool. 83
Figure 4.18 Barrels used for calibration and characterizations. 84
Figure 4.19 Empty water tank. The hole in the middle extends deeper, so that the neutron generator and gamma detector portion of the logging tool can be positioned at the center of the sample barrel. 85
Figure 4.20 Logging tool and characterization barrel properly placed inside the tank. 85
Figure 4.21 Measurement and fit of the quartz + calcite sample. 86

Figure 5.1 Dolomite rock sample. 92

Figure 5.2 Raw measurements of the dolomite sample in water borehole. . . . 93
Figure 5.3 Raw measurements aligned to specification using parameters calculated in Table 5.2. 94
Figure 5.4 The net burst, capture, and inelastic spectra after background subtraction. 95
Figure 5.5 Deconvolution of the capture spectrum. Reduced $\chi^2 = 18.3$. . . . 96
Figure 5.6 Deconvolution of the inelastic spectrum. Reduced $\chi^2 = 13.3$. . . . 97

Chapter 1

Introduction

1.1 Background

This research involves developing a nuclear geochemical oil well logging device, which is a wireline logging tool used for open hole wells.

In the context of oil exploration, well logging refers to 'a recording against depth of any of the characteristics of the rock formations traversed by a measuring apparatus in the well-bore'[1]. The characteristics can be measured by retrieving samples of the rock formations from the borehole for lab analysis, or by utilizing logging devices and measuring the properties inside the borehole. Different types of logs are compiled, correlated, reviewed, and interpreted by professionals to assess the status of the oil well. The analysis results are then provided to the management as the basis for operational decisions. Well logs provide critical information regarding the status of an oil well. Each oil well may undergo several well logging runs throughout its entire life cycle. Well logging, as a general technique, is also utilized in fields other than oil exploration and production, such as uranium exploration.

Wireline logging is one of several major types of well logging, categorized by how the measurements are taken. A wireline logging tool is usually a long cylindrical device, attached to wires. The logging is performed by lowering one or a string of such tools down to the bottom of the borehole, and lifting up the tool(s) again. The measurement is usually taken when the tool is being pulled up through the well, but can also be taken when the tool is being lowered down into the well. The depth of the tool at each measurement point is controlled and monitored by a calibrated winch, to which the tool

is attached. The measured data is either sent back to the surface in real time, or stored on the device and retrieved at a later time. Wireline logging is performed after a borehole is drilled. Another type of logging is logging while drilling, or LWD for short. As the name implies, LWD is performed while a borehole is being drilled, as the LWD device is integrated to be part of the drilling collar. The data measured by the LWD tool can be stored on the device, sent back to the surface through drillpipe in real time, or via generating pulses in the well's mud.

The tool being developed and described in this dissertation ('the Tool') is a geochemical logging tool[2], meaning that it is specialized in measuring the elemental concentrations of the rock formations. A geochemical logging tool is essentially a prompt gamma neutron activation analysis (PGNAA) device, with some designs specifically facilitating the application environment of an oil well. This type of device is equipped with a neutron source and a gamma spectroscopy detector. The neutron source stimulates the rock formations by emitting high energy neutrons, and measures the gamma spectral responses of the formation. The two primary types of reactions are the (n, γ) neutron capture reaction, and the (n, n'γ) neutron inelastic scattering reaction. Both reactions release gamma photons whose energies are characteristic of the target nuclei. The spectrum is then analyzed for elemental contributions, which are further converted into elemental concentrations. Such elemental analysis is made possible by the fact that, 9 elements, namely oxygen, silicon, aluminum, iron, calcium, sodium, potassium, magnesium, and hydrogen, make 98.13% of the total mass of the earth crust[3][4].

In the industry, a few major oil service companies developed several types of geochemical logging devices. Table 1.1 lists the major geochemical tools and their technical parameters. Of the three tools, FLeX and Litho Scanner both use pulsed neutron generators as neutron source. Comparing to the Am-Be source which is used by the GEM tool, neutrons emitted from the PNG have much higher energy (14 MeV), which is enough for the target nuclei to undergo inelastic scattering reactions. This allows FLeX and Litho Scanner to directly measure the carbon concentration in the formation, which is important for deriving total organic carbon (TOC). In addition, the application of a controllable source also reduces the potential risks in storing, transporting, and using a radioactive source. On the other hand, using a chemical source considerably simplifies the electronics on the device.

FLeX and GEM both use BGO as the detector, whereas Litho Scanner uses $LaBr_3$.

Table 1.1 Current geochemical well logging devices.

	FLeX[5]	GEM[6]	Litho Scanner[7]
Company	Baker Hughes	Halliburton	Schlumberger
Commercial introduction	2006	2009	2012
Neutron source	PNG	Am-Be	PNG
Diameter	4.9 in	4.8 in	4.5 in
Detector	3-in BGO	3-in BGO	$LaBr_3$
Temperature rating	175°C	175°C	175°C
Pressure rating	20,000 psi	20,000 psi	20,000 psi
Logging speed	15-30 ft/min	15-30 ft/min	15-30 ft/min
Capture elements	Ca, Cl, Fe, Gd, H, Mg, S, Si, Ti	Ca, Cl, Fe, Gd, H, Mg, S, Si, Ti	Ca, Cl, Fe, Gd, H, Mg, Na, S, Si, Ti
Inelastic elements	Al, C, Mg, Si	N/A	Al, C, Ca, Fe, Mg, S, Si

Comparing to BGO, $LaBr_3$ is a relatively new crystal, as it was first introduced in 2001[8] and became commercially available in 2006[9]. $LaBr_3$ does not only have better energy resolution, it is also more resilient to higher temperature, and the resolution does not degrade as badly as BGO does. Some type of temperature control device has to be applied if a BGO detector is to be used in a high temperature environment. The only disadvantage of $LaBr_3$ is that it is not as dense as the BGO, which affected its detection efficiency, but still, its denser than NaI.

1.2 Overview

The Tool uses a D-T neutron generator as the neutron source and a $LaBr_3$ crystal as the detector. Figure 1.1 schematically shows the major components of the tool. In addition to the detector and the neutron source, another important component is a neutron reflector made of tungsten. This reflector prevents the energetic neutrons from entering the detector without reacting with the substance outside the tool. Figure 1.2 shows a photo of a prototype of the Tool.

This research focuses on the data processing of the Tool. The data acquisition and processing procedure for the Tool is illustrated in a flow chart shown in Figure 1.3.

In the flow chart:

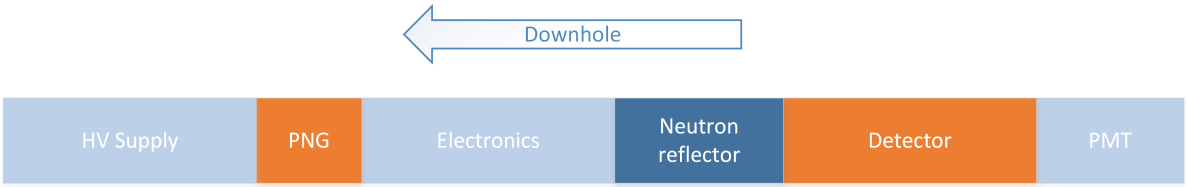

Figure 1.1 Block diagram of the Tool.

Figure 1.2 A prototype of the Tool.

1. 'Initialization' refers to the initialization of the device control and data processing software, which loads a variety of device parameters. The most important ones are the neutron firing sequence, and the predetermined elemental characteristic gamma standard spectra, or 'elemental standards' for short. These are illustrated in Chapter 3 and Chapter 4.

2. 'Gamma spectrum measurements' refers to the generation of two gamma energy spectra: net neutron capture gamma spectrum, and net neutron inelastic scattering gamma spectrum. Three gamma spectra are actually measured alternately in order to generate the two aforementioned spectra: neutron capture gamma spectrum, neutron burst gamma spectrum, and background spectrum. The fundamental physics are briefly illustrated in Chapter 2. The generation of the two final spectra are elaborated in Chapter 3.

3. 'Spectral analysis for elemental yields' refers to the step that numerically analyzes the capture and inelastic spectra. The two spectra are individually resolved using the predetermined elemental standards to estimate the number of gamma counts each element contributes to each spectrum. The numerical method used for the deconvolution is illustrated in Chapter 4.

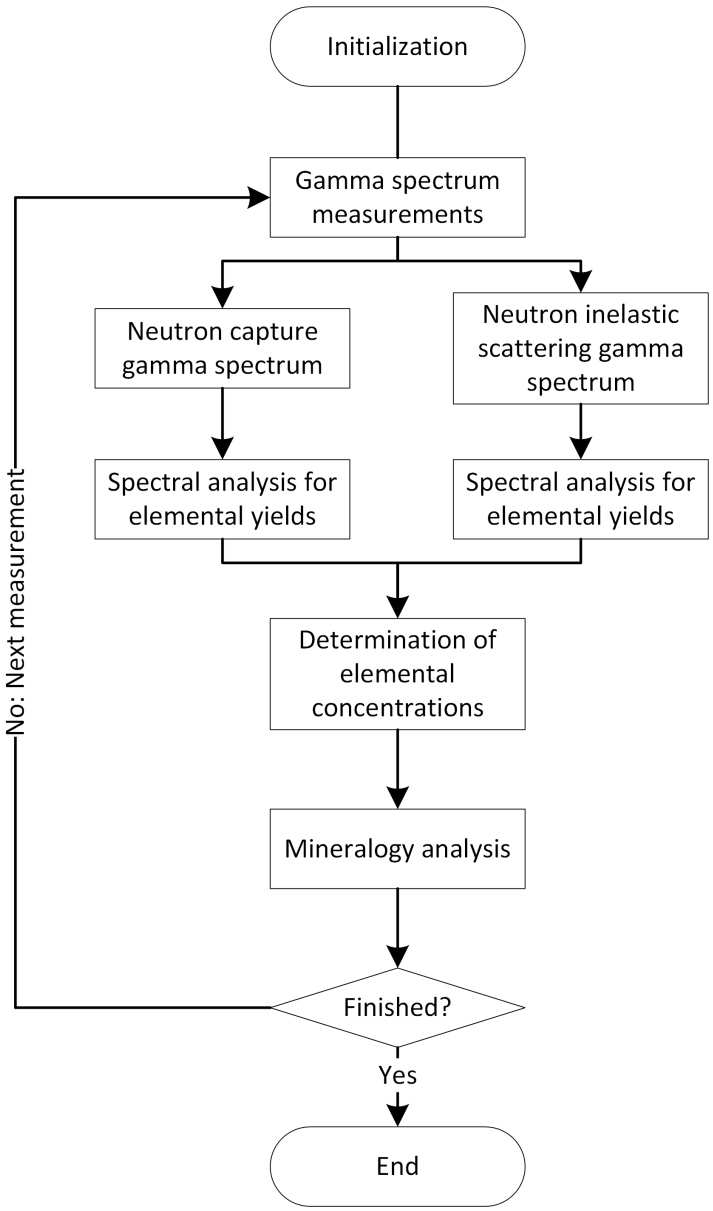

Figure 1.3 Flow chart of data acquisition and processing of the Tool.

4. 'Determination of elemental concentrations' and 'Mineralogy analysis' are the two final steps. The first converts elemental yields to elemental weight concentrations. The second converts elemental concentrations to mineralogy results. Conversion to elemental concentrations is described in Chapter 4. Mineralogy calculation is a geology problem, and is out of the scope of this research.

In addition, a complete example of calculation is given in Chapter 5.

Chapter 2

Nuclear Reactions

The Tool resolves the elemental compositions of the rock formations by deconvoluting the neutron activated prompt and delayed gamma spectra. This section discusses the nuclear reactions that are of importance to the Tool. The fundamental physical processes are explained in great details elsewhere, such as Knoll's radiation detection book[10] and Han's dissertation[11]. In this section, the focus is on how they are of interest to the development and application of the Tool.

2.1 Neutron transport

Of the numerous ways in which neutrons can interact with nuclei, three of them are the most important to the Tool.

2.1.1 Elastic scattering

The elastic scattering reaction changes the neutron's travel direction and energy, but does not directly contribute to the gamma spectrum. It provides a path for neutrons to thermalize so that neutrons can undergo the neutron capture reaction, which eventually contributes to the gamma spectrum. The reaction is characterized by the conservation of energy and momentum.

2.1.2 Neutron capture (n, γ)

Although (n, γ) is possible over a wide energy range, its probability is much higher in the thermal energy range. During the (n, γ) reaction, a neutron is absorbed by the target nucleus, and a new nucleus at an excited energy state is formed. The new nucleus de-excites by emitting at least one γ photon, whose energy is characteristic of the target nucleus.

The newly formed nucleus may be stable or unstable. One commonly observed example is an ^{27}Al nucleus, which may absorb a neutron to form an ^{28}Al nucleus. In addition to the characteristic gammas due to the (n, γ) reaction, ^{28}Al is a radioactive isotope with a half-life of 2.24 minutes. ^{28}Al β^- decays to ^{28}Al, and also emits a 1.78 MeV γ photon.

Notice that in the context of nuclear reactor engineering, the term 'neutron capture' refers to all types of neutron reactions that are not scattering reactions. In other words, (n, γ) is one type of neutron capture reaction, and neutron capture reaction does not include (n, γ) only. For example, the nuclear fission reaction is also a type of neutron capture reaction. Nevertheless, the term 'neutron capture', or simply 'capture' is frequently used as a synonym for (n, γ) in the oil industry, as other types of neutron capture reactions, such as fission or (n, α) reaction, are either very rare, or the products make no detectable contribution to the measurements.

2.1.3 Inelastic scattering (n, n'γ)

Inelastic scattering is another way γ can be generated. In an inelastic scattering reaction, an energetic neutron collides with a nucleus, and instead of being scattered immediately, the neutron is absorbed into the nucleus, forming a new metastable compound nucleus. The compound nucleus then decays by emitting a neutron, and leaving the target nucleus in an excited state. The excited nucleus may de-excite by emitting gamma photons whose energies are characteristic of the target nucleus. Such inelastic scattering that results in de-excitation by gamma emissions is denoted by (n, n'γ), and can be represented by the formula:

$$ {}^{\mathrm{A}}_{\mathrm{Z}}\mathrm{X} + n \longrightarrow {}^{\mathrm{A+1m}}_{\mathrm{Z}}\mathrm{X} \longrightarrow {}^{\mathrm{A}}_{\mathrm{Z}}\mathrm{X}^{*} + n' \longrightarrow {}^{\mathrm{A}}_{\mathrm{Z}}\mathrm{X} + n' + \gamma $$

Compared to the (n, γ) reaction, the (n, n'γ) is more complex from the perspective of gamma spectroscopy for two reasons:

1. The inelastic scattering reaction requires a threshold energy in order to take place,

which is derived from the Q value formula, and is expressed as[12]:

$$T_n \geq E_{L1}\frac{A+1}{A} \tag{2.1}$$

where T_n is the kinetic energy of the incident neutron, E_{L1} is the energy of the target nucleus' first excited level, and A is the atomic number of the target nucleus. The formula implies that the energy of the incident neutron should be slightly higher than the first excited state of the target nucleus in order for inelastic scattering to occur. This energy threshold is usually in the MeV range. Table 2.1 summarizes the (n, n'γ) reaction threshold energies for several isotopes that are commonly found in the earth formations.

Table 2.1 Inelastic scattering threshold energies of isotopes commonly found in the earth formations.

Isotope	Threshold (MeV)	Isotope	Threshold (MeV)
^{12}C	4.81	^{32}S	2.30
^{16}O	6.44	^{39}K	2.59
^{24}Mg	1.43	^{40}Ca	3.44
^{27}Al	0.88	^{48}Ti	1.00
^{28}Si	1.84	^{56}Fe	0.86

2. The gamma energy spectrum of the (n, n'γ) reaction is a function of energy of the incident neutron. Due to the mechanism of (n, n'γ) reaction, higher incident neutron energy may excite the target nucleus into higher energy levels, and thus 'unlock' new decay schemes and gammas with different energies to be emitted. Figure 2.1 shows the level scheme of the ^{28}Si nucleus. According to Equation 2.1, the threshold energy for the first excited state is $1.779 \times 29/28 = 1.843$ MeV, and that of the second excited state is 4.783 MeV. If the incident neutron has an energy below 1.843 MeV, inelastic scattering is impossible. If the neutron's energy is between 1.843 MeV and 4.783 MeV, inelastic scattering is possible, but only 1.779 MeV gamma can be emitted. If the neutron's energy is above 4.783 MeV,

then the target nucleus can be excited to the second energy level, and can emit 2.838 MeV gammas.

2.1.4 Probabilities of reactions

Figure 2.2 illustrates the ratios of the individual reaction microscopic cross section to the total microscopic cross section of isotope ^{28}Si, over the energy range of 0.001 eV to 20 MeV. This represents the probability of each reaction, relative to the sum of all reactions. ^{28}Si is used as an example because it is one of the most commonly observed elements in the earth, and both its capture gammas and (n, n'γ) gammas are relatively pronounced.

From the figure, one can see that elastic scattering is the most probable reaction between 0.001 eV and $\sim$ 5 MeV. (n, γ) has a higher probability in the thermal energy range, except for a few resonances in the fast neutron range. These resonance captures do not have a big impact on nuclear oil well logging application, as the resonance capture regions are all very narrow. It can also be observed that inelastic scattering only becomes possible from approximately 2 MeV. To be exact, the probability of inelastic scattering is 0 below the 1.843 MeV threshold.

Also notice that at higher energies, the probability of reactions other than elastic scattering, inelastic scattering, or (n, γ) start to increase. The products of these reactions vary, but are usually ions, such as α particles, with very short range, and are disregarded in the design of a nuclear oil well logging device.

2.2 Photon transport and detector Response

2.2.1 Photon reactions

The three types of photon reactions of concern to the Tool are: photoelectric absorption, Compton scattering, and pair production, which will be explained briefly.

Photoelectric absorption

Photoelectric absorption refers to the process that a photon imparts all its energy to an orbital electron, and the electron is ejected from the orbit. After the reaction, the photon ceases to exist. The energy of the incident photon must exceed a threshold for

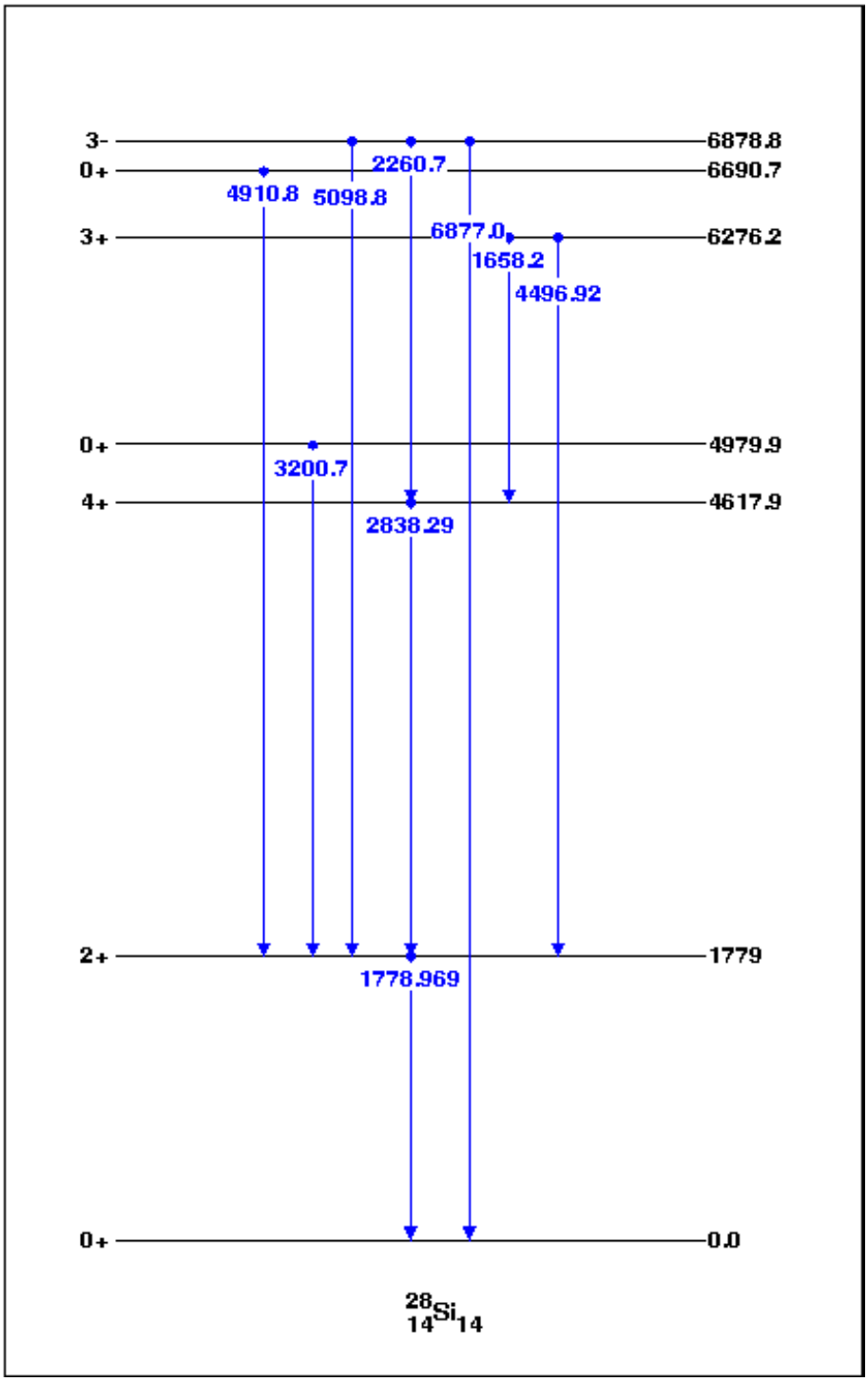

Figure 2.1 Level scheme of ^{28}Si, up to 6880 KeV[13].

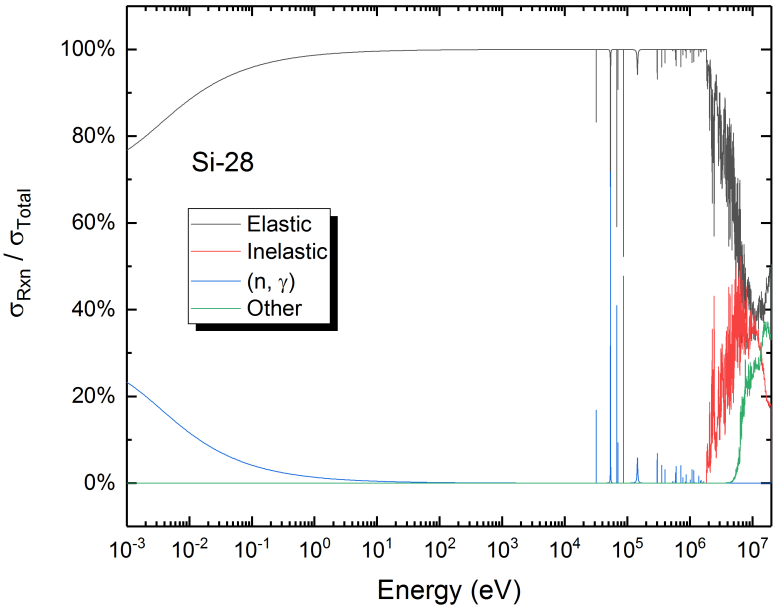

Figure 2.2 Ratios of microscopic cross sections of individual reactions to the total microscopic cross section of ^{28}Si. Cross section data extracted from ENDF data file[14].

the photoelectric effect to take place. After the electron is ejected, the atom may be in an excited state, and may de-excite by emitting fluorescence X-rays. Due to the detection resolution, these X-rays cannot be directly observed on typical scintillation detectors.

Compton scattering

Compton scattering refers to the process where a photon imparts a portion of its energy to an orbital electron, after which the electron is ejected from its orbit. Both energy and momentum are conserved in the reaction. Therefore, the energy of the scattered photon and the kinetic energy of the scattered electron can be calculated if the energy of the incident photon and its incident angle are known, i.e.,

$$E'_\gamma = \frac{E_\gamma}{1 + (1 - \cos\theta)E_\gamma / m_e c^2} \tag{2.2}$$

where E'_γ is the energy of the scattered photon, E_γ is the energy of the incident photon, $\cos\theta$ is the scattering angle of the photon in lab coordinate, m_e is the mass of electron, and c is the speed of light.

A distinctive feature of Compton scattering is that the maximum amount of energy that a photon can impart to the electron is limited. The maximum electron recoil energy directly dictates the Compton edge of a gamma spectrum. According to Equation 2.2, when $\theta = 0$, the incident photon does not lose energy. When $\theta = \pi$, the energy loss, or the energy transferred to the electron is

$$T_{e,max} = \frac{2E_\gamma/m_e c^2}{1 + 2E\gamma/m_e c^2} \cdot E_\gamma \tag{2.3}$$

where $T_{e,max}$ denotes the maximum possible electron recoil energy. Figure 2.3 shows the maximum percentage of energy of the incident photon that can be transferred to the recoil electron, as a function of the incident photon energy. It can be seen that higher energy incident photons lose more energy.

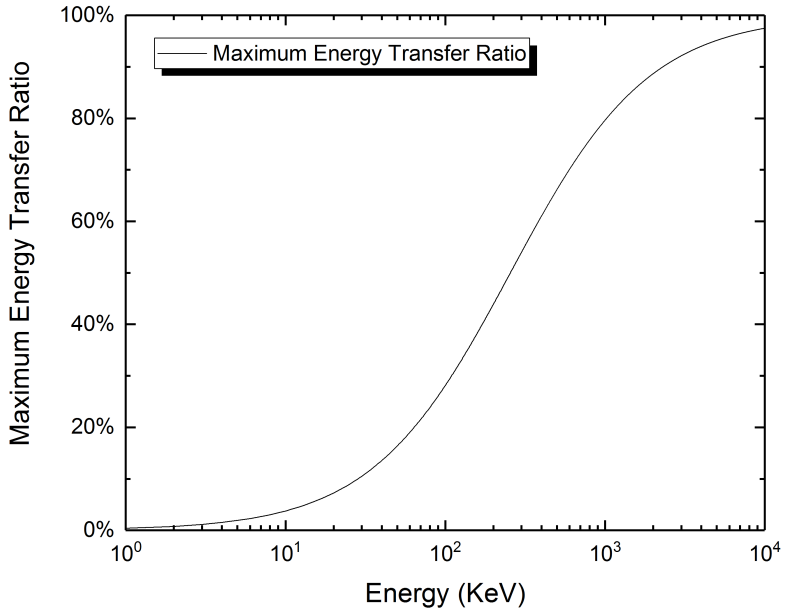

Figure 2.3 Maximum percentage of energy transferable to the recoil electron as a function of incident photon energy.

Pair production

Pair production refers to the process where an energetic photon ceases to exist, and splits into an electron/positron pair. Pair production is not a simple spontaneous reaction that can take place by a photon alone. Usually, the photon must be in the vicinity of a nucleus. In rare occasions, the pair production reaction may also take place in the vicinity of an electron, but the probability is orders of magnitude smaller than pair production in a nuclear field reaction. As the energy of the photon is completely converted into mass and kinetic energies, the energy of the photon must be greater than 1.022 MeV, which is two times the mass of an electron. The kinetic energy of the electron or the positron is simply half of the energy of the incident photon in excess of 1.022 MeV. The electron and positron subsequently travel in the medium, and deposit their kinetic energy. When the electron deposits all its energy, it becomes localized. When the positron is localized, it is annihilated with an electron, and creates two 511 KeV photons.

2.2.2 Probabilities of reactions

In principle, photoelectric absorption dominates the lower energy range, around or below 100 KeV; Compton scattering dominates the intermediate MeV range; and pair production becomes the dominant reaction in the upper MeV region. Figure 2.4 shows the macroscopic cross sections (Σ) of the three individual reaction types and the total Σ of $LaBr_3$. Figure 2.5 shows the relative ratios of the three reactions.

2.2.3 Detector response

The ionizing energetic photons activated by the neutrons eventually need to be recorded by the detector. The Tool utilizes a $LaBr_3$ crystal, which is very well suited for well logging. This section discusses features of the detector in the context of gamma spectroscopy.

Features on a spectrum

In order to illustrate and discuss features that are typically observed in gamma ray energy spectra under more restricted and idealized conditions, an MCNP[15][16] simulation is conducted. Figure 2.6 shows a cross section perpendicular to the Y axis (XZ plane) of

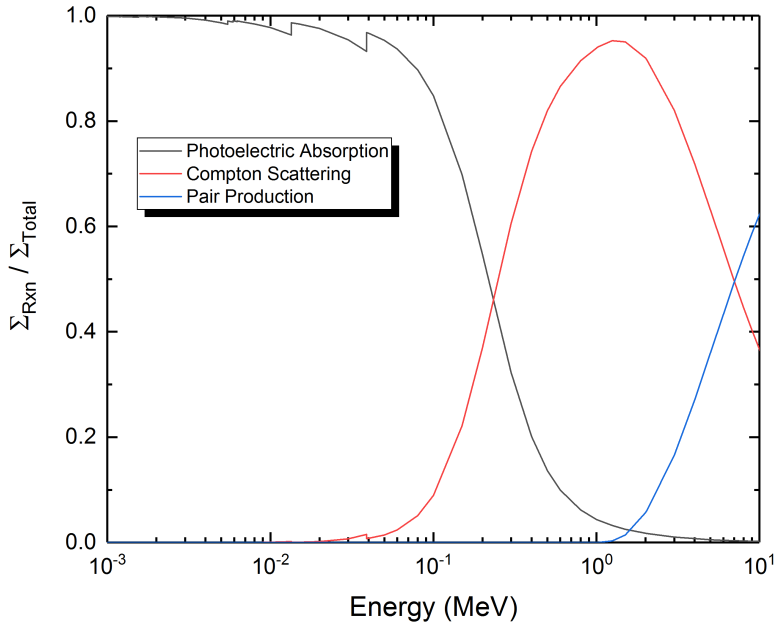

Figure 2.4 Macroscopic cross sections of $LaBr_3$ between 100 KeV and 20 MeV. Calculated based on NIST XCOM database.

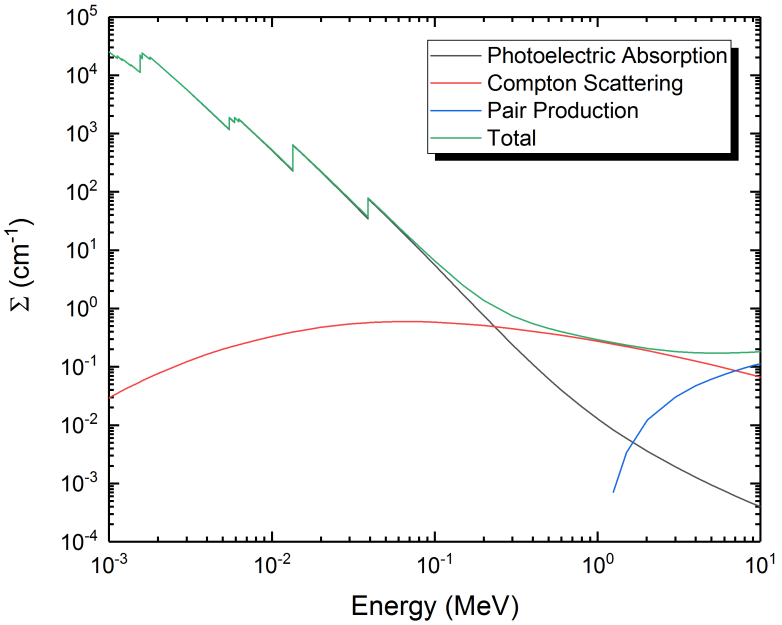

Figure 2.5 Ratios of three types of photon reactions for $LaBr_3$ between 100 KeV and 20MeV.

the geometry modeled in MCNP. In this geometry, cell 11 is a 6 inches long right circular cylinder (RCC) $LaBr_3$ detector; cell 12 is a cubical vacuum space of 60 cm long on each side, excluding cell 11; cell 13 is a 60 cm radius sphere excluding the cube, made of lead; cell 17 is the outer vacuum. The radiation source is set to be an isotropic photon source which emits 2.223 MeV photons at $(12.7, 0, 0)$, or 4 inches away from the cylindrical surface of the detector. Figure 2.7 is a 3 dimensional representation of the model.

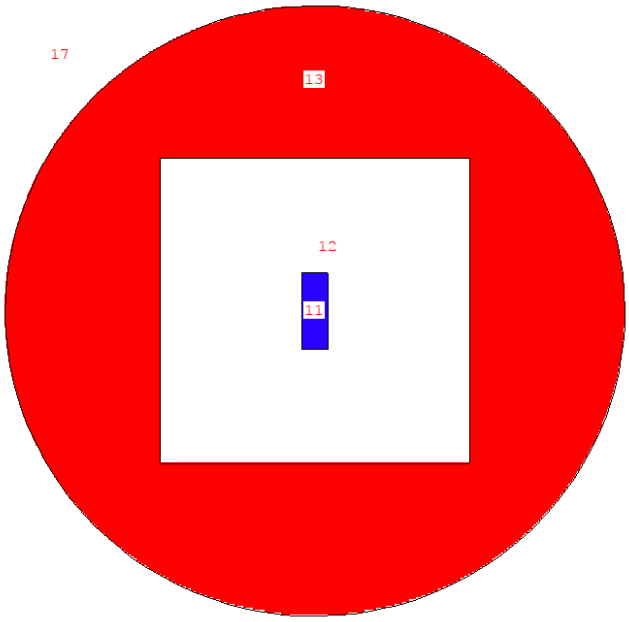

Figure 2.6 Cross section of the geometry set up used for MCNP modeling. Figure shows a cross section perpendicular to the Y axis.

This model is very much simplified and idealized. However, it is very convenient to illustrate some important concepts of gamma spectroscopy involved in nuclear oil logging. Figure 2.8 shows the simulation result. The F8 tally is used for calculating the distribution of energy deposited in the detector. The spectrum shown in Figure 2.8 is not broadened, which means that the detection resolution is infinite. Eight features of the spectrum have been marked by letters, they are:

A: Full energy peak Energy of the full energy peak equals the energy of the source photon. Pulse signals that contribute to the full energy peak are those formed when

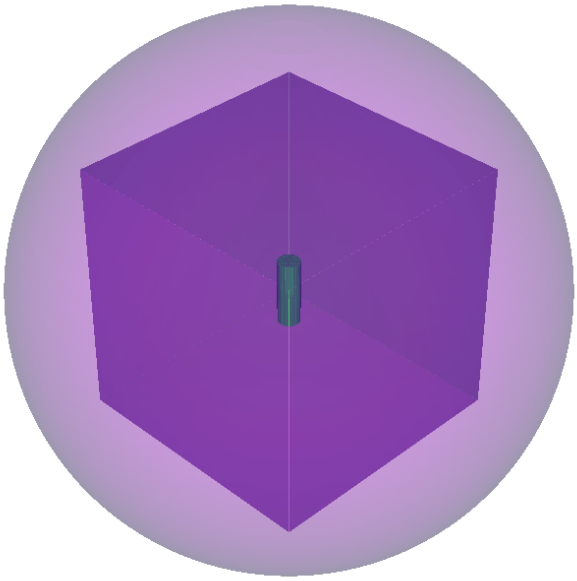

Figure 2.7 3D presentation of the geometry set up used for MCNP modeling.

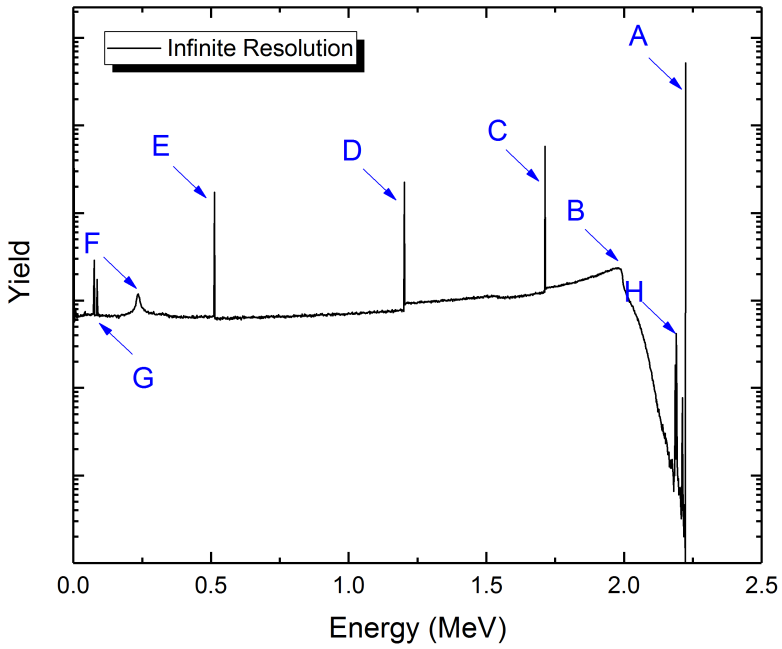

Figure 2.8 MCNP F8 tally result of the geometry shown in Figure 2.6.

a source photon enters the detector, and deposits all its energy in the detector. The energy deposition can be completed by one single photoelectric absorption, or by a series of reactions. A full energy peak is also occasionally referred to as a 'photoelectric peak'. This is incorrect, because this peak does not only consist of contributions from single photoelectric absorption of source photons.

B: Compton edge Statistically, some source photons will enter the detector, undergo the Compton scattering reaction once, and then exit the detector without depositing more energy. If this happens, according to Equation 2.2, as the scattering angle varies between 0°to 180°, the energy deposited in the detector varies between 0 to a maximum value, when $\theta = 180°$. For the case modeled, this maximum energy deposition due to Compton scattering is

$$\Delta E = E_\gamma - E'_\gamma = 2.223 - \frac{2.223}{1 + (1 - \cos(\pi)) \times 2.223/0.511} = 1.994 \text{ MeV} \tag{2.4}$$

On the gamma energy spectrum, this corresponds to an edge, pointed by letter 'B' in Figure 2.8, known as the 'Compton Edge'.

C: Single escape peak Energy of the single escape peak equals the energy of the source photon minus 511 KeV. When a source photon enters the detector, undergoes a pair production reaction and becomes an electron-positron pair, the positron annihilates inside the detector. Finally one of the 511 KeV annihilation photons escapes the detector without depositing energy inside the detector, and the final pulse signal formed will contribute to the single escape peak. After the reaction is complete, the source photon deposits all its energy except the 511 KeV annihilation photon. The energy of the peak formed is the energy of the source photon minus 511 KeV.

D: Double escape peak Energy of the double escape peak equals the energy of the source photon minus 1.022 MeV. The mechanism of the formation of the double escape peak is almost identical to that of the single escape peak, except that both annihilation photons escape from the detector without any interaction.

E: Annihilation peak Energy of the annihilation peak is 511 KeV. Photons contributing to the annihilation peak are those that undergo the pair production reaction outside

the detector, where one of the 511 KeV photons from the positron annihilation reaches the detector and deposits all its energy in the detector. The annihilation peak primarily appears when the detector is surrounded by a dense medium.

F: Backscattering peak Like the annihilation peak, the backscattering peak is also formed outside the detector. A pulse signal contributing to the backscattering peak is formed when a source photon reacts with the medium outside the detector by undergoing Compton scattering. The scattered photon reaches the detector and deposits all of its energy in the detector. The scattering angle incorporates a small range around 180°, and therefore the backscattering peak is not just a single line.

The energy of the backscattering peak is not a constant, and is usually between 200 and 300 KeV. For the simulated case, assuming the scattering angle is 180°, the energy of the scattered photon will be:

$$E'_\gamma = \frac{2.223}{1 + (1 - \cos(\pi)) \times 2.223/0.511} = 0.229 \text{ MeV} \tag{2.5}$$

G: X-ray fluorescence peaks X-ray fluorescence peaks usually incorporate a small number of peaks clustered together, and are formed in the medium surrounding the detector. When energetic photons interact with the atoms of the materials surrounding the detector, the atoms may become excited. When they de-excite, characteristic X-ray photons are emitted. When such an X-ray photon reaches the detector and deposits all its energy to the detector, a pulse signal is formed which contributes to one of the X-ray florescence peaks.

The energies of the X-ray fluorescence peaks are related to the orbital electron binding energies of the material surrounding the detector, and are usually less than 100 KeV.

H: X-ray escape peaks When energetic photons deposit energy inside the detector, the detector atoms may also be excited, and de-excite by emitting characteristic X-ray photons. When an X-ray photon escapes the detector without depositing its energy, the total energy deposited in the detector by the incident source photon while missing a small portion. The pulse signals formed contribute to one of a few X-ray escape peaks near the full energy peak.

Energy resolution

Energy resolution characterizes how well a detector can resolve energy peaks close to each other. For scintillation detectors, the energy peaks are Gaussian peaks, and can be described by the normal distribution

$$f(E|\mu,\sigma^2) = \frac{1}{\sqrt{2\pi\sigma^2}} \exp^{-\frac{(E-\mu)^2}{2\sigma^2}} \tag{2.6}$$

where E is the energy, μ is the peak centroid, and σ is the standard deviation. σ has the same units as energy, and is a commonly used quantity to characterize the width of the peak. Another commonly used quantity is the full width at half maximum, or 'FWHM', which is the width of the peak at half of the amplitude of the peak. By definition, there is

$$\text{FWHM} \approx 2.355\sigma \tag{2.7}$$

The most frequently used quantity to characterize the energy resolution of the detector is the quotient of the FWHM of a peak divided by the centroid of the peak, i.e.

$$R = \frac{\text{FWHM}}{\mu} \approx 2.355\frac{\sigma}{\mu} \tag{2.8}$$

R is a unitless quantity, and is oftentimes presented as a percent.

Visually, a detector with better energy resolution would give narrower peaks. Physically, the energy resolution is related to the number of information carriers a detector can generate per unit energy deposition. For scintillation detectors, such as $LaBr_3$ or NaI, this translates to the number of visible light photons emitted inside the crystal per unit photon energy deposited. According to data released by Saint-Gobain, a well-known scintillation crystal manufacture, the $LaBr_3$ crystal emits 63 visible light photons per KeVγ absorbed, whereas the NaI crystal emits only 38 photons per KeV γ absorbed[17]. This agrees with the fact that $LaBr_3$ has better resolution.

Even for the same scintillation detector, the energy resolution is not the same for peaks of different energies. The reason is that higher energy photons deposit more energy in the crystal, and therefore generate more visible light photons. According to Poisson statistics, more visible light photons will result in wider peaks with better resolution; that is, for higher energy photons, FWHM will be greater, μ will also be greater, and the overall resolution FWHM/μ is smaller (better). For avoiding confusions and ambiguities,

when the resolution of a detector is quantified with only one parameter, this parameter refers to the energy resolution at 662 KeV, which is the gamma energy of the ^{137}Cs source.

As the energy resolution is also a function of photon energy deposition, it is of practical interest to characterize how the resolution changes, usually for simulation purposes. In MCNP, arguably the most frequently used general purposes Monte Carlo simulation program, the embedded photon transport theories do not consider the scintillation process and the subsequent photo-multiplication process. Therefore, by relying on the simulation of the physics, only spectra like Figure 2.8 can be calculated. To make the energy deposition spectra more realistic, a separate subroutine that broadens the spectra is needed. In MCNP, this module is called 'Gaussian Energy Broadening', or 'GEB' for short. GEB randomizes the amount of energy a source photon eventually deposits inside the detector by sampling a Gaussian distribution. This distribution is characterized by E which equals the energy deposition without GEB, as well as an FWHM whose value is calculated by

$$\text{FWHM} = a + b\sqrt{E + cE^2} \tag{2.9}$$

In Equation 2.9, E is the energy of the energy deposited without GEB, and a, b, and c are all empirical parameters. The net effect of this randomization is very close to broadening each tally bin of the infinite resolution F8 spectrum by convoluting the value of that bin by a FWHM, calculated by Equation 2.9, where the energy E corresponds to the center of the bin.

In 2012, Wang and Gardner[18] found it was also possible to further simplify this relation to an exponential expression, i.e.,

$$\text{FWHM} = d \cdot E^e \tag{2.10}$$

where d and e are both empirical parameters.

To realistically broaden a simulated energy spectrum using either Equation 2.9 or Equation 2.10, the empirical parameters should first be determined by taking multiple measurements using the desired detector, after which the measured peak widths are fitted with the corresponding model to calculate the values of the parameters. Figure 2.9 shows an example of such a process. In the figure, each black dot represents the FWHM of a full energy peak measured using a $LaBr_3$ detector. These data points are then gathered and fitted to the MCNP model and the Gardner model. It is found that both models

can describe the FWHM vs energy relation with good accuracy.

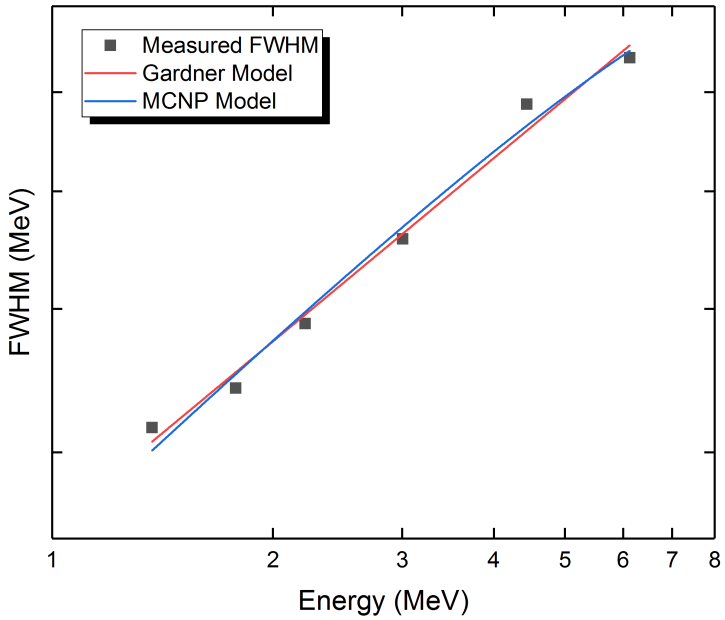

Figure 2.9 FWHM fitted to Equation 2.9 and Equation 2.10 respectively. The measurements are made using a $LaBr_3$ detector.

Figure 2.10 shows a comparison of the MCNP F8 tally results, as shown in Figure 2.8, broadened using MCNP GEB card, with parameters derived from Figure 2.9.

2.3 Data Sources

Data for neutron capture gammas are relatively abundant. A publication by IAEA titled 'Database of Prompt Gamma Rays from Slow Neutron Capture for Elemental Analysis'[19] is a good reference for looking up capture gammas for individual isotopes. Other sources for capture gamma rays include a nuclear data table by Reedy and Frankel[20], and the widely used 'Evaluated Nuclear Structure Data File', or more frequently referred to as 'ENSDF'[21]. Brookhaven National Laboratory National Nuclear Data Center (NNDC) hosts an online system for parsing the raw ENSDF data file to more readable reports. Information regarding (n, γ) of a specific isotope can be easily searched by specifying the target isotope and reaction '(n,g)', where 'g' refers to 'gamma'.

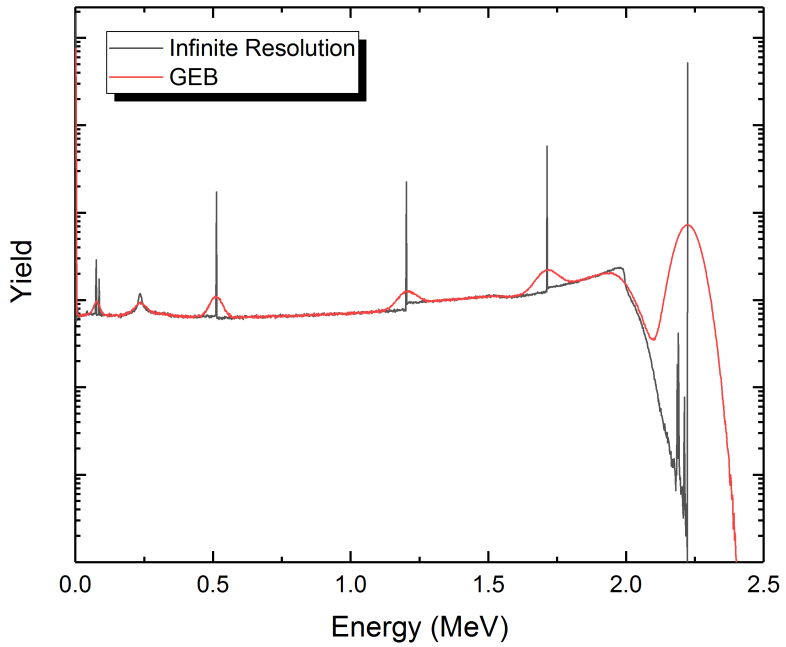

Figure 2.10 Energy spectrum as shown in Figure 2.8 broadened using realistic broadening parameters.

Spectra for neutron inelastic scattering can be found from a comprehensive book compiled by a Soviet and Iraqi joint research team, titled 'Atlas of Gamma-ray Spectra from the Inelastic Scattering of Reactor Fast Neutrons'[22]. Gamma data from this book are based on experiments, and some of the weak peaks may be missing. For more comprehensive list of inelastic gammas, a nuclear data search system called 'NuDat' hosted by Brookhaven National Laboratory NNDC can be very helpful. Figure 2.1 is generated using NuDat. Alternatively, inelastic gammas can also be acquired from the ENSDF search system hosted by NNDC, by searching for 'Adopted Levels' of the target nucleus.

As for neutron reaction cross sections, the Evaluated Nuclear Data File (ENDF)[14] is very comprehensive and is also widely applied. Brookhaven National Laboratory National Nuclear Data Center hosts a very usable system for online ENDF data retrieval and visualization. Notice that the cross section data included in the original ENDF database are temperature independent, and need further processing to broaden the resonance peaks at specified temperature. A nuclear data veteran, Dr. Dermott E. Cullen maintains a computer code called PREPRO[23], which processes ENDF cross sections by broadening

the resonance peaks and linearizing the data points. Dr. Cullen also maintains a database, called POINT. This database is essentially identical to ENDF database, but have all the neutron reaction cross sections linearized and broadened at a few temperatures already. Thus, for simpler programming purposes, POINT is much more useful than ENDF. The most recent version of POINT at the time this document is composed, is POINT 2015, and is hosted by IAEA. Cross sections in Figure 2.2 are extracted from POINT 2015 database.

Data for photon interactions can be found from at least two reliable sources. One is a database called 'the Evaluated Photon Data Library, 97 version'[24], which is more comprehensive and includes not only cross sections, but also other relevant data for secondary particles. For simpler applications, the National Institute of Standards and Technology (NIST) also maintains a good system called XCOM[25]. XCOM is both a database of photon reaction cross sections, and a computer code, available online and for downloading, to calculate the cross sections for compounds and mixtures. Cross sections in Figure 2.4 are acquired from the NIST XCOM database.

Chapter 3

Spectral Acquisition and Preprocessing

3.1 Spectral acquisition

For each new sample, spectra measurement is the first step of analysis. By utilizing the pulsed neutron generator (PNG), three spectra are measured alternately at high speed: burst spectrum, capture spectrum, and background spectrum.

3.1.1 Neutron source

The usage of PNG is one of the most distinguishing features of advanced neutron nuclear logging tools, such as the Tool itself. A D-T neutron source exerts high voltage and accelerates deuterium ($^{2}_{1}\mathrm{H}$) and/or tritium ($^{3}_{1}\mathrm{H}$) toward a solid target which contains tritium and/or deuterium. When the kinetic energy of the incident ion is high enough, it may overcome the Coulomb barrier of the target nucleus, and undergoes a fusion reaction[26]

$$^{2}_{1}\mathrm{H} + ^{3}_{1}\mathrm{H} \rightarrow ^{4}_{2}\mathrm{He} + ^{1}_{0}\mathrm{n} + 17.586 \text{ MeV}$$

The total energy emission of the reaction is 17.586 MeV, and is distributed between the α particle and the neutron. The neutron eventually gains a kinetic energy of 14 MeV.

The principle of operation of a D-T source makes it a favorable neutron source for formation elemental analysis in at least three ways:

1. The fusion reaction does not occur spontaneously. The fact that ions have to be

accelerated to initiate the fusion reaction makes it much safer than the traditional chemical neutron sources, such as ^{252}Cf or ^{241}Am-Be. The neutron emission of a D-T generator will automatically stop once the high voltage is cut off. This is impossible for chemical sources.

2. Another type of fusion reaction, D-D reaction, can also produce energetic neutrons. But the neutron yield is orders of magnitude lower than that of D-T reaction[27]. In addition, the energy of the D-T source neutron is 14 MeV, but the energy of D-D neutron is only 2.5 MeV. Higher energy neutrons are advantageous in the sense that they induce more inelastic scattering gammas with higher reaction threshold energies to be emitted.

3. As the generator is a controllable source and can be turned on and off, alternating the operating status allows measurements of both an inelastic gamma spectrum and a capture gamma spectrum. Some elements can only be found practically in one of the two spectra. For example, H can only be found in the capture spectrum, and O can only be found in the inelastic spectrum. Some other elements, such as Si, is fairly observable in both spectra. The target isotopes emitting different characteristic gammas in these two different types of neutron reactions allow the elements to be measured and analyzed with a different strategy.

3.1.2 Measuring spectra

In order to take a measurement, the control unit instructs the PNG to emit neutrons intermittently, and also coordinates the detector to make measurements accordingly. The timing sequence of neutron emission and data acquisition is called a 'firing sequence', or sometimes 'firing scheme'. Each tool may have a different firing sequence. But at the very least, to take advantage of the pulsed generator, the firing sequence should allow the detector to take three different measurements:

1. Burst spectrum: photon energy spectrum taken when the neutron generator is steadily emitting fast neutrons. A burst spectrum is also sometimes referred to as a 'total spectrum', since it includes both capture and inelastic gamma rays.

2. Capture spectrum: photon energy spectrum taken when the neutron generator has just been deactivated, and the photon counting rate is slowly and steadily

decreasing.

3. Background spectrum: photon energy spectrum taken when the neutron generator has been deactivated long enough and it can be considered that prompt gammas are no longer generated.

The Tool has a complex firing sequence. Each sequence is 50 ms long, and is divided into three periods:

- Period 1 is 45 ms long, and constitutes 225 cycles of a 200 μs long sub-cycle. In each sub-cycle, the neutron generator is activated in the first 60 μs, and then deactivated. The counts detected between 20 μs to 60 μs are counted towards the burst spectrum. The counts detected between 70 μs to 200 μs are counted towards the capture spectrum.

- Period 2 is 2 ms long. Counts detected during Period 2 are used for the macroscopic neutron capture cross section (also known as 'sigma' in the oil industry) calculation, and are not used for spectral analysis.

- Period 3 is 3 ms long. Counts detected during Period 3 are considered as background radiation. The background spectrum will be subtracted from the measured burst spectrum and the measured capture spectrum to form the background-free burst and capture spectra.

Figure 3.1 illustrates the whole cycle graphically. Notice that to show the repetition of the neutron emission sub-cycles, the abscissa is not drawn to scale. Each yellow block between 0 ms to 45 ms represents one sub-cycle of Period 1, the green block represents Period 2, and the purple block represents Period 3. Figure 3.2 is an example of a count rate time spectrum of a experiment measurement. The sample was a large tank filled with water. The figure shows the time spectrum of one single sub-cycle of Period 1, averaged over the entire measurement period, which was approximately 20 minutes. This figure corresponds to one single yellow block in Figure 3.1.

In Figure 3.2, the generator is activated at time 0 μs. In the first 20 μs, the neutron output and the photon counting rate are both rapidly increasing. During this time, the detector only takes counts, but does not generate a spectrum. From approximately 20 μs, the gamma count rate is stabilized. The counts collected during the period marked

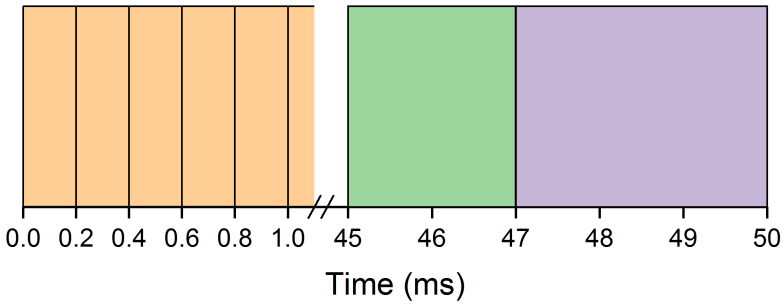

Figure 3.1 Firing sequence of the Tool. The yellow blocks represent the neutron emission sub-cycles of Period 1, the green block represents Period 2, and the purple block represent Period 3.

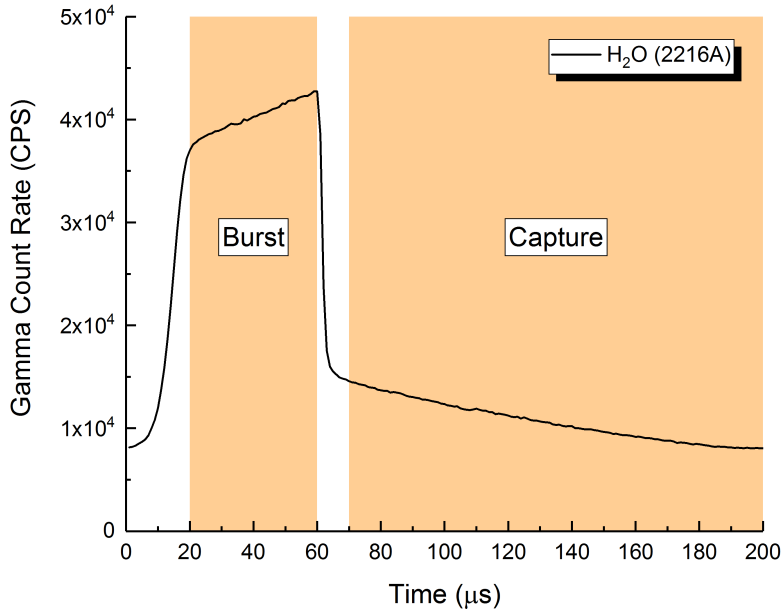

Figure 3.2 Count rate time spectrum of a water tank measurement.

by the smaller yellow block are histogrammed to form the burst spectrum. The burst spectrum includes capture gammas, inelastic gammas, and background gammas. The background spectrum includes gamma rays from neutron activation as well as natural background.

After 60 μs, the neutron generator is cut off. Between 60 μs to 70 μs, the output of the generator rapidly drops to 0, and the fast neutrons that are already in the formation are thermalized. Similar to the first 20 μs, the detector records counts only, but they are not included in the energy spectrum.

From 70 μs to 200 μs, which is the end of the current sub-cycle, the neutron generator remains deactivated. The neutrons that are already in the formation are below the lowest (n, n'γ) reaction threshold. These neutrons lose energy by elastic scattering reactions, and are gradually absorbed through neutron capture reactions. During this period, the detector actively takes counts and collects a spectrum, called 'capture spectrum'. Gammas of the spectrum come from (n, γ) reactions as well as the background.

For each sample, the firing sequence is repeated until the predesignated measurement time is reached.

3.2 Noticeable spectral features

By the end of the measurement stage, three raw gamma energy spectra are generated. Figure 3.3 shows a typical water tank measurement in raw counts, and Figure 3.4 shows the same measured spectra in count rates.

In Figure 3.4, there are a few features worth mentioning:

1. A: Hydrogen peak at 2.223 MeV. More specifically, the peak is the hydrogen (n, γ) peak. The hydrogen peak is almost always present in the burst spectrum and the capture spectrum, because there is almost always liquid in the borehole, and usually there is water or hydrocarbon in the pores of the rocks. In addition, as the (n, γ) cross section of hydrogen is 0.332 barn at 0.0253 eV, which is fairly high comparing to other common elements in the formation. Thus the hydrogen peak is usually the most pronounced peak in both the capture and the burst spectrum.

   By specification, the energy range of a standard energy spectrum of the Tool is defined in a way such that the hydrogen peak is centered at the 65^{th} channel. When logging, the firmware on the Tool actively searches the hydrogen peak, and

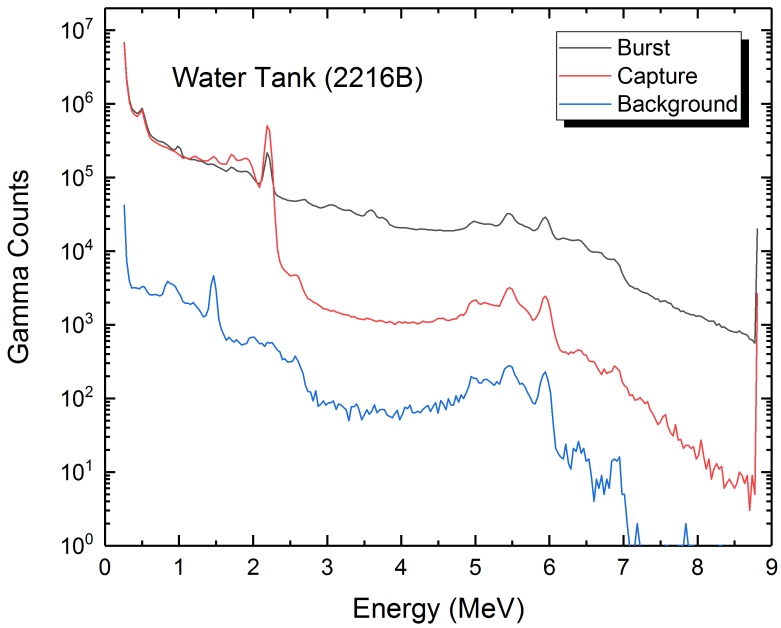

Figure 3.3 Unprocessed gamma spectra of a water tank measurement shown in raw counts.

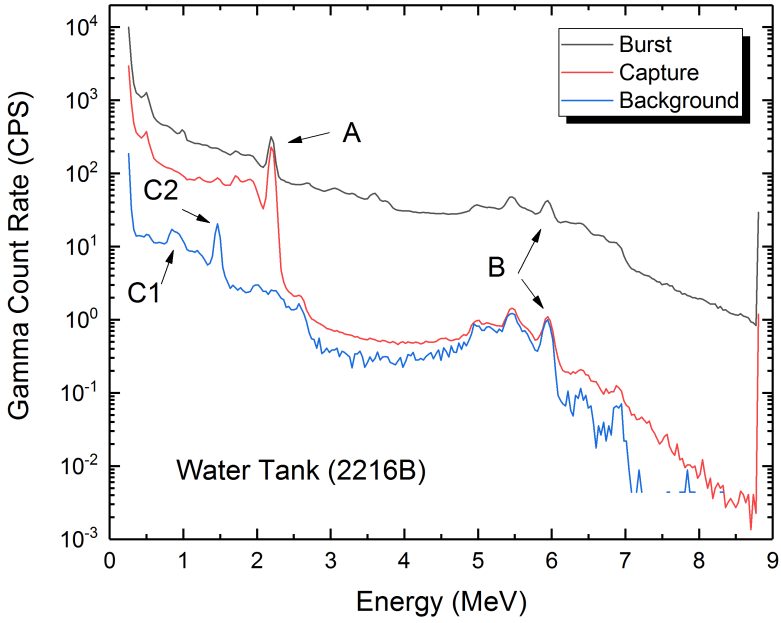

Figure 3.4 Unprocessed gamma spectra of a water tank measurement shown in count rates.

adjusts the gain settings of the signal amplifier to make sure the hydrogen peak is aligned.

2. B: Oxygen peak at 6.129 MeV. In realistic measurements, the oxygen peak is almost always observable in the burst spectrum, and is usually present in the background spectrum. However, the counts that contribute to the oxygen peak come from two different sources.

   In the burst spectrum, most of the oxygen peak counts come from (n, n'γ) reaction with ^{16}O isotope. After the reaction, excited ^{16}O nucleus de-excites by emitting gammas, and 6.129 MeV gamma is the most intense one.

   Another source of the oxygen peak is oxygen activation delayed gamma. Above 10.2 MeV, the ^{16}O nucleus can undergo (n, p) reaction, and produce ^{16}N, that is

$$^{16}\mathrm{O} + \mathrm{n} \longrightarrow {}^{16}\mathrm{N} + \mathrm{p}$$

   ^{16}N is a radioactive isotope with a half-life of 7.13 s. It decays by emitting β^- and becomes ^{16}O again. After the β^- decay, the ^{16}O nucleus is in excited state, and de-excites by emitting gammas, which is the same as the (n, n'γ) reaction gammas. Figure 3.5 shows the probability of the (n, p) reaction at high energy region. It can be seen that the (n, p) reaction of ^{16}O is only possible above 10 MeV, and the maximum probability is about 6.5%. Figure 3.6 shows the decay scheme of ^{16}N and the energies levels of ^{16}O and the gamma energies. The most intense ^{16}O de-excitation gamma is 6.129 MeV, and is de-excitation from the second level down to the ground level.

   Similar to the oxygen activation peak, another commonly seen neutron activation delayed gamma peak is the ^{28}Al decay peak, as shown in Figure 3.7. ^{28}Al is a radioactive isotope with a half-life of 2.24 minutes. $^{28}_{13}$Al decays to excited $^{28}_{14}$Si by emitting β^- particle. The excited ^{28}Si subsequently de-excites by emitting a 1.779 MeV gamma. The decay scheme is shown in Figure 3.8. This ^{28}Al decay peak also has two sources: ^{28}Si activation and ^{27}Al activation.

   As shown in Figure 3.9, at higher energy range, $^{28}_{14}$Si has a relatively high probability of undergoing (n, p) reaction and produce $^{28}_{13}$Al, that is,

$$^{18}_{14}\mathrm{Si} + \mathrm{n} \longrightarrow {}^{28}_{13}\mathrm{Al} + \mathrm{p} \tag{3.1}$$

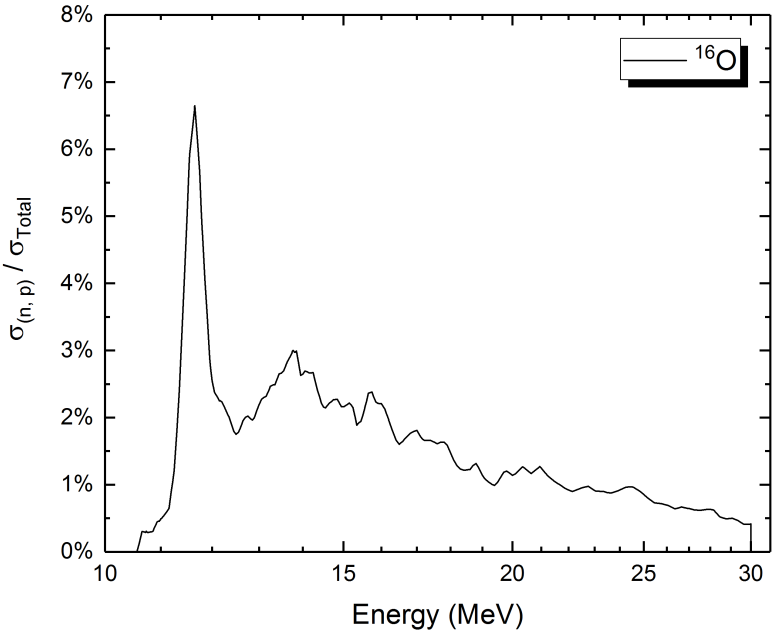

Figure 3.5 (n, p) reaction ratio of ^{16}O. Data from ENDF data files.

When the sample has abundant Si to be activated, the ^{28}Al decay peak is usually present in the spectrum.

Alternatively, the ^{28}Al isotope can also be produced by ^{27}Al(n, γ)^{28}Al reaction. Aluminum is generally not as abundant as Si in the rocks, but still can be significant, such as granite which has about 7% Al by weight. As a somewhat extreme example, Figure 3.10 shows the background spectrum of a large cubic aluminum block sample.

3. C1 and C2: Natural lanthanum element itself has a low radioactivity. Natural La element constitutes 99.911% stable ^{139}La, and 0.089% radioactive ^{138}La, which has a half-life of 1.05×10^{11} years. The hump marked by 'C1' and the peak marked by 'C2' in Figure 3.4 correspond to radiations originate from inside the detector.

   For 34.5% of the probability, $^{138}_{57}$La decays to excited $^{138}_{58}$Ce through β^- emission, as shown in Figure 3.11. The decay product subsequently de-excites to ground state by emitting a 0.789 MeV gamma. When the de-excitation gamma escapes the detector without depositing energy, the only energy deposition is the decay electron, with an end point of 255 KeV[28]. On a standard energy spectrum of the Tool, this β continuum is located between channel 1 to channel 8, and is

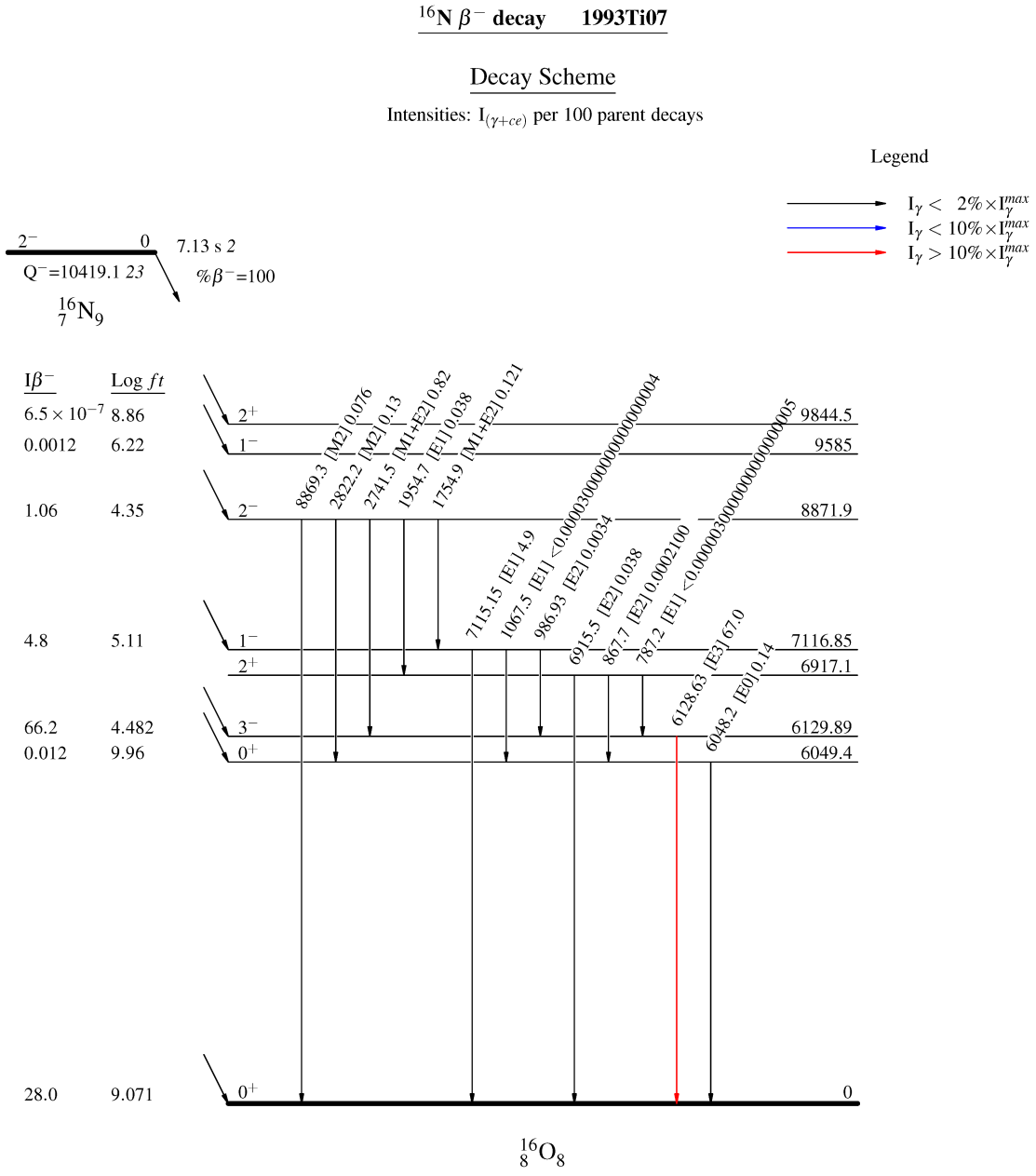

Figure 3.6 ^{16}N decay scheme. The chart also shows the energy levels and de-excitation gamma energies of ^{16}O. Data from ENSDF data files.

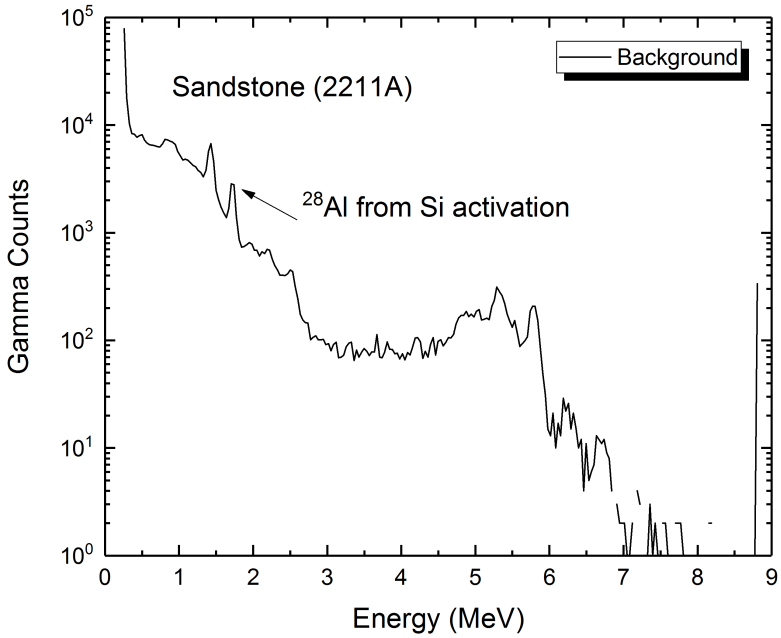

Figure 3.7 Background spectrum of a sandstone measurement.

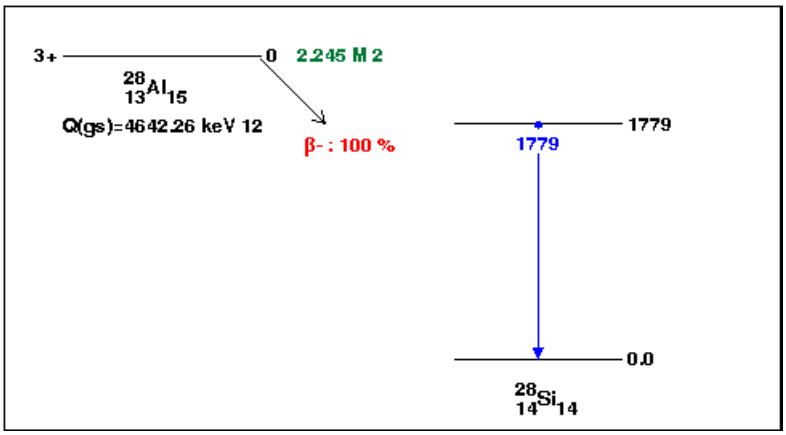

Figure 3.8 Decay scheme of $^{28}_{13}$Al. Data from ENSDF data files.

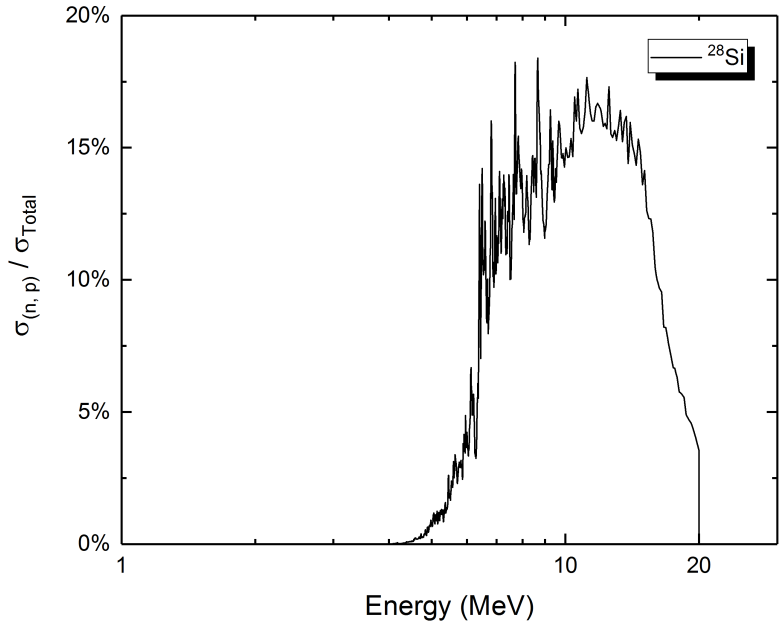

Figure 3.9 (n, p) reaction ratio of ^{28}Si. Data from ENDF data files.

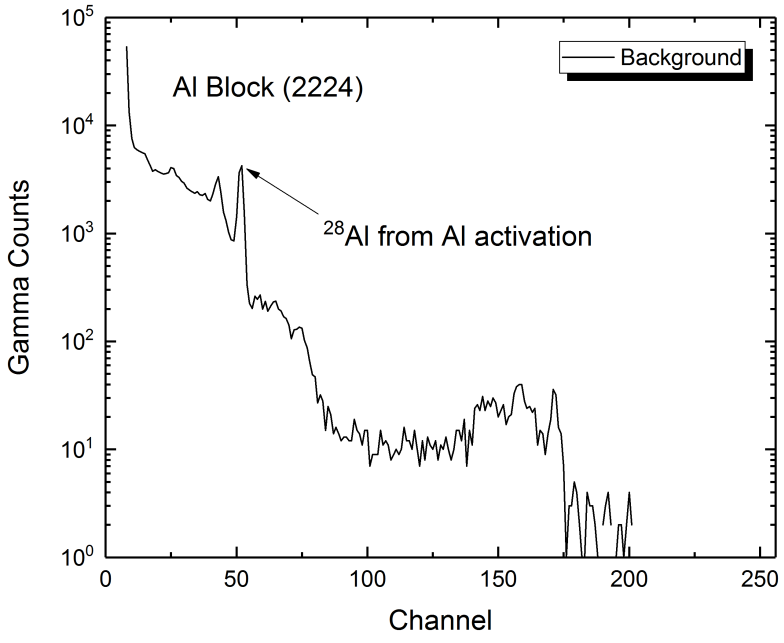

Figure 3.10 Background spectrum of an aluminum block measurement.

usually not observable due to lower level discriminator settings. When both the de-excitation 0.789 MeV gamma and the decay electron are absorbed by the detector, a hump feature, marked by 'C1' in Figure 3.4 is formed. The left edge of the hump corresponds to the energy of the gamma, which is 0.789 MeV, and the hump ranges from 0.789 MeV to approximately 1.044 MeV, as a result of both the gamma and the electron depositing their energies in coincidence.

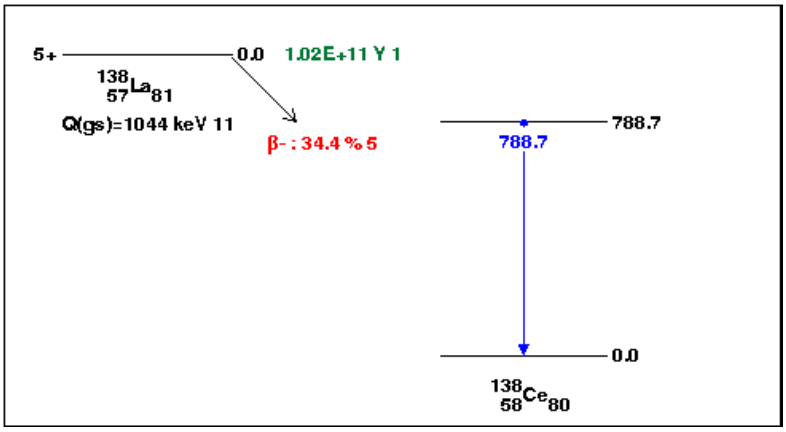

Figure 3.11 $^{138}_{57}$La β^- decays to $^{138}_{58}$Ce. The branching ratio is 34.4%. Data from ENSDF data files.

For 65.6% of the probability, $^{138}_{57}$La decays to excited $^{138}_{56}$Ba through electron capture, as shown in Figure 3.12. The decay product subsequently de-excites to ground state by emitting a 1.436 MeV gamma. At the same time, as an electron is absorbed by the ^{138}La nucleus, the lower orbital electron vacancy has to be filled by upper orbital electron. The exact process how the electron vacancy is refilled is not unique, and involves X-ray emission, Auger electron emission, or combinations of both. Previous research[29] indicated that the energy of the emitted X-ray photon is on average either 35.5 KeV or 4.5 KeV, depending on the orbit the electron was in before being captured. The peak marked by 'C2' in Figure 3.4 is actually two peaks convolved. They correspond to 1.440 MeV, which is the sum peak of the ^{138}Ba de-excitation and the 4.5 KeV X-ray, and 1.471 MeV, which is the sum peak of the ^{138}Ba de-excitation and the 35.5 KeV X-ray. As the standard energy spectrum has only 256 channels, and extends to over 8 MeV, these two La peaks

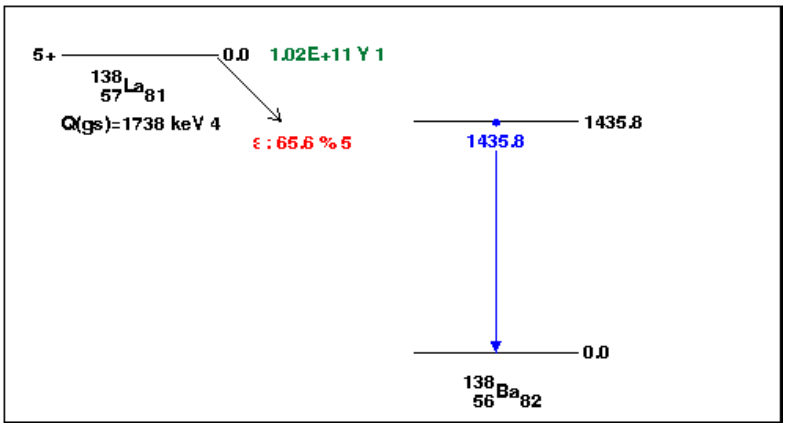

Figure 3.12 $^{138}_{57}$La electron capture decays to $^{138}_{56}$Ba. The branching ratio is 65.6%. Data from ENSDF data files.

usually shows as one slightly wider peak.

3.3 Spectra preprocessing

After the three raw spectra are acquired, two spectral preprocessing are required before entering the spectral elemental analysis stage. They are alignment and background subtraction

3.3.1 Alignment

Several factors may affect the gain settings, or scale, of the energy spectra. The factors include temperature, count rate, power supply stability, etc. Although significant gain shifting is not likely, small variations always exist. Figure 3.13 shows a comparison of the raw, unprocessed capture spectra of two separate measurements of a water tank. Misalignment can be clearly observed in the figure, especially around the oxygen activation peak.

To maintain a consistent measurement and analysis, by specification, the Tool defines that the energy spectra should have 256 channels, ranging from 0 eV to 8.823 MeV, such that the 2.223 MeV hydrogen peak centers at exactly the middle of the 65$^{\text{th}}$ channel. To maintain this standard, two types of alignment are implemented on the Tool:

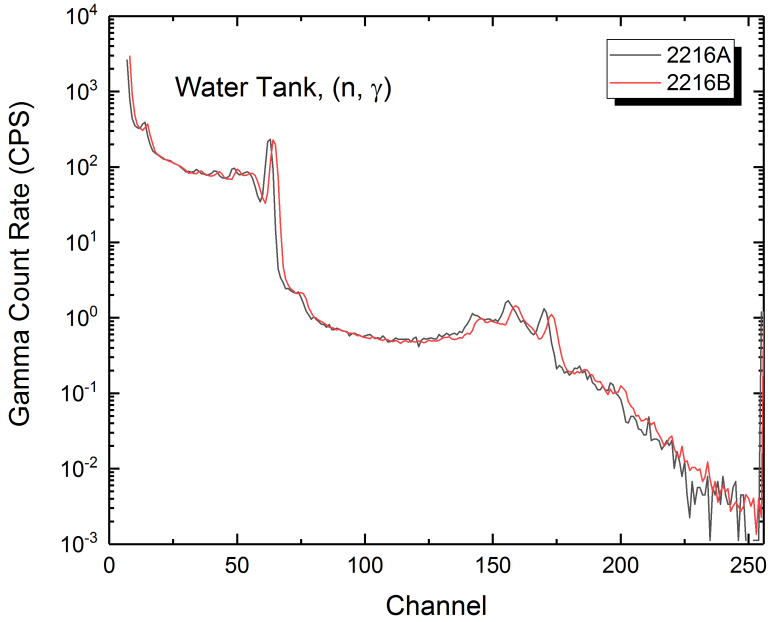

Figure 3.13 Unprocessed capture spectra of two separate water tank measurements. 2216A and 2216B are measurement IDs.

1. The firmware on the Tool actively searches for the hydrogen peak during measurement, and adjusts the amplifier gain setting to maintain the hydrogen's centroid.

2. After the spectra are measured, the processing code also searches for specific elemental characteristic peaks, which are scattered over the entire range of the spectra, and then realigns the spectra.

To perform the spectra alignment, two algorithms are needed: peak search and spectral rebinning.

Peak search

A peak search algorithm primarily estimates the centroid of a peak within specified channel range of a spectrum. Optionally, the algorithm can also estimate the amplitude of the peak and the background. Currently there are two methods implemented.

1. Differentiation method. This method first applies two filters to adjust the shape of the spectrum, then differentiates the spectrum and finds the zero crossing points.

The first filter to be applied is a Gaussian filter to smooth the spectrum. The filter to be convoluted with the measured spectrum is shown in Figure 3.14. The FWHM of the filter is 4.43. Take the water tank measurement shown in Figure 3.13 as an example. Figure 3.15 shows what the spectrum looks like after the Gaussian filter is applied to the raw capture spectrum. Notice that the entire spectrum is much smoother, and the peaks are broadened. As the primary purpose is only to find the centroids of the peaks, limited broadening does not affect the results.

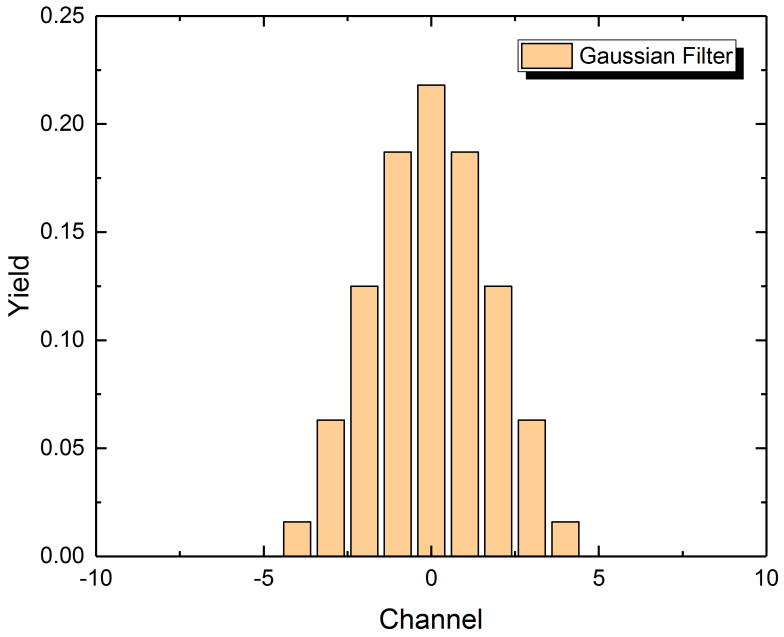

Figure 3.14 The Gaussian filter used for smoothing the measurement spectrum. The FWHM$\approx$ 4.43.

The second filter to be applied is a background removal filter to make the peaks more pronounced. Here the 'background' does not refer to the radiation background. Instead, this background removal filter treats the spectrum as a series of pulses, and removes the positive component of the signal by applying the removal filter shown in Figure 3.16. After the filter is applied, the sum of counts of the entire spectrum is 0. Figure 3.17 shows a comparison of the raw measurement and the spectrum after the Gaussian and background removal filters are applied. Notice

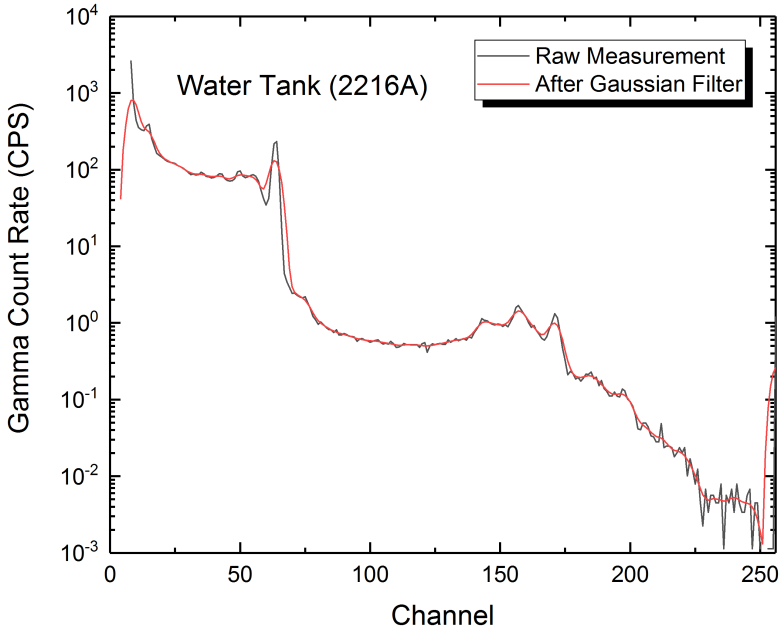

Figure 3.15 Comparison of the raw capture spectrum of water tank measurement (2216A) and after the Gaussian filter is applied.

that as the processed spectrum has both positive and negative signals, so that logarithm ordinate can no longer be used. Due to the amplitude, the shape of the processed spectrum between channel 130 to channel 190, corresponding to the oxygen activation peaks, is not clearly visible. Figure 3.18 shows the details by zooming to channel 130 to 190, which clearly shows three peaks.

Finally, the spectrum is differentiated, and a typical differentiation method is used to identify the centroids of the peaks. Figure 3.19 shows how the shape of the spectrum changes after each filter is applied, and how the oxygen activation peak and its escape peaks are identified using this algorithm. The dashed lines mark the centroids of the peaks identified using differentiation method. The centroids of the three peaks shown in the figure in channels are: 143.20, 156.83, 170.72.

2. Peak fitting method. It is known that the gamma peaks measured by scintillation detectors are Gaussian peaks[30][31]. To correctly estimate the centroid and amplitude of the peak itself, accounting for the background, a small portion of the spectrum, near the vicinity of the peak of interest, can be fitted to a model. After a few trials, it was found that the Gaussian distribution formula with a cu-

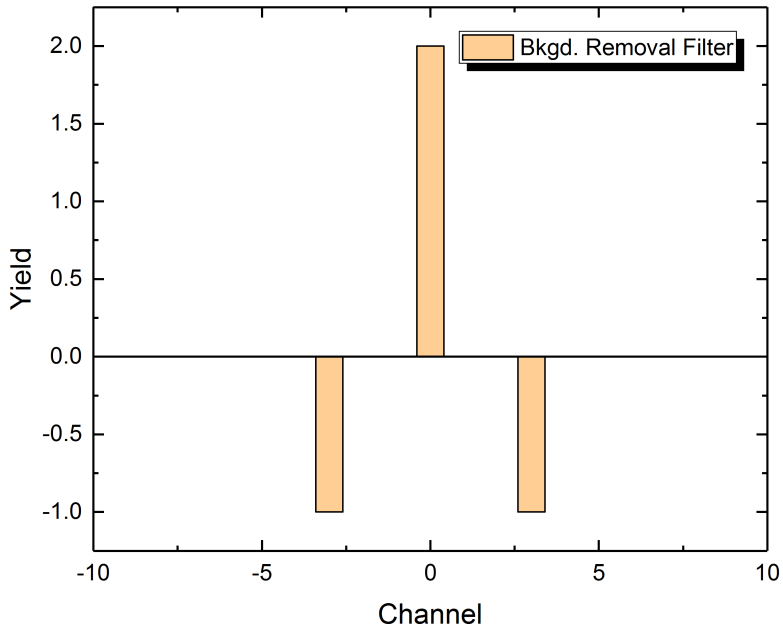

Figure 3.16 The background removal filter used for removing the positive component of the spectrum.

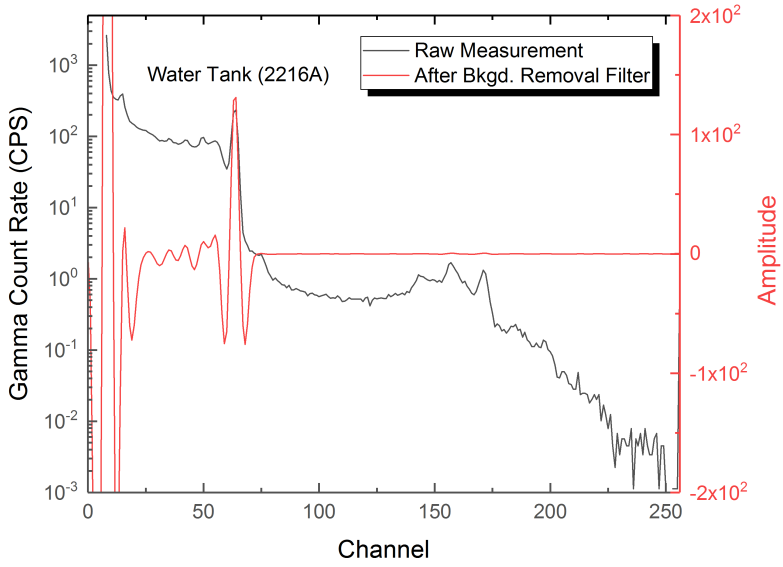

Figure 3.17 Comparison of the raw capture spectrum of water tank measurement (2216A) and after application of the Gaussian filter and background removal filters.

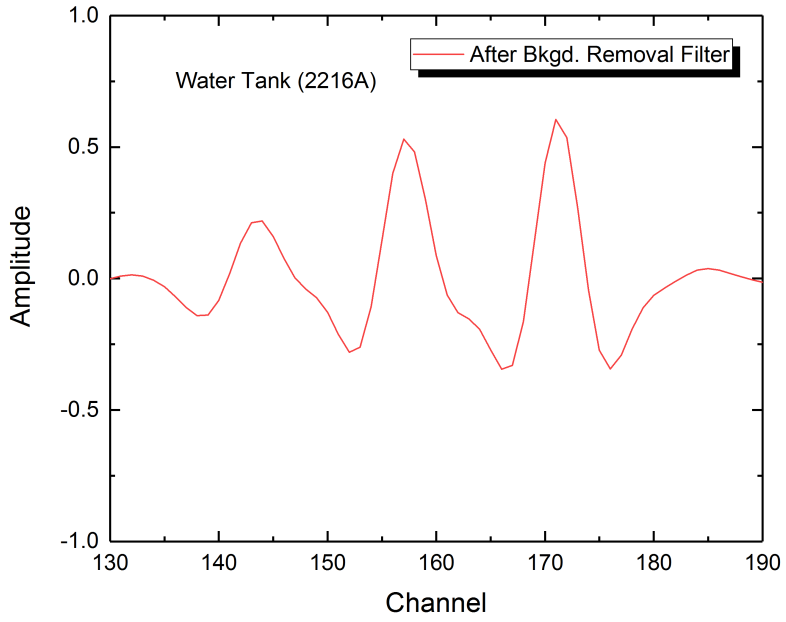

Figure 3.18 Figure 3.17 zoomed to channel 130 to channel 190 to show the details.

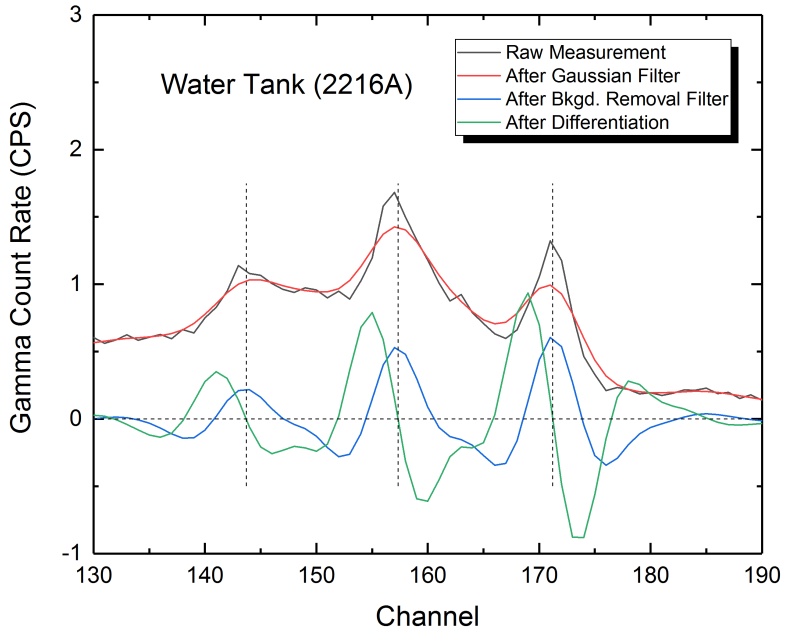

Figure 3.19 Water tank capture spectrum measurement zoomed to channel 130 to channel 190 showing shapes of the spectrum after each filter is applied. The dashed lines mark the three peaks identified by the algorithm in this range.

bic polynomial background term would generate satisfactory results in most cases. Mathematically, the model is

$$y(x) = \frac{A}{\sqrt{2\pi\sigma^2}} \exp^{-\frac{(x-\mu)^2}{2\sigma^2}} + c_0 + c_1 x + c_2 x^2 + c_3 x^3 \tag{3.2}$$

where, x is the independent variable, and for this particular fitting, is always 0.5 or a positive integer plus 0.5, y is the number of counts in the $(x + 0.5)^{\text{th}}$ channel, A is a coefficient proportional to the amplitude of the peak, μ is the centroid of the peak, σ is the standard deviation of the peak, c_0, c_1, c_2, and c_3 are the polynomial coefficients.

Equation 3.2 may be difficult to fit using typical nonlinear fitting method, because there are 7 parameters in largely different magnitudes. A fitting code based on Equation 3.2 and an improved linear-nonlinear joint fitting method, which will be elaborated in Chapter 4, has been developed and solves the problem nicely.

As an example, use the capture spectrum of the water tank measurement 2216A again, but take the gamma counts instead of the count rate, use the portion from channel 163 to channel 184, and fit to Equation 3.2. The fitting shows the centroid of the peak is 170.71, which is almost identical to that estimated by the differentiation method (170.72). In addition, the fitting also shows the value of the A parameter, which is proportional to the amplitude of the peak, is 3348, and the standard deviation of the peak is 1.61. The overall reduced χ^2 of the fitting is 1.22, which indicates a good fit. The fitted peak, background, and measurement are shown in Figure 3.20.

Both the differentiation method and the fitting method can be used for estimating properties of peaks, but they are not interchangeable. The differentiation method can both identify peaks and estimating the centroids of the peaks it identifies. In addition, it has no requirements on the shapes of the peaks, or in other words, the differentiation methods estimates the local maximum only. This is especially helpful when the centroid of a convolved peak is of interest. For example, the ^{138}La peak, which is actually two peaks convolved, with the 1.471 MeV peak slightly higher. The fitting method, on the other hand, would have difficulties fitting peaks which are not clean.. It will not estimate the centroid of the ^{138}La 1.471 MeV peak correctly. Neither can the fitting method be used for identifying peaks by itself. The strength of the fitting method is that it can

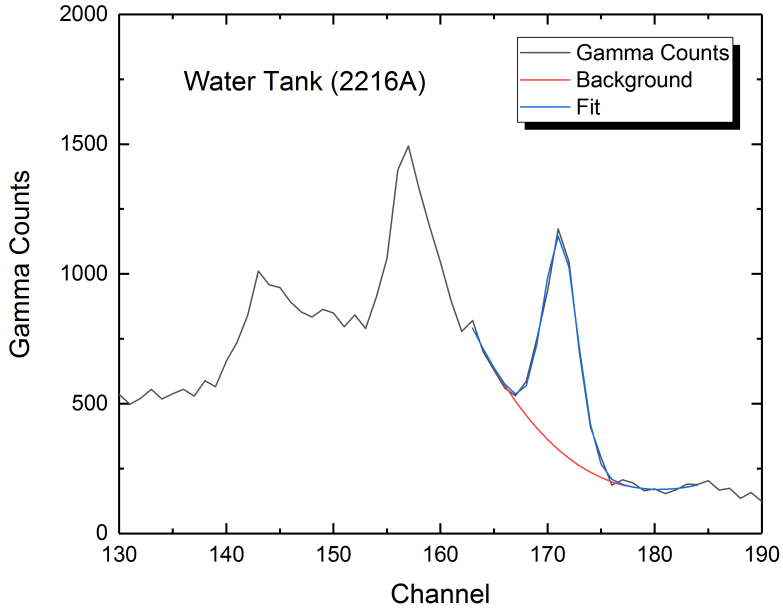

Figure 3.20 Oxygen peak of the capture spectrum of the water tank measurement fitted to Equation 3.2.

estimate the amplitude of the peak, which can be helpful in spectral analyzing during the development phase. The elemental standard generation work introduced in Chapter 4 relies on the peak fitting to a great extent.

Rebinning algorithm

Rebinning, or sometimes also referred to as gain shifting or alignment, is a very typical spectrum adjustment operation, which numerically contracts, expands, and/or shifts the energy spectrum. Rebinning is characterized by two parameters, the multiplicative factor M, and the additive factor A. $M > 1$ is analogous to tuning up the gain setting of the amplifier when taking the measurement, which expands the spectrum, and thus the energy range after rebinning is narrower. $M < 1$ means the spectrum is contracted, and thus the energy range after rebinning is wider. $A > 0$ means the entire spectrum is shifted towards the higher energy side (right) as a whole, and $A < 0$ means the spectrum is shifted towards the low energy side.

By definition, a spectrum measured by the Tool has 256 channels. The specification also defines a continuous real axis spanning from 0 to 256, such that, the i^{th} channel spans from $i - 1$ to i on the real axis. Figure 3.21 illustrates the relation of the continuous

scale to the discrete channel system. For example, the 5^{th} channel ranges from point 4 to point 5 of the continuous scale.

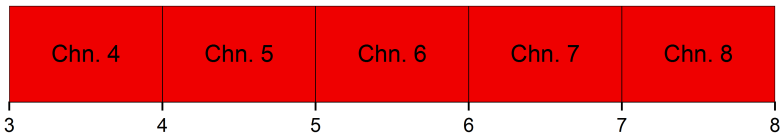

Figure 3.21 By definition, the i^{th} channel ranges from point $i-1$ to point i on the continuous scale.

Rebinning is essentially redistributing the counts from each channel of the original spectrum to corresponding channels of the new spectrum, according to the specified parameter M and A. For an arbitrary channel i, rebinning redistributes the counts between point $i-1$ to i, to the channel(s) that covers the range $(i-1) \times M + A$ to $i \times M + A$. Or vice versa, the counts in the j^{th} channel of the rebinned spectrum come from the range $(j-1-A)/M$ to $(j-A)/M$ of the original spectrum.

The rebinning algorithm used in this research is very simple to implement. The steps of the calculation can be summarized as:

1. Calculate the cumulative sum of the original spectrum to be rebinned.
2. For each boundary of each channel of the new spectrum, that is, 0, 1, 2, ..., 256, calculate its corresponding value on the continuous scale of the original spectrum.
3. Linearly interpolate the cumulative sum to calculate the values corresponding to the x calculated in the 2^{nd} step.
4. The differences between two adjacent elements of the array calculated in the 3^{rd} step is the new spectrum.

The following Matlab script is an example implementation of the method described in this section. This code is for illustration purpose only, and may not be the simplest or most efficient implementation.

```
function gs_spe = gainshift(spe, m, a)
    nChns = numel(spe);
    raw_x = 0 : nChns;
```

```
rawspe_cumsum = cumsum([0, spe]);
gs_x = (raw_x - a) ./ m;
gsspe_cumsum = interp1(raw_x, rawspe_cumsum, ...
    gs_x, 'linear', 'extrap');
gs_spe = diff(gsspe_cumsum);
```

Example

Figure 3.22 shows an example of alignment. Table 3.1 summarizes the calculation results.

In Figure 3.22, the black curve is the unprocessed capture spectrum of a sandstone with water borehole measurement (measurement ID 2211A). The spectrum is comprised of contributions from capture hydrogen, capture silicon, and background. Three peaks are selected for peak search: 2.223 MeV hydrogen peak, 3.539 Si peak, and 4.934 Si peak. Their standard locations, at where they are expected to be found in a standardized spectrum, are listed in the 3$^{\text{rd}}$ column 'Std. Chn.' of Table 3.1. A differentiation peak search, as described in this section, is ran to find the actual centroids of these peaks in the unprocessed spectrum. The centroids of the peaks are listed in the 4$^{\text{th}}$ column 'Found in Chn' of Table 3.1.

Table 3.1 Peaks used for the alignment, and their centroids before and after the alignment. Based on these peaks, $M = 1.0678$, $A = -1.879$.

Peak	Energy (MeV)	Std. Chn.	Found in Chn.	Realigned to Chn.	Δ
H	2.223	64.52	62.16	64.49	0.03
Si	3.539	102.72	98.00	102.77	-0.05
Si	4.934	143.20	135.84	143.18	0.02

Next, data in column 3 and 4 of the table are used to run a linear fit to find the multiplicative factor M and A to realign the peaks, that is:

$$\text{Std. Chn.} = M \times \text{Found in Chn.} + A \tag{3.3}$$

For this particular example, the fitting gives $M = 1.0678$, and $A = -1.879$.

Finally, the spectrum is realigned using the parameters calculated, obtaining the red

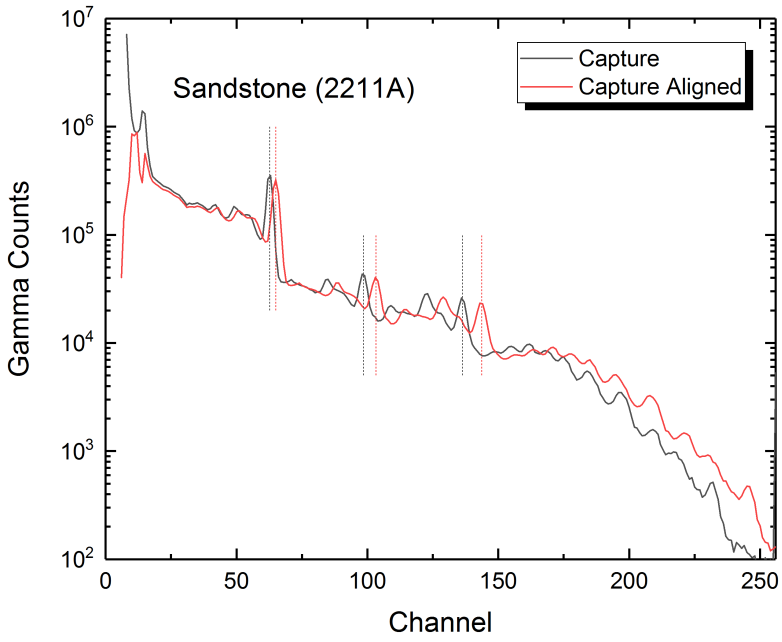

Figure 3.22 Capture spectrum of sandstone with water borehole measurement before and after spectral alignment. The dotted lines indicate the peaks used for the alignment, and their centroids before and after the alignment.

curve in Figure 3.22. The black and red dotted lines in the figure mark the centroids of the three peaks selected for alignment. As M and A are calculated using a fitting, there is still a small displacement after the alignment. Column 5, 'Realigned to Chn.', of Table 3.1 shows the centroids of the peaks after the alignment, and column 6 'Δ' shows the uncertainty of each peak. From the results, the maximum uncertainty is only 1/20 of a channel, which indicates a very good fit.

3.3.2 Background subtraction

As a step in the preprocessing stage, the background radiation spectrum can be subtracted from the burst and capture spectra. It is not impossible to use the background spectrum as a standard in the spectral deconvolution step. However, it is much preferable to have the background subtracted before the elemental analysis for at least two reasons:

1. The background radiation contribution is normally lower than most formation elements' contributions to the burst spectrum or the capture spectrum. Therefore,

deconvolution using the measured background spectrum as a standard has larger uncertainty.

2. As the neutron generator firing sequence is well defined, the measurement time of each spectrum is known, and subtracting the background spectrum from the burst and capture spectra is just a matter of alignment followed by a simple subtraction.

As part of the calculation, the deconvolution method to be elaborated in Chapter 4 requires the variance of each channel of the spectrum, which is, according to Poisson statistics theories, approximately the number of counts, i.e.,

$$\sigma^2(Y_i) \approx Y_i \tag{3.4}$$

where σ^2 is variance, and Y_i is the number of counts in the i^{th} channel. Therefore, it is preferable to manipulate the gamma counts spectra instead of the count rates spectra.

To subtract the background from the burst and capture spectra, first align these three spectra to the standard, using the method described in Section 3.3.1. Then simply perform a channel by channel subtraction for the two spectra, with a corresponding subtraction coefficient. This subtraction coefficient accounts for the difference in measurement time, and is 9.75 for the capture and 3 for the burst.

Figure 3.23 shows the background subtraction from the capture spectrum. The measured capture spectrum has a higher fraction of background, and thus the changes are clearly observed after the subtraction. Notice that the peaks highlighted by the yellow circles in the figure are removed after the subtraction. The amplitude of the background spectrum is multiplied by 9.75 to account for the difference in measurement time, on order to show the relative amplitude of the background to the capture.

Figure 3.24 shows the background removal from the burst spectrum. Note that the measured burst spectrum has a much smaller fraction of background than the capture. Again, the amplitude of the background spectrum is multiplied by 3 to account for the difference in measurement time, in order to show the relative amplitude of the background to the burst.

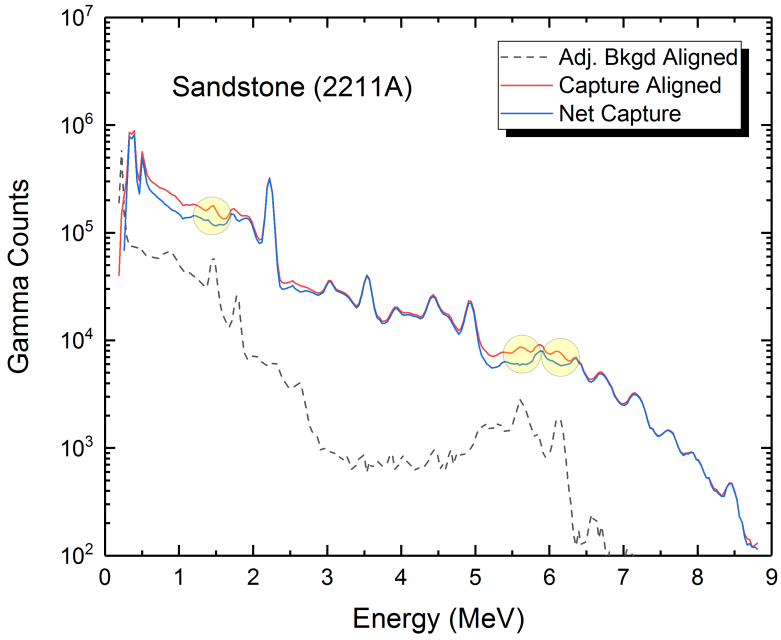

Figure 3.23 Subtraction of the background radiation spectrum from the capture spectrum. The yellow circles highlight some significant changes after the subtraction.

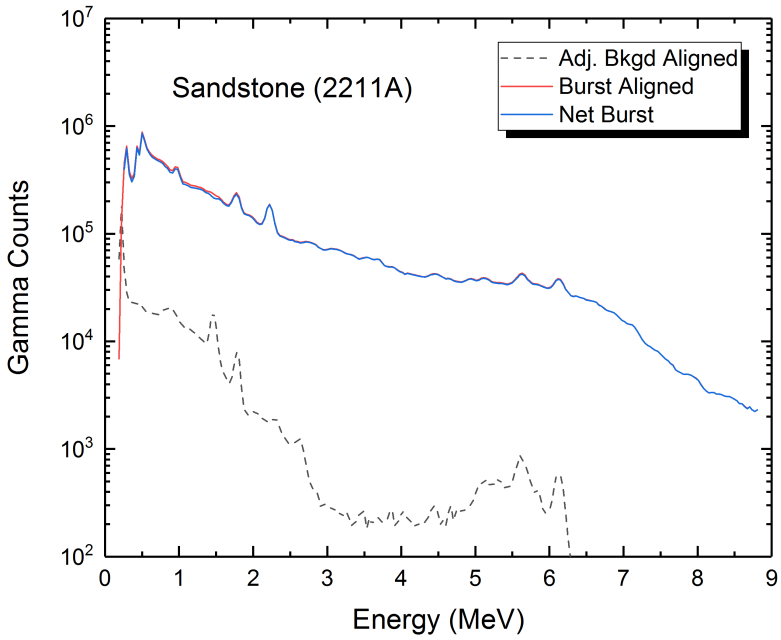

Figure 3.24 Subtraction of the background radiation spectrum from the burst spectrum.

Chapter 4

Spectral Analysis

4.1 Overview

Spectral analysis is the second step of the entire processing chain of the Tool. Figure 4.1 shows a flow chart of the spectral analysis stage. From previous stage, which is the spectral acquisition and preprocessing stage described in Chapter 3, two composite spectra are passed to the spectral analysis stage: the net capture spectrum, which is the measured capture spectrum with the radiation background subtracted, and the net burst spectrum, which is the burst spectrum with the radiation background subtracted.

Next, the processing forks into two branches. In one of the branches, the net capture spectrum is deconvolved into elemental counts, using a set of predetermined elemental capture standards, and is further normalized to elemental yields. The other branch is slightly more complicated. The net burst spectrum is composed of contributions from inelastic scattering gammas and capture gammas. The capture contribution should be excluded from the spectrum in some way in order to correctly analyze the elemental inelastic counts. The capture spectrum can be either used as a component spectrum to fit the burst spectrum together with other inelastic elemental standards, or the capture spectrum can be subtracted from the burst spectrum before deconvolution, to generate a pure inelastic spectrum. In addition, it is also possible to limit the elemental standards used for deconvolving the inelastic spectrum based on the deconvolution results of the capture spectrum. Other than that, the processing of the net burst spectrum is identical to that of the net capture spectrum. It has to be noted that, the elements that are involved in the calculation of these two spectra are usually not the same. For example,

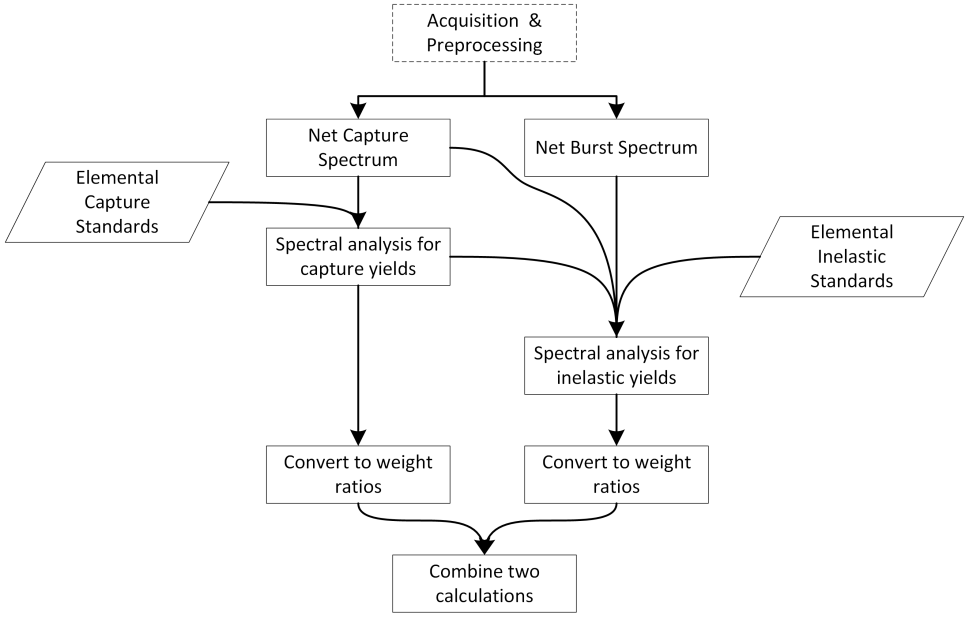

Figure 4.1 Overview of the spectral analysis process.

hydrogen can only appear in the capture spectrum, and oxygen only appears in the burst spectrum.

After two spectra are deconvolved, the elemental counts derived from each spectrum are converted to elemental weight ratios using predetermined elemental sensitivity factors, respectively. Finally, the elemental weight fractions from two spectra may be combined to form a comprehensive set of solutions, which will be further processed using geology theories for estimating the lithology and mineralogy of the sample formation.

In this chapter, contents regarding the elemental standards are elaborated in Section 4.2. Contents regarding the deconvolution algorithms are elaborated in Section 4.3. Conversion from elemental yields to elemental weight concentrations is briefly introduced in Section 4.4.

4.2 Elemental standards

4.2.1 Definition

In more specific terms, and in the context of neutron activation elemental analysis, an elemental standard is a characteristic energy spectrum that represents the detector's

response to gammas originating from either the neutron capture or inelastic scattering reactions with a specific element.

Strictly speaking, the elemental standard of an element depends on the composition of the sample and the measurement environment, because any change in the sample composition or the environment will affect the neutron distribution, gamma generation, and gamma transportation.

Figure 4.2 shows a comparison of two aluminum capture standards generated under different environments. The same sample, which is a pure Al block, is used for both measurements. The difference is that, in one measurement, the borehole is filled with water, and in the other case, the borehole is left empty. From the comparison, it is evident that the red curve, which is the measurement with water borehole, has more features. The explanation for this particular case is that, with water in the borehole, the 14 MeV fast neutrons thermalizes quicker and with fewer scattering reactions. The capture gammas are generated closer to the detector, and thus the characteristic gammas have higher probability of reaching the detector without loosing energy on the way.

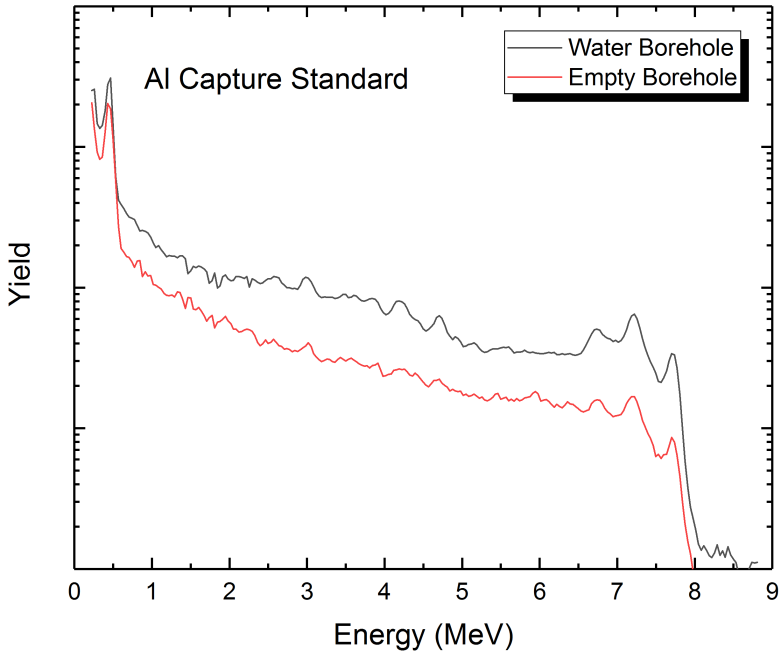

Figure 4.2 Comparison of Al capture standards measured under different environment.

In practice, not all factors are important. For example, many earth formations are similar in physical properties, and the gamma transmission in a formation, whether it is a sandstone or a limestone, are similar. For capture standards, the presence of water does have a bigger influence, because H acts as a strong moderator and allows capture reactions to take place closer to the detector. It is desirable to measure the standards in a water borehole, to emulate the environment of real well logging. For inelastic standards, making measurements in water borehole or empty borehole makes limited difference, because inelastic gammas are generated in the first few collisions, and the tool is usually eccentered. In addition, the Tool only uses 0.7 MeV to 8 MeV of the spectra for deconvolution, where the linearity is better than the portion of the spectrum below 0.7 MeV.

The Tool is designed to be capable of measuring the following elements, all of which are common elements in the earth formations or the borehole:

- Capture: Al, Ca, Cl, Fe, Gd, H, K, Mg, S, Si, Ti
- Inelastic: Al, Ca, C, Fe, Mg, O, S, Si

4.2.2 Generation

For an arbitrary element X, its elemental standard is generated by taking measurements of a substance that has a significant fraction of X. The measured spectrum may include contributions from X, as well as undesired element Y, Z, etc, that are also present in the sample. The inclusion of contributions from Y and Z are, although undesirable, often inevitable. For example, capture H is almost always present in capture measurements.

Next, the contributions from all elements other than X are subtracted from the measurement to make the standard of X. The contributions of other elements to be subtracted are also in the form of elemental standards, and need to be determined before processing that of X.

MCNP[32] program can also be employed to generate elemental standards. A simpler but more time consuming approach is to use the same method as generating the empirical standards, as illustrated above. Alternatively, a better method is to modify the MCNP source code, to make the program record the isotope that generates each gamma recorded by the detector. A Monte Carlo code called 'CEARCPG' developed by Xiaogang Han[11] implemented the second method, and is capable of generating the standards efficiently.

Previous experience indicates that the simulations still suffer from disagreements with the experiments due to various reasons, such as inaccurate cross sections, inability of modeling the PMT, etc. Nevertheless, the modeled standards can act as very good references in terms of predicting if a specific characteristic peak is visible on the spectrum, etc.

Example

The followings is an example of generating a Si capture elemental standard empirically.

The first step is to decide on the choice of sample. For Si, sandstone, whose chemical composition is SiO_2, is a good choice. Si makes 1/3 of the compound by atomic fraction, or 46.7% by weight. Oxygen has very small capture cross section, and makes hydrogen (from the borehole) the only element needs to be subtracted from the measurement. In reality, 100% pure SiO_2 is not possible. For this particular measurement, a $> 99\%$ purity large sandstone is used. The remaining $< 1\%$ is small enough to be ignored.

A hole is drilled in the rock, and is filled with water. The tool is then placed in the borehole to take the measurement. Figure 4.3 shows the measured capture spectrum, after typical alignment and background subtraction operations.

In the spectrum, a strong hydrogen capture 2.223 MeV peak is clearly visible, due to the presence of water in the borehole. The contributions from hydrogen needs to be subtracted next. The hydrogen capture standard, as shown in Figure 4.4, is measured by placing the Tool in a large water tank. As oxygen has very low capture cross section, the measured capture spectrum would be the hydrogen capture standard, after typical alignment and background subtraction. Hydrogen capture standard should be the first capture standard to be determined, as all the subsequent measurements need to have the hydrogen capture contribution subtracted.

Because the percentage of hydrogen capture contribution is not known, there is no automated method of performing the subtraction. This is also the case for all the subtractions when making other elemental standards. To reduce the uncertainties of this operation, some knowledge of the spectrum to be subtracted is needed. If there is at least one peak that is known to be part of a elemental standard that needs to be subtracted (H peak for this case), the amplitude of this peak in the measurement and the standard can be measured. Then, the peak height ratio can be used as a reference for determining the subtraction factor.

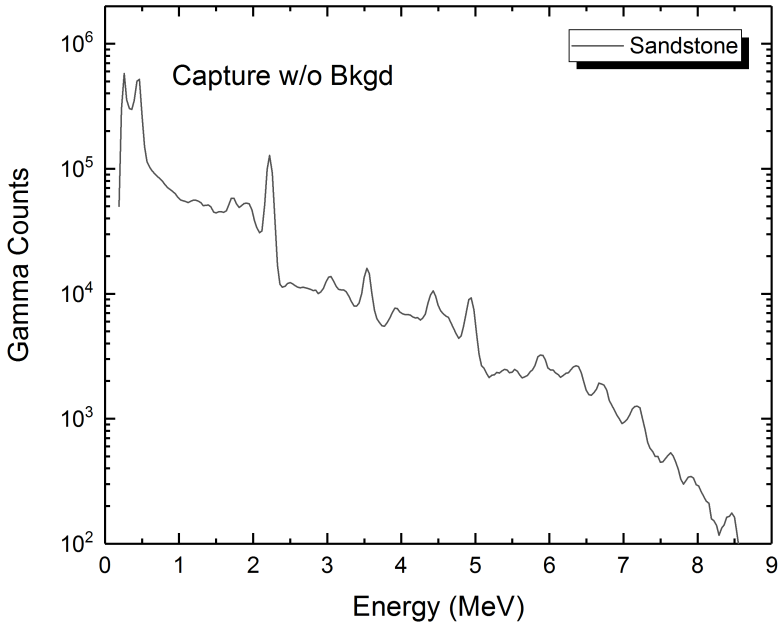

Figure 4.3 Capture spectrum of a sandstone sample with water in the borehole. Spectrum has been aligned and background subtracted.

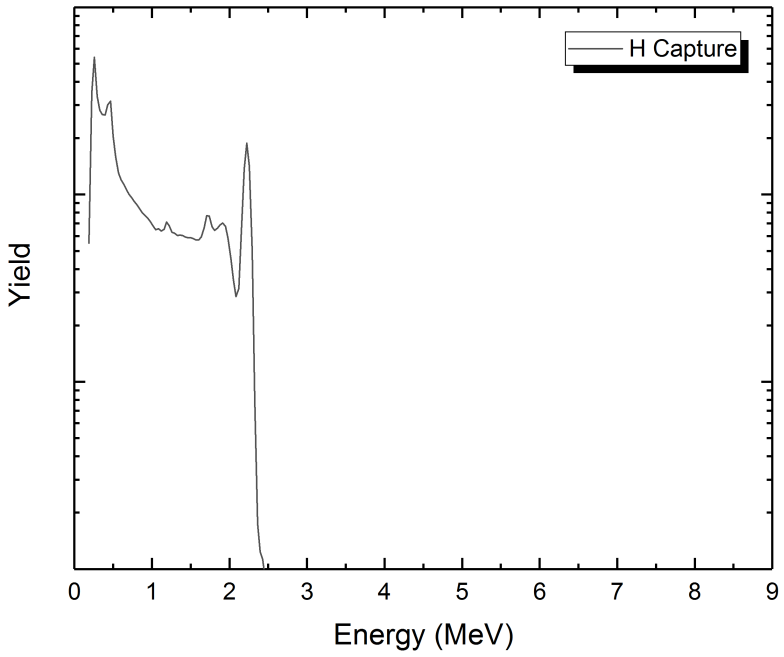

Figure 4.4 Hydrogen capture standard.

By using the peak fitting code described in Section 3.3.1, it is determined that the amplitude factor of the H peak in the sandstone measurement spectrum is 3.397×10^5, and is 5.550×10^5 in the H standard. A good estimate of the subtraction factor is then:

$$\frac{3.397 \times 10^5}{5.550 \times 10^5} = 0.612$$

Due to the varying parameters of each measurement, after the subtraction coefficient is determined, there are still a few parameters that may need adjustments, including relative shifting and the spectral broadening. These are more difficult to be determined quantitatively without visual aid.

A GUI code called 'SpeStripping' was developed to perform the subtraction manually. Figure 4.5 shows a snapshot of the interface. On the bottom half of the interface is a plot, showing the 'Convolved Spectrum', which is the capture sandstone measurement in this example, and the 'Component Spectrum', which is the hydrogen capture standard in this example. The yellow curve in the plot, marked as 'After Subtraction', is the residue spectrum after the convolved spectrum and component spectrum are adjusted for shifting and resolution, and the adjusted component spectrum subtracted from the adjusted convolved spectrum. The adjustment factors are adjusted and indicated by the first 4 slider bars on the top half of the interface. The subtraction factor is adjusted and indicated by the 5^{th} slider bar, named 'Multiplier'. The two text boxes above the plot are used for adjusting the upper and lower limits of the multiplier slider bar. The two text boxes below the plot are used for adjusting the upper and lower limits of the ordinate of the plot. For this example, the hydrogen standard is shifted to the left by less than 1/10 of a channel, the sandstone measurement is broadened by $\sigma = 0.23$, and the hydrogen standard's subtraction coefficient is 0.612, as calculated above.

4.2.3 Considerations

The qualities of the standards are of critical importance to the determination of elemental yields. The generation of elemental standards should be considered as a complex project that requires thorough understanding and planning. Some factors to consider when making such experiment plans include:

- The measurement time is ideally as long as reasonably achievable, but the gain settings of the device may shift during measurement, giving rise to slightly poorer

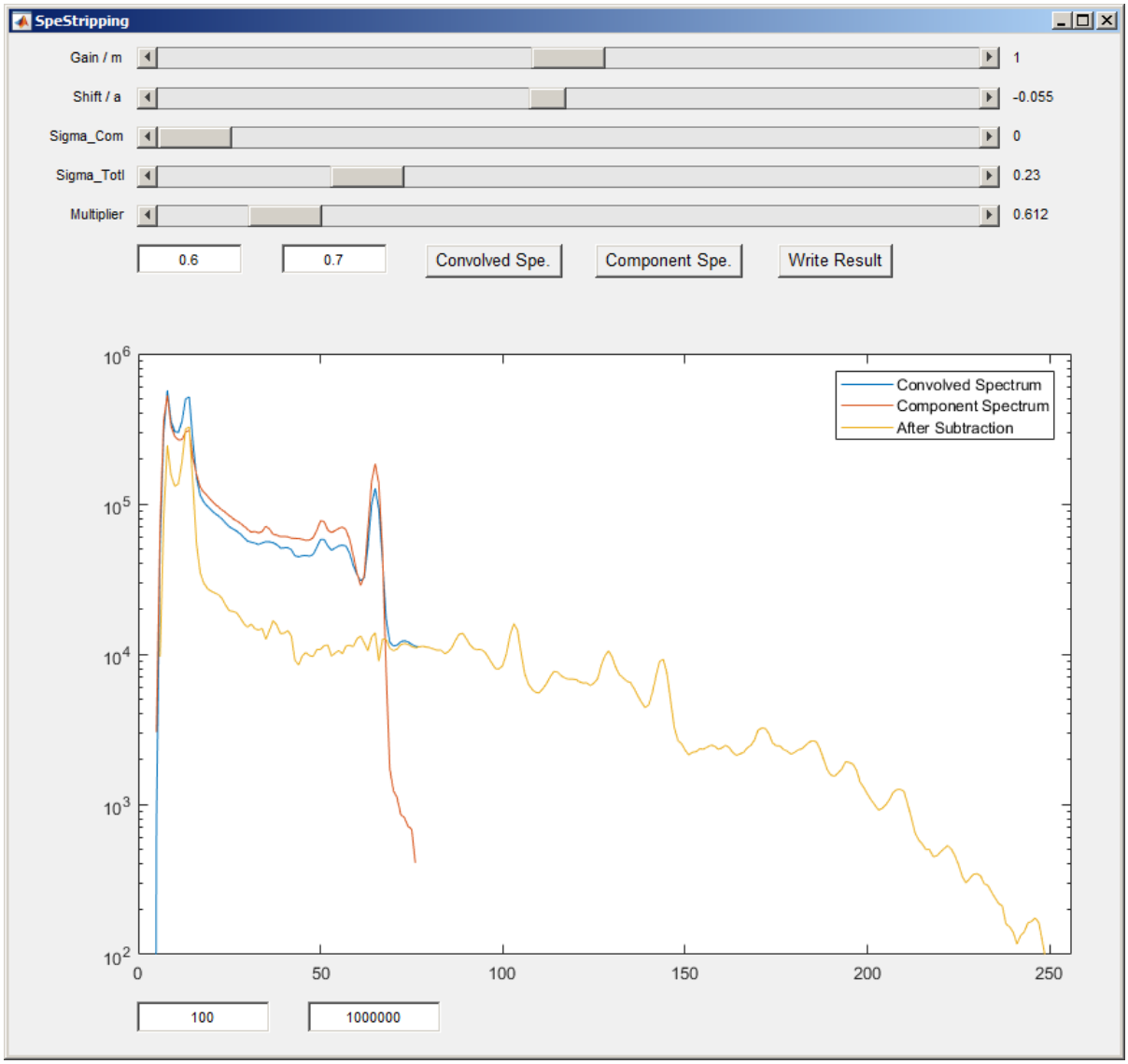

Figure 4.5 Snapshot of the SpeStripping code. The blue curve is the capture spectrum of the sandstone measurement. The red curve is the hydrogen capture standard. The yellow curve is the residue curve after subtracting the H standard from the measurement, after the adjustments characterized by the parameters shown on top of the plot.

resolutions. In addition, due to heat dissipated by components of the tool, longer measurement time may also increase the temperature of the detector, which degrades the resolution.

- The sample to be measured should have a significant amount of the element of interest. An elementary substance is usually not available for various reasons, such as the elementary substance may be gaseous (hydrogen), or not chemically stable (sodium). If that is the case, the selected sample should have a significant amount of the element of interest. For example, to measure the capture standard of Si, sandstone which is SiO_2 is a good choice.

- Although the elemental standard is very unique, some of the characteristic gammas may overlap with those of another element. For example, Al has two characteristic peaks at 7.693 MeV and 7.724 MeV, and Fe has two characteristic peaks at 7.631 MeV and 7.646 MeV. Therefore, when measuring the standard of Al or Fe, the existence of the other element is highly undesirable.

- Each time a component spectrum has to be subtracted from the measurement, such as subtracting the hydrogen spectrum from the Al block with water borehole measurement, the spectrum degrades slightly. It is desirable to use a sample with simpler chemical composition and less components in the spectrum.

4.3 Deconvolution algorithms

4.3.1 Overview

The deconvolution algorithm is another critical component of the processing chain. It resolves the elemental counts, which are further normalized to elemental yields, from the sample measurements and predetermined elemental standards. An important assumption[33][34] which made this deconvolution much easier is that, the spectral response of a sample that is composed of contributions from multiple elements, can be approximated by a linear superposition of these individual elemental contributions. For example, if the sample is a mixture of Ca and Mg, then the measured capture spectrum of this sample is the summation of the Ca capture standard and the Mg capture standard, each multiplied by a coefficient representing the relative amount of each element.

In the most simplified model, if m is the number of channels of a spectrum, n is the number of elements to be resolved, $\boldsymbol{X}$ is an $m \times n$ matrix that stores n elemental standards, each has m channels, $\boldsymbol{Y}$ is a column vector of size m that stores the measurement spectrum, according to the assumption,

$$\boldsymbol{X} \cdot \boldsymbol{\beta} \approx \boldsymbol{Y} \tag{4.1}$$

In this model, the value of m is up to 256 for the Tool, and the value of n is typically about 10. Therefore, having more data points than the unknowns makes this system an overdetermined system, and can be resolved by least squares fitting. Define column vector $\hat{\boldsymbol{Y}}$ as

$$\hat{\boldsymbol{Y}} = \boldsymbol{X} \cdot \boldsymbol{\beta} \tag{4.2}$$

Then the spectral deconvolution algorithm is to find $\boldsymbol{\beta}$ that minimizes χ^2, defined as

$$\chi^2 = \sum_{i=1}^{m} \frac{(y_i - \hat{y}_i)^2}{\sigma(y_i)^2} \tag{4.3}$$

where y_i and $\hat{y}_i$ are the i^{th} element of vector $\boldsymbol{Y}$ and $\hat{\boldsymbol{Y}}$, and $\sigma(y_i)$ is the standard deviation of the y_i measurement. Another frequently used metric that is related to χ^2 is reduced χ^2, which normalizes χ^2 to the degree of freedom of the system, defined as

$$\text{Reduced } \chi^2 = \frac{1}{m - n - 1} \sum_{i=1}^{m} \frac{(y_i - \hat{y}_i)^2}{\sigma(y_i)^2} \tag{4.4}$$

As nuclear counting follows Poisson distribution, a very helpful implication is

$$\sigma(y_i) \approx \sqrt{y_i} \tag{4.5}$$

and thus

$$\chi^2 \approx \sum_{i=1}^{m} \frac{(y_i - \hat{y}_i)^2}{y_i} \tag{4.6}$$

In reality, the problem is more complicated due to some constraints. Section 4.3.2 introduces the algorithm that solves the most simplified model with no complications. Section 4.3.3 introduces an algorithm that solves the simplified model with constrained solutions. Section 4.3.4 introduces the Levenberg-Marquardt nonlinear fitting method,

which allows the elemental standards to be adjusted for shapes. The LM method is the foundation of a hybrid algorithm introduced in Section 4.3.5, which significantly improves the computation efficiency of the LM method.

4.3.2 Weighted linear least squares

The weighted linear least squares ('Weighted LLS' or 'WLLS') algorithm is the simplest algorithm that solves the elemental counts vector $\boldsymbol{\beta}$ by making no adjustment to $\boldsymbol{X}$, placing no restriction on the values of $\boldsymbol{\beta}$, and taking the standard deviation of $\boldsymbol{Y}$ into consideration (thus 'weighted').

The algorithm solves $\boldsymbol{\beta}$ that minimizes χ^2 by differentiating χ^2 with respect to $\boldsymbol{\beta}$, and equating to 0, that is,

$$\frac{\partial \chi^2}{\partial \boldsymbol{\beta}} = 0 \tag{4.7}$$

To derive the expression, first rewriting the expression of χ^2 in matrix form

$$\begin{aligned}
\chi^2 &= \sum_{i=1}^{m} \frac{(y_i - \hat{y}_i)^2}{\sigma(y_i)^2} \\
&= (\boldsymbol{Y} - \hat{\boldsymbol{Y}})^T \boldsymbol{W} (\boldsymbol{Y} - \hat{\boldsymbol{Y}}) \\
&= (\boldsymbol{Y} - \boldsymbol{X}\boldsymbol{\beta})^T \boldsymbol{W} (\boldsymbol{Y} - \boldsymbol{X}\boldsymbol{\beta}) \\
&= (\boldsymbol{Y}^T - \boldsymbol{\beta}^T \boldsymbol{X}^T) \boldsymbol{W} (\boldsymbol{Y} - \boldsymbol{X}\boldsymbol{\beta}) \\
&= (\boldsymbol{Y}^T \boldsymbol{W} - \boldsymbol{\beta}^T \boldsymbol{X}^T \boldsymbol{W}) (\boldsymbol{Y} - \boldsymbol{X}\boldsymbol{\beta}) \\
&= \boldsymbol{Y}^T \boldsymbol{W} \boldsymbol{Y} - \boldsymbol{\beta}^T \boldsymbol{X}^T \boldsymbol{W} \boldsymbol{Y} - \boldsymbol{Y}^T \boldsymbol{W} \boldsymbol{X} \boldsymbol{\beta} + \boldsymbol{\beta}^T \boldsymbol{X}^T \boldsymbol{W} \boldsymbol{X} \boldsymbol{\beta}
\end{aligned} \tag{4.8}$$

where $\boldsymbol{W}$ is the weighting matrix, and is a diagonal matrix with $w_{ii} = 1/\sigma(y_i)^2$. Notice that each term of Equation 4.8 is a scaler, and $\boldsymbol{W}$ is symmetric, thus the second term equals the third term

$$\boldsymbol{\beta}^T \boldsymbol{X}^T \boldsymbol{W} \boldsymbol{Y} = (\boldsymbol{\beta}^T \boldsymbol{X}^T \boldsymbol{W} \boldsymbol{Y})^T = \boldsymbol{Y}^T \boldsymbol{W}^T \boldsymbol{X} \boldsymbol{\beta} = \boldsymbol{Y}^T \boldsymbol{W} \boldsymbol{X} \boldsymbol{\beta} \tag{4.9}$$

Substituting Equation 4.9 to Equation 4.8

$$\chi^2 = \boldsymbol{Y}^T \boldsymbol{W} \boldsymbol{Y} - 2\boldsymbol{Y}^T \boldsymbol{W} \boldsymbol{X} \boldsymbol{\beta} + \boldsymbol{\beta}^T \boldsymbol{X}^T \boldsymbol{W} \boldsymbol{X} \boldsymbol{\beta} \tag{4.10}$$

Next, differentiating χ^2 with respect to $\boldsymbol{\beta}$

$$\begin{aligned}\frac{\partial\chi^2}{\partial\boldsymbol{\beta}} &= \frac{\partial(\boldsymbol{Y}^T\boldsymbol{W}\boldsymbol{Y})}{\partial\boldsymbol{\beta}} - 2\frac{\partial(\boldsymbol{Y}^T\boldsymbol{W}\boldsymbol{X}\boldsymbol{\beta})}{\partial\boldsymbol{\beta}} + \frac{\partial(\boldsymbol{\beta}^T\boldsymbol{X}^T\boldsymbol{W}\boldsymbol{X}\boldsymbol{\beta})}{\partial\boldsymbol{\beta}} \\ &= 0 - 2\boldsymbol{Y}^T\boldsymbol{W}\boldsymbol{X} + (\boldsymbol{X}^T\boldsymbol{W}\boldsymbol{X}\boldsymbol{\beta})^T + \boldsymbol{\beta}^T\boldsymbol{X}^T\boldsymbol{W}\boldsymbol{X} \\ &= -2\boldsymbol{Y}^T\boldsymbol{W}\boldsymbol{X} + 2\boldsymbol{\beta}^T\boldsymbol{X}^T\boldsymbol{W}\boldsymbol{X}\end{aligned} \tag{4.11}$$

Equating Equation 4.11 to 0

$$\begin{aligned}-2\boldsymbol{Y}^T\boldsymbol{W}\boldsymbol{X} + 2\boldsymbol{\beta}^T\boldsymbol{X}^T\boldsymbol{W}\boldsymbol{X} &= 0 \\ \boldsymbol{Y}^T\boldsymbol{W}\boldsymbol{X} &= \boldsymbol{\beta}^T\boldsymbol{X}^T\boldsymbol{W}\boldsymbol{X} \\ (\boldsymbol{X}^T\boldsymbol{W}\boldsymbol{Y}) &= (\boldsymbol{X}^T\boldsymbol{W}\boldsymbol{X})\boldsymbol{\beta}\end{aligned} \tag{4.12}$$

Finally,

$$\boldsymbol{\beta} = (\boldsymbol{X}^T\boldsymbol{W}\boldsymbol{X})^{-1}(\boldsymbol{X}^T\boldsymbol{W}\boldsymbol{Y}) \tag{4.13}$$

gives the mathematical solution to vector $\boldsymbol{\beta}$ that minimizes χ^2. Notice that numerically, it is recommended to calculate $\boldsymbol{\beta}$ by solving the system of linear equation given by Equation 4.12 instead, for better computation efficiency.

The uncertainty of the fitting parameters can be calculated by[35]

$$\boldsymbol{\sigma}_{\boldsymbol{\beta}} = \sqrt{\mathrm{diag}([\boldsymbol{J}^T\boldsymbol{W}\boldsymbol{J}]^{-1})} \tag{4.14}$$

Notice that this formula is a general formula, and also applies to the other fitting methods introduced in this document.

The weighted LLS method is easy to implement. Matrix transposition, matrix multiplication, and linear system of equations solver are all mature methods, and can be found from various numerical calculation packages, such as MATLAB®, Intel®Math Kernel Library, and BLAS/LAPCK. The complete LLS solver is also available from various sources. The complete solver typically does not include the weighting matrix, but this could be easily remedied by preprocessing the $\boldsymbol{X}$ and $\boldsymbol{Y}$ matrices. The computation is very fast. On current computers, the computation of a typical case (≤ 256 channels, ≈ 10 elements) can be completed almost instantly.

Although the weighted LLS algorithm is the most fundamental method that solves the spectral deconvolution problem, it only solves the most simplified cases, and is not

very practical for real applications, because this algorithm does not constrain the value of the elemental counts vector $\boldsymbol{\beta}$. It is rather possible that negative values appear in the solution in favor of smaller χ^2, which does not make physical sense.

As a demonstration, a dolomite (chemical composition is $CaMg(CO_3)_2$) (n, γ) measurement spectrum is deconvolved using the weighted LLS method, with two sets of capture elemental standards. The first set includes standards for H, Ca, and Mg, which are all known to be present in the sample. The second set includes all three elements in the first set, as well as an interference Si standard which is known to be not present. The standards are shown in Figure 4.6. The comparison of the measurement and the fit using both sets of standards are shown in Figure 4.7.

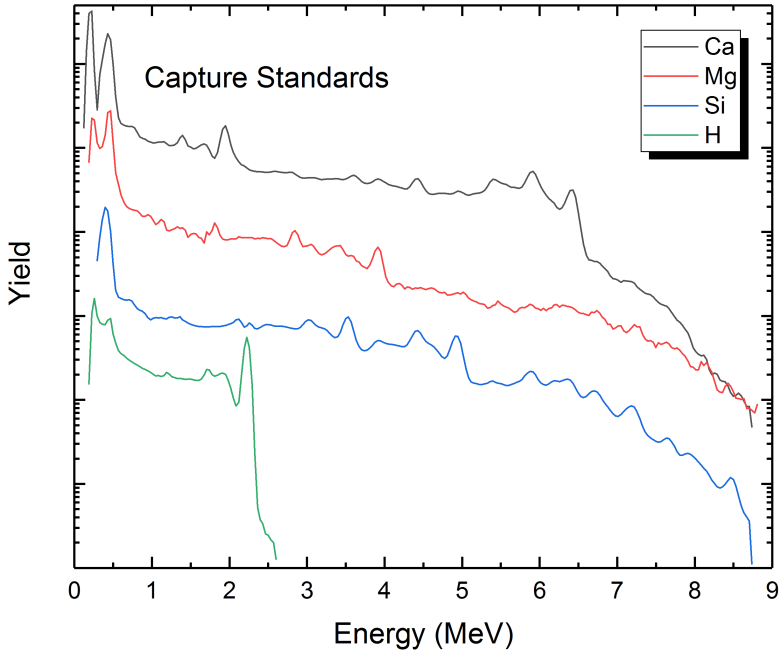

Figure 4.6 Elemental standards of (n, γ) capture reaction. The amplitudes are artificially adjusted to show the details of each standard.

From Figure 4.7, the differences between the two calculated spectra are hard to see, as they both fit the measurement rather well. Numerical results indicate that the reduced χ^2 for the fitting with limited standards set is 24.3, and that with the interference set is 24.2. However, the elemental yield of Si when the interference set is used is -0.96%,

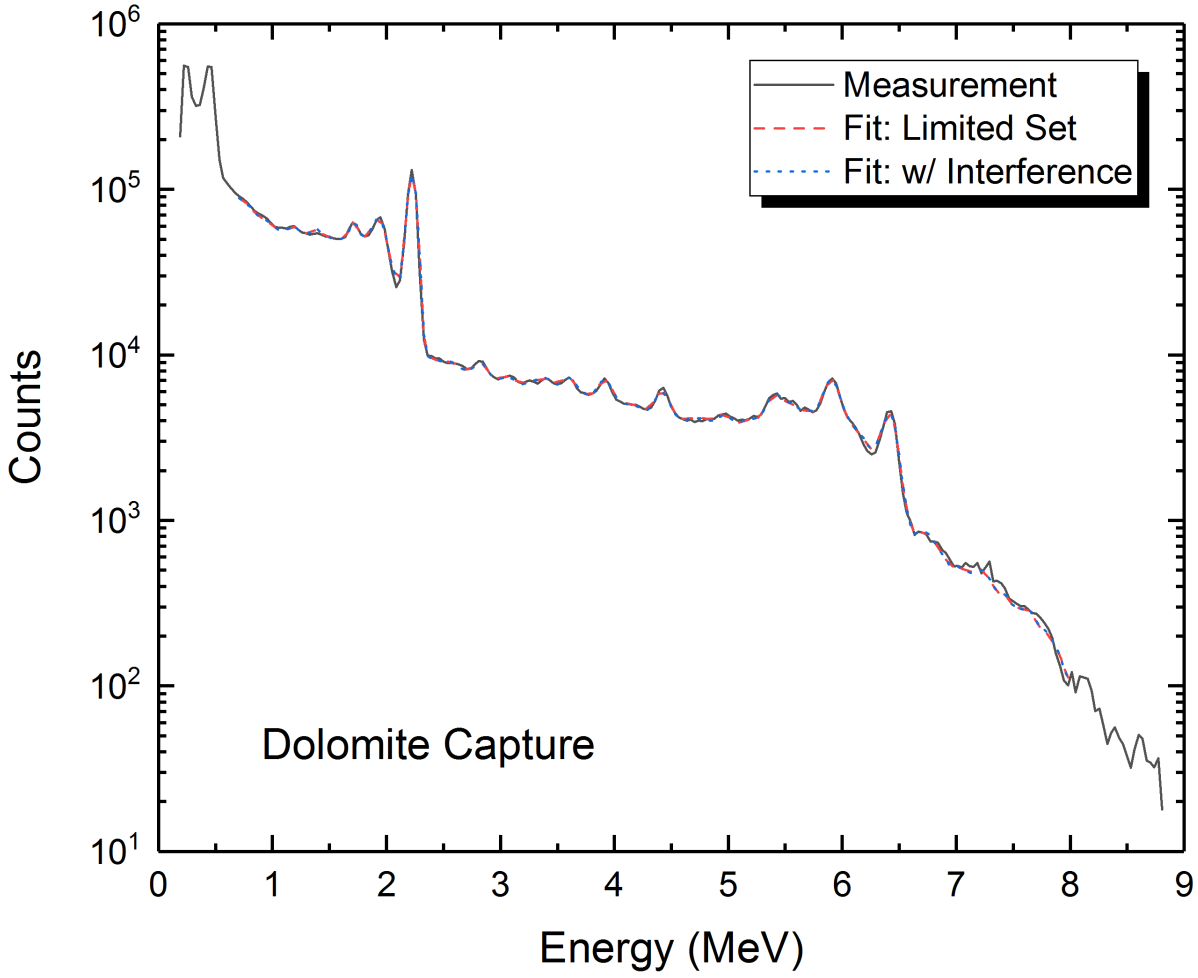

Figure 4.7 Comparison of measured dolomite capture spectrum and fit spectrum using two sets of standards. 'Limited Set' refers to the set with H, Ca, and Mg. 'w/ Interference' refers to the set with H, Ca, Mg, and Si, which is not present in the sample.

which is not realistic. Table 4.1 shows the numerical results of the fittings.

Table 4.1 Numerical results of the deconvolutions.

Element	Elemental Counts		Elemental Yields	
	Limited Set	w/ Interference	Limited Set	w/ Interference
Ca	1.27975×10^6	1.29603×10^6	35.92%	36.38%
Mg	2.43543×10^5	2.68418×10^5	6.84%	7.53%
H	2.03908×10^6	2.03218×10^6	57.24%	57.04%
Si	Not used	-3.42063×10^4	Not used	-0.96%

4.3.3 Non-negative least squares

Non-negative least squares (NNLS) method is another least squares fitting method for determining coefficients of linear models. Comparing to the LLS method, NNLS method restricts the coefficients to be non-negative, which makes this method much more practical for spectral deconvolution. A widely used algorithm is described by Lawson and Hanson in their book originally published in 1974[36]. In this research, this algorithm is implemented, but is slightly altered to make the computer code better organized, whereas the results calculated are identical to Lawson and Hanson's method. The following is a description of the algorithm used in this research. The meanings of $\boldsymbol{X}$, $\boldsymbol{Y}$, $\boldsymbol{\beta}$, m, and n are the same as those in Section 4.3.2.

1. Normalization: For each x_{ij} in matrix $\boldsymbol{X}$, let $x_{ij} = x_{ij}/\sqrt{y_i}$, and for each y_i in matrix $\boldsymbol{Y}$, let $y_i = y_i/\sqrt{y_i}$, where $i \in \{1, 2, 3, \ldots, m\}$, and $j \in \{1, 2, 3, \ldots, n\}$. This step accounts for the weight of each channel, and avoids the multiplication of weighting matrix $\boldsymbol{W}$ in the following computations.

2. Initialization: Define vectors $\boldsymbol{P} = \emptyset$, $\boldsymbol{R} = \{1, 2, 3, \ldots, n\}$. Let $\boldsymbol{\beta} = \{0, 0, 0, \ldots, 0\}$.

3. Outer loop:

   (a) Define vector $\boldsymbol{w}$ of dimension n, calculate its values by $\boldsymbol{w} = \boldsymbol{X}^T\boldsymbol{Y} - \boldsymbol{X}^T\boldsymbol{X}\boldsymbol{\beta}$.

(b) If vector $\boldsymbol{R}$ is empty, or if $w_i \leq 0$ for all $i \in \boldsymbol{R}$, then exit the Outer loop, and go to Step 4.

(c) Find an index $t \in \boldsymbol{R}$, such that $w_t = \max\{w_i; i \in \boldsymbol{R}\}$.

(d) Move t from $\boldsymbol{R}$ to $\boldsymbol{P}$.

(e) Inner loop:

i. Compose matrix $\boldsymbol{X'}$ from matrix $\boldsymbol{X}$ such that the i^{th} column of $\boldsymbol{X'}$ is the ${p_i}^{\text{th}}$ column of $\boldsymbol{X}$, $i \in \{1, 2, 3, \ldots, \text{size}(\boldsymbol{P})\}$.

ii. Solve the linear least squares problem $\boldsymbol{X's'} \approx \boldsymbol{Y}$ for vector $\boldsymbol{s'}$, using the LLS method described in Section 4.3.2. The weighting matrix should not be used here, as the weights have already been factored in.

iii. Compose vector $\boldsymbol{s}$ of dimension n from $\boldsymbol{s'}$, such that $s_{p_i} = s'_i$ for $i \in \{1, 2, 3, \ldots, \text{size}(\boldsymbol{P})\}$, and let other elements of $\boldsymbol{s}$ to be 0.

iv. If for all s'_i, there is $s'_i > 0$ (or equivalently, if $s_i > 0$ for all $i \in \boldsymbol{P}$), let $\boldsymbol{\beta} = \boldsymbol{s}$, then exit the Inner loop and go to Step 3.

v. Else, find an index $u \in \boldsymbol{P}$ such that $\beta_u/(\beta_u - s_u) = \min\{\beta_i/(\beta_i - s_i); s_i \leq 0, i \in \boldsymbol{P}\}$.

vi. Let scaler $\alpha = \beta_u/(\beta_u - s_u)$. Let $\boldsymbol{\beta} = \boldsymbol{\beta} + \alpha(\boldsymbol{s} - \boldsymbol{\beta})$.

vii. Move from $\boldsymbol{P}$ to $\boldsymbol{R}$ all indices $i \in \boldsymbol{P}$ for which $\beta_i = 0$ [1].

viii. Cycle Inner loop. Go to Step 3e.

4. The computation is completed. $\boldsymbol{\beta}$ holds the computation results.

The NNLS method is obviously more computational intensive than WLLS method, but on current computers, it still runs fast for typical cases. The difference in computation time between NNLS and WLLS is not significant.

Restricting the results to be non-negative makes the NNLS method a much more preferred method than WLLS for spectral deconvolution, because in realistic nuclear oil well logging application, the existence of a specific element in the rock formation is unknown. It is actually the deconvolution algorithm's duty to find out what elements are present. The $\boldsymbol{X}$ matrix of the computation, which stores the elemental standards,

[1] Special care should be given to this step when implementing this algorithm as a computer code. Due to finite precision arithmetic, β_i may exist in the computer memory as a very small number when it should be 0 arithmetically. Consider comparing β_i with a small number rather than 0.

usually holds all the predetermined standards. NNLS works very well in picking the right elements. Running the dolomite capture spectrum using H, Ca, Mg, and Si again with NNLS method gives the results shown in Table 4.2. It is demonstrated that this method correctly yields 0% Si, while resolves other elements correctly.

Table 4.2 Numerical results of the deconvolution of dolomite capture spectrum using different methods.

Element	Elemental Counts		Elemental Yields	
	WLLS	NNLS	WLLS	NNLS
Ca	1.27975×10^6	1.27975×10^6	35.92%	35.92%
Mg	2.43543×10^5	2.43543×10^5	6.84%	6.84%
H	2.03908×10^6	2.03908×10^6	57.24%	57.24%
Si	Not used	0	Not used	0%

4.3.4 Levenberg-Marquardt

Algorithm

The Levenberg-Marquardt (LM) method is a very commonly used method for fitting an arbitrary function by minimizing χ^2. The LM method is an iterative method that converges to the best answer, instead of calculating the best answer in one step like the LLS method. A very good description of the LM method in scaler form is available in Bevington's book published in 1992[37]. Gavin gives a good description of the method in matrix form[35]. Here a step by step algorithm is given, summarized from aforementioned sources.

Assuming $\hat{\boldsymbol{Y}}$ is calculated by an arbitrary function f, with independent variable $\boldsymbol{X}$ and generic parameter vector $\boldsymbol{\phi}$, that is

$$\hat{\boldsymbol{Y}} = f(\boldsymbol{X}; \boldsymbol{\phi}) \tag{4.15}$$

The Jacobian matrix of $\hat{\boldsymbol{Y}}$ with respect to $\boldsymbol{\phi}$ is

$$\boldsymbol{J} = \frac{\partial \hat{\boldsymbol{Y}}(\boldsymbol{X}; \boldsymbol{\phi})}{\partial \boldsymbol{\phi}} \tag{4.16}$$

And define a damping parameter λ, which is a scaler, then then LM algorithm is:

1. Initialization:
   (a) Specify the initial guess of $\boldsymbol{\phi}$.
   (b) Specify the initial value of $\lambda = \lambda_0$.
   (c) Calculate $\chi^2(\boldsymbol{\phi})$.
2. Solve
   $$(\boldsymbol{J}^T \boldsymbol{W} \boldsymbol{J} + \lambda \boldsymbol{I}) \Delta\boldsymbol{\phi} = \boldsymbol{J}^T \boldsymbol{W} (\boldsymbol{Y} - \hat{\boldsymbol{Y}}) \tag{4.17}$$
   for $\Delta\boldsymbol{\phi}$, where $\boldsymbol{I}$ is a unit matrix. Here $\Delta\boldsymbol{\phi}$ is an increment for $\boldsymbol{\phi}$, and is also a vector.
3. Calculate $\chi^2(\boldsymbol{\phi} + \Delta\boldsymbol{\phi})$.
4. If $\chi^2(\boldsymbol{\phi} + \Delta\boldsymbol{\phi}) > \chi^2(\boldsymbol{\phi})$, that means the tentative increment $\Delta\boldsymbol{\phi}$ makes the fit worse[2]. If $\lambda < \lambda_{max}$, increase λ by a factor of 10, and go to Step 2. Otherwise, the fitting is considered failed and should exit.
5. Else, if $\chi^2(\boldsymbol{\phi} + \Delta\boldsymbol{\phi}) < \chi^2(\boldsymbol{\phi})$, accept the increment by letting $\boldsymbol{\phi} = \boldsymbol{\phi} + \Delta\boldsymbol{\phi}$, $\chi^2(\boldsymbol{\phi}+\Delta\boldsymbol{\phi})$ also becomes $\chi^2(\boldsymbol{\phi})$. If $\lambda > \lambda_{min}$, decrease λ by a factor of 10, otherwise, let $\lambda = \lambda_{min}$.
6. If $\max |\Delta\boldsymbol{\phi}/\boldsymbol{\phi}| < \epsilon_1$, or $\max |\boldsymbol{J}^T \boldsymbol{W} (\boldsymbol{Y} - \hat{\boldsymbol{Y}})| < \epsilon_2$, the fitting is converged, exit.

In this algorithm, λ_0, λ_{max}, λ_{min}, ϵ_1, and ϵ_2 are all algorithm parameters, and can be tweaked to the needs. An example set is: $\lambda_0 = 0.01$, $\lambda_{max} = 10^7$, $\lambda_{min} = 10^{-7}$, $\epsilon_1 = 10^{-12}$, and $\epsilon_2 = 10^{-3}$.

[2]The acceptance criterion can also be a metric ρ, as specified by Nielsen[38].

Examples of application

As a demonstration, a series of $\boldsymbol{Y}$ data is created using

$$y = \exp(-x/\tau) \tag{4.18}$$

for $x = [-10, 10]$ and $\tau = 9.5$, as shown in Figure 4.8 by the red curve marked by 'True Value'. This is a typical nonlinear model because the value of y does not change linearly to x.

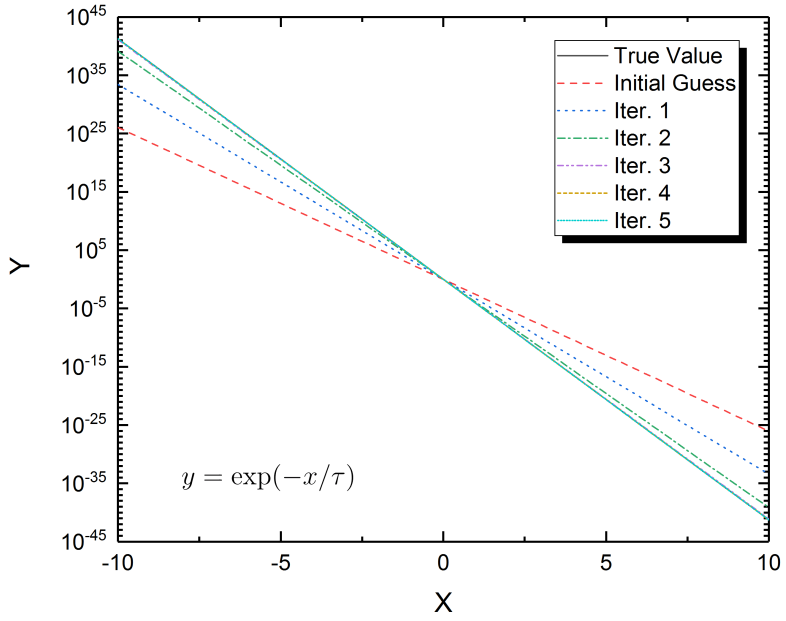

Figure 4.8 Iteration and convergence of τ calculated using LM method.

Next, assuming that the real value of τ is unknown. To use the LM method to fit the data and estimate the value of τ, make up an initial guess of $\tau = 6$, and run the fitting with model Equation 4.18. It is found that for this particular case, the fitting is converged in 5 steps, the fitted curve of each iteration is plotted in Figure 4.8, represented by the dotted curves. From the figure, it can be observed that, the initial $\boldsymbol{Y}$ calculated using the initial guess of $\tau = 6$ is significantly different from the true value. But with each iteration, the calculation approaches the true value progressively. From the 3$^{\text{rd}}$ iteration, the difference between the calculation and the true value is not quite distinguishable in

the figure. After the 5$^{\text{th}}$ iteration, the fitting exited successfully, with converged $\tau = 9.5$, which is the true value. Figure 4.9 shows the change of χ^2 in each step. It is clear that each iteration moves τ towards the direction that makes χ^2 smaller. Again, the last few iterations can hardly be distinguished in the figure, because the size of the step is generally reduced as the fitting parameter approaches optimum.

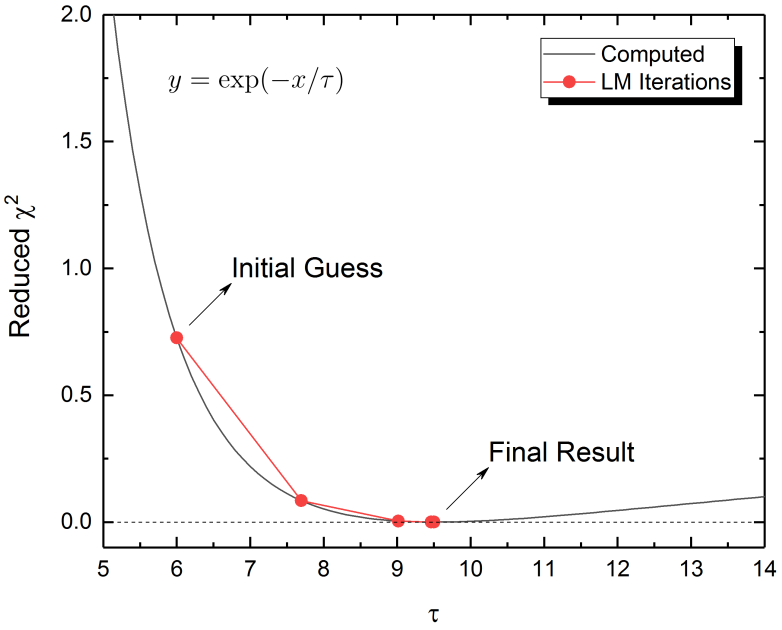

Figure 4.9 Change of χ^2 in each iteration of the fitting shown in Figure 4.8. The red curve is χ^2 computed using different τ values between 5 and 14.

The model formulated by Equation 4.18 is maybe one of the simplest models, because it has only one parameter. Figure 4.10 shows the iteration of a slightly more complex case, with two fitting parameters. This time, the model is a normal distribution with the amplitude equals 1, given by

$$y = \frac{1}{\sqrt{2\pi\sigma^2}} e^{-\frac{(x-\mu)^2}{2\sigma^2}} \tag{4.19}$$

The true parameters are centroid $\mu = 3.5$, and the width parameter $\sigma = 9.5$. To demonstrate the iteration of the two parameters, the initial guess is set to $\mu = 8$ and $\sigma = 6$. The fitting converged after 6 steps, and successfully found the correct parameters. Notice that as there are two fitting parameters in this model, the iteration figure has to be a

contour.

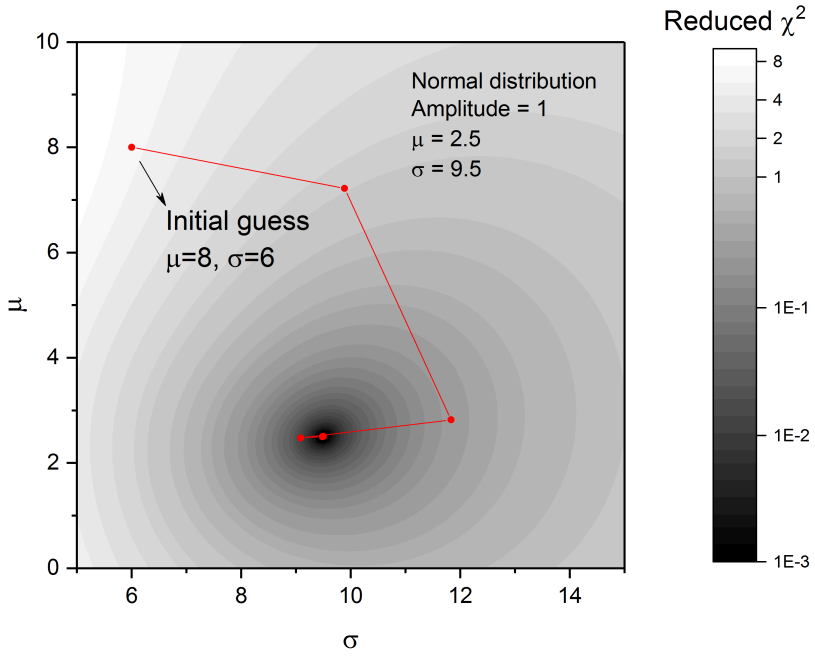

Figure 4.10 Iteration of fitting a normal distribution using the LM method.

Initial guess and local minimum

One disadvantage of the LM method is that, all the fitting parameters require initial guesses, and the final fitting results may be very sensitive the initial guesses. For some models, the χ^2 may include 'local minimums', where $\partial\chi^2/\partial\phi = 0$, but the value of χ^2 is not the smallest of the entire range in which the model is defined. The LM method only looks for the local best solution from the initial guesses of the fitting parameters specified by the user, but is not able to distinguish if the converged fitting result is the global optimum.

Take the sine wave as an example. Assume a sine wave is defined as

$$y = \sin(\omega x), \tag{4.20}$$

in $x = [-10, 10]$, and the real value of the parameter is $\omega = 1.1$. The black curve in

Figure 4.11 shows the change of χ^2 as a function of ω. A few 'pits' of χ^2 can be observed in the figure. Each pit represent a local minimum of χ^2. The true global smallest χ^2 appears at $\omega = 1.1$, which is the parameter used to generate the demonstration data.

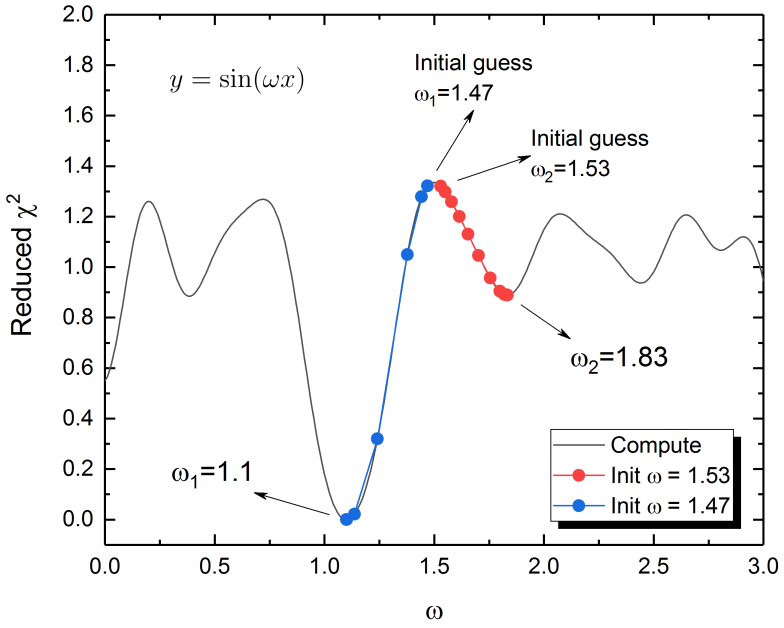

Figure 4.11 χ^2 as a function of ω for the model $y = \sin(1.1 \cdot x)$. Multiple local minimum χ^2 exists between -10 and 10. Whether the LM fitting can find the global optimum ω depends on the initial guess.

Also in Figure 4.11, the red curve shows the LM fitting iterations when the initial guess is $\omega = 1.53$, which is marginally larger than the peak at $\omega \approx 1.5$. As the LM method proceeds towards the direction that makes χ^2 smaller, the iteration progressively increases ω from 1.53, and eventually converges at $\omega = 1.83$, which is the value of the bottom of the pit of χ^2. Alternatively, the blue curve in the figure shows the same calculation, except that the initial guess is $\omega = 1.47$, which is on the left of the peak of χ^2. This time, as $\partial\chi^2/\partial\omega > 0$ at 1.47, the fitting moves ω towards the left, and eventually converges at the global optimum $\omega = 1.1$ after 7 iterations. This case shows that the selection of initial guess can be very important for the final results.

4.3.5 Modifications of LM for spectral deconvolution

Fitting model

In reality, the deconvolution model specified by Equation 4.2 does not always work well. Specific to the spectral deconvolution for the Tool, two factors needs to be considered:

1. The gain settings may shift. The device has a separate algorithm that monitors the gain settings, and attempts to adjust the settings periodically so that the capture hydrogen peak is always centered at channel 65, by definition. However, small mismatch between the alignment of the measurements and the elemental standards may still exist. As the resolution of $LaBr_3$ crystal is relatively higher, the misalignment problem does have greater impact on the deconvolution than other detectors with worse resolutions, such as BGO. It is desirable to have the standards adjusted for gain shifting by the fitting algorithm, in order to obtain a better fit. The alignment adjustment algorithm is described in Section 3.3.1.

2. The resolution may degrade. The device is subject to elevated temperature in the borehole. The heat may worsen the resolution, which again requires adjustments to the elemental standards in order to match the resolution of the measured spectra.

These two issues require additions to Equation 4.2, and make it a nonlinear problem:

$$\boldsymbol{Y} \approx \hat{\boldsymbol{Y}} = \sum_{i=1}^{n} \hat{\boldsymbol{X}}_i(\boldsymbol{X}_i; \boldsymbol{\alpha}_i)\beta_i \tag{4.21}$$

where $\boldsymbol{Y}$ is still the measurement, $\hat{\boldsymbol{Y}}$ is the calculated response, and is a vector of dimension m, $\hat{\boldsymbol{X}}_i$ is a vector of dimension m, and is the i^{th} elemental standard after adjustments for gain shifting and/or resolution matching, characterized by the adjustment parameter vector $\boldsymbol{\alpha}_i$ and the original elemental standard of the i^{th} element $\boldsymbol{X}_i$, and β_i is the elemental counts of the i^{th} element.

In Equation 4.21, the spectral adjustments to the standards can be either gain shifting adjustment, resolution matching adjustment, or both, depending on the need. For example, during the development phase, the measurements are always taken in an outdoor lab for no more than 1 hour, thus the resolution matching is not usually needed for these samples. The gain shifting adjustment includes two parameters, the multiplicative

factor M, and the additive factor A. The resolution matching adjustment includes one parameter σ only.

The inclusion of these adjustments makes the problem a nonlinear problem, and requires the LM method to solve. When using the LM method to calculate the elemental counts, the alignment adjustment parameters and the resolution matching parameter are automatically fitted, and they collectively constitute the model. When calculating $\hat{\boldsymbol{Y}}$ for each iteration inside the computer code, each elemental standard $\boldsymbol{X}_i$ is first adjusted for gain shifting and/or resolution matching to obtain $\hat{\boldsymbol{X}}_i$. Next, each adjusted standard $\hat{\boldsymbol{X}}_i$ is multiplied by an elemental count coefficient β_i, and summed up, to obtain $\hat{\boldsymbol{Y}}$.

Modification to the LM method

The core calculation of the LM method is solving Equation 4.17 for the increments of the parameters. In this equation, $\hat{\boldsymbol{Y}}$ and $\boldsymbol{J}$ both depend on the specific model. When implementing the LM method as a computer code, the Jacobian matrix $\boldsymbol{J}$ is calculated by finite difference method, usually central finite difference. Therefore, the partial derivative of $\hat{\boldsymbol{Y}}(\boldsymbol{X};\boldsymbol{\phi})$ with respect to the i^{th} parameter ϕ_i is

$$\begin{aligned}\boldsymbol{J}_i &= \frac{\partial \hat{\boldsymbol{Y}}(\boldsymbol{X};\boldsymbol{\phi})}{\partial \phi_i} \\ &\approx \frac{\hat{\boldsymbol{Y}}(\boldsymbol{X};\boldsymbol{\phi}+\Delta\boldsymbol{\phi}_i) - \hat{\boldsymbol{Y}}(\boldsymbol{X};\boldsymbol{\phi}-\Delta\boldsymbol{\phi}_i)}{2\|\Delta\boldsymbol{\phi}_i\|}\end{aligned} \tag{4.22}$$

where $\boldsymbol{J}_i$ is the j^{th} column of the Jacobian matrix, $\Delta\boldsymbol{\phi}_i$ is a vector with the same dimension as $\boldsymbol{\phi}$, and each element is equal to 0, except the i^{th} element which equals to a small scaler, and is a parameter of the iteration algorithm. Define two notations

$$\begin{aligned}\boldsymbol{\phi}_i^+ &= \boldsymbol{\phi} + \Delta\boldsymbol{\phi}_i \\ \boldsymbol{\phi}_i^- &= \boldsymbol{\phi} - \Delta\boldsymbol{\phi}_i\end{aligned} \tag{4.23}$$

Then Equation 4.22 can be written as

$$\boldsymbol{J}_i \approx \frac{\hat{\boldsymbol{Y}}(\boldsymbol{X};\boldsymbol{\phi}_i^+) - \hat{\boldsymbol{Y}}(\boldsymbol{X};\boldsymbol{\phi}_i^-)}{2\|\Delta\boldsymbol{\phi}_i\|} \tag{4.24}$$

To fit Equation 4.21 with the regular LM method, both in $\boldsymbol{\alpha}$ and $\boldsymbol{\beta}$ are treated as

nonlinear parameters, and the Jacobian matrix includes columns for each element of $\boldsymbol{\alpha}$ and $\boldsymbol{\beta}$. However, re-examining Equation 4.21 may reveal that, although as a whole, the formula is nonlinear, all β_i are in fact linear coefficients. This suggests that, if all the nonlinear parameters $\boldsymbol{\alpha}_i$ are known, then all the adjusted elemental standards $\hat{\boldsymbol{X}}_i(\boldsymbol{X}_i;\boldsymbol{\alpha}_i)$, $i \in \{1,2,\ldots,n\}$, are uniquely determined, and thus the vector of elemental counts $\boldsymbol{\beta}$ can be readily calculated using either WLLS or NNLS method, as illustrated in Section 4.3.2 and Section 4.3.3.

Having noticed this, this research modifies the regular LM method to work better for the spectral deconvolution problem. More specifically, a computer code was implemented that separately treats the nonlinear parameters $\boldsymbol{\alpha}$ and the linear parameters $\boldsymbol{\beta}$, and only uses the iterations to determine the values of $\boldsymbol{\alpha}$. In each iteration, the value of $\hat{\boldsymbol{Y}}$, which is needed in Equation 4.24 and Equation 4.17, is determined by first calculating each $\hat{\boldsymbol{X}}_i(\boldsymbol{X}_i;\boldsymbol{\alpha}_i)$ using the $\boldsymbol{\alpha}$ in current iteration, and then fitting them to Equation 4.21 using either WLLS method or NNLS method.

The detailed algorithm is mostly identical to the regular LM algorithm illustrated in Section 4.3.4, except the 2nd step is expanded, as the following:

2. Solve

$$(\boldsymbol{J}^T\boldsymbol{W}\boldsymbol{J} + \lambda\boldsymbol{I})\Delta\boldsymbol{\alpha} = \boldsymbol{J}^T\boldsymbol{W}(\boldsymbol{Y} - \hat{\boldsymbol{Y}}) \tag{4.25}$$

   for $\Delta\boldsymbol{\alpha}$.

   Assuming the spectra to be solved have m channels each, and the system has n nonlinear spectral adjustments parameters, and uses l elemental standards. Then, in Equation 4.25: $\boldsymbol{J}$ is the Jacobian matrix of size $m \times n$; $\boldsymbol{W}$ is the weighting matrix of $m \times m$, and is a diagonal matrix with the elements $w_i = 1/\sigma(y_i)^2$, $i \in \{1,2,\ldots,m\}$; $\boldsymbol{I}$ is a unit matrix of $n \times n$; $\Delta\boldsymbol{\alpha}$ is a vector of n; $\boldsymbol{Y}$ and $\hat{\boldsymbol{Y}}$ are both vectors of m.

   (a) To calculate $\hat{\boldsymbol{Y}}$, first calculate the adjusted elemental standard vectors $\hat{\boldsymbol{X}}_i = f(\boldsymbol{X}_i;\boldsymbol{\alpha}_i)$ for each elemental standard i, where $i \in \{1,2,\ldots,l\}$. Here f is the adjustment function(s), which could be gain shifting adjustment, resolution matching adjustment, or both; $\boldsymbol{X}_i$ is the original elemental standard vector of the i^{th} element; and $\boldsymbol{\alpha}_i$ is the adjustment parameters to be applied to the i^{th} standard. It is possible to apply different $\boldsymbol{\alpha}_i$ to different standards, or use the same set of adjustment parameters to every standard. Next, calculate $\hat{\boldsymbol{Y}}$

by performing a linear spectra fitting, using either WLLS or NNLS method, using the model

$$\hat{\boldsymbol{Y}} = \sum_{i=1}^{l} \beta_i \hat{\boldsymbol{X}}_i \tag{4.26}$$

(b) Calculate each column $\boldsymbol{J}_i$ of the Jacobian matrix, $i \in \{1, 2, \ldots, n\}$. $\boldsymbol{J}_i$ is calculated using Equation 4.24 and the method illustrated in Step 2a. Notice that the parameter vector $\boldsymbol{\phi}$ in Equation 4.24 should be replaced by $\boldsymbol{\alpha}$.

This algorithm is inspired by an earlier code developed by Gardner, called 'CURMOD'[39]. They differs in the way the Jacobian matrix $\boldsymbol{J}$ is computed. CURMOD keeps the linear coefficients $\boldsymbol{\beta}$ constant when calculating $\boldsymbol{J}$ using Equation 4.24 for Equation 4.25. This research treats $\boldsymbol{\beta}$ as a function of $\boldsymbol{X}$, $\boldsymbol{Y}$, and $\boldsymbol{\alpha}$, and recomputes $\boldsymbol{\beta}$ when calculating $\hat{\boldsymbol{Y}}(\boldsymbol{X}; \boldsymbol{\alpha}_i^+)$ and $\hat{\boldsymbol{Y}}(\boldsymbol{X}; \boldsymbol{\alpha}_i^-)$.

Example

An artificial case was created and tested in order to demonstrate the feasibility of the nonlinear spectral deconvolution model.

First, two 256 channels component spectra, which are equivalent to the elemental standards, are created. Each of these two spectra have 5 Gaussian peaks. Some of the peaks are intentionally placed close to each other or overlapped with another peak in the spectrum. The widths of these peaks are selected so that they roughly resemble the widths the peaks measured by a $LaBr_3$ detector. Each peak also has a different amplitude. The component spectra are shown in Figure 4.12.

Each of the two component spectra is then multiplied by a factor, and summed up to make a composite spectrum, which is equivalent to a gamma spectrum measured in an ideal environment and is well aligned. Next, this composite spectrum is Gaussian broadened with $\sigma = 3$, contracted by 5%, and shifted to the right by 5 channels (gain shifting parameter $M = 0.95$, and $A = 5$). This emulates an extreme scenario where the measurement is highly distorted. The distorted spectrum is then randomized according to Poisson distribution to make it more realistic. Figure 4.13 shows the comparison of the original composite spectrum, and the distorted and Poisson randomized composite spectrum.

Finally, the two component spectra, are used to fit the distorted and randomized

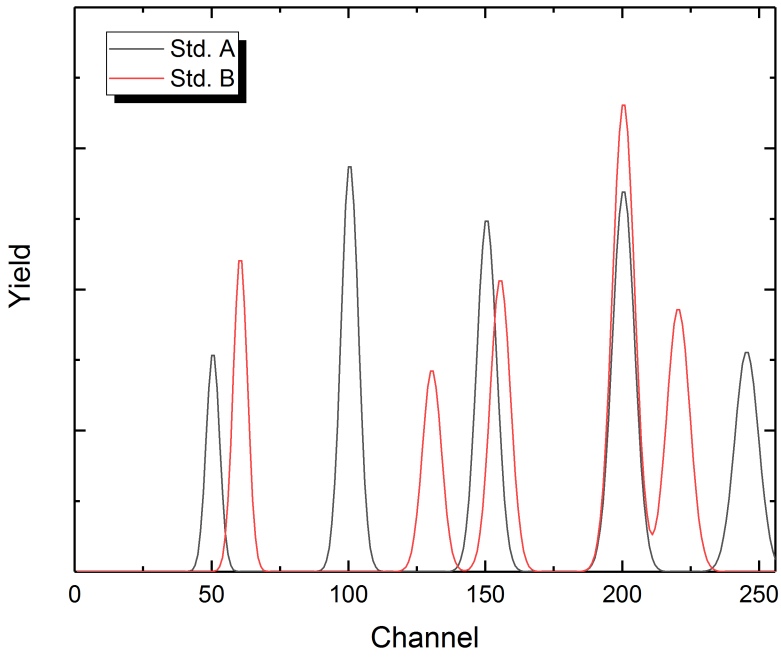

Figure 4.12 Two artificially generated component spectra.

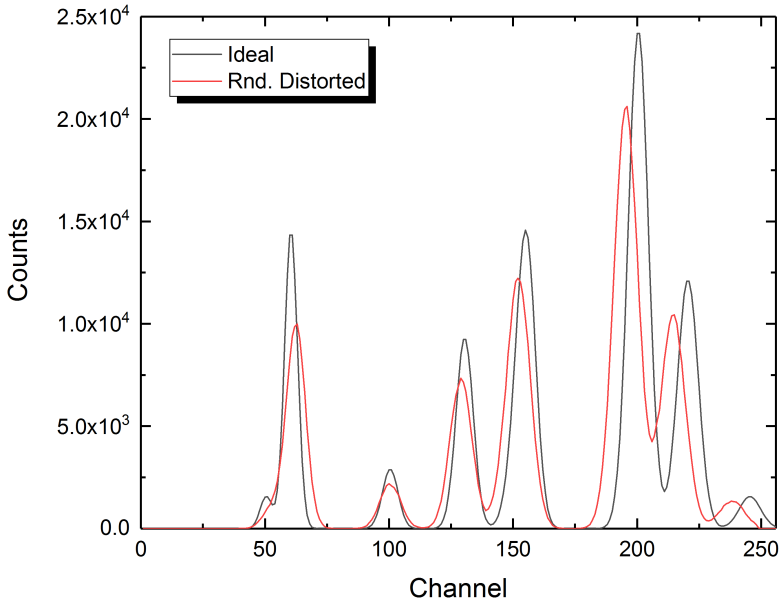

Figure 4.13 Comparison of the ideal composite spectrum, and the distorted and Poisson randomized composite spectrum. The ideal composite spectrum is Gaussian broadened by $\sigma = 3$, contracted by 5%, and shifted to the right by 5 channels to create the distorted spectrum.

composite spectrum. Both gain shifting adjustment and resolution matching adjustment are enabled, and both component spectra share the same set of adjustment parameters. Figure 4.14 shows the comparison of the composite spectrum and the fitted spectrum. The fitting successfully converged. The absolute differences of the fitted adjustment parameters are: $\Delta\sigma = 3.2 \times 10^{-3}$, $\Delta A = 2.5 \times 10^{-3}$, $\Delta M = 5.8 \times 10^{-5}$. The overall reduced $\chi^2 = 0.70$, which indicates a very good fitting.

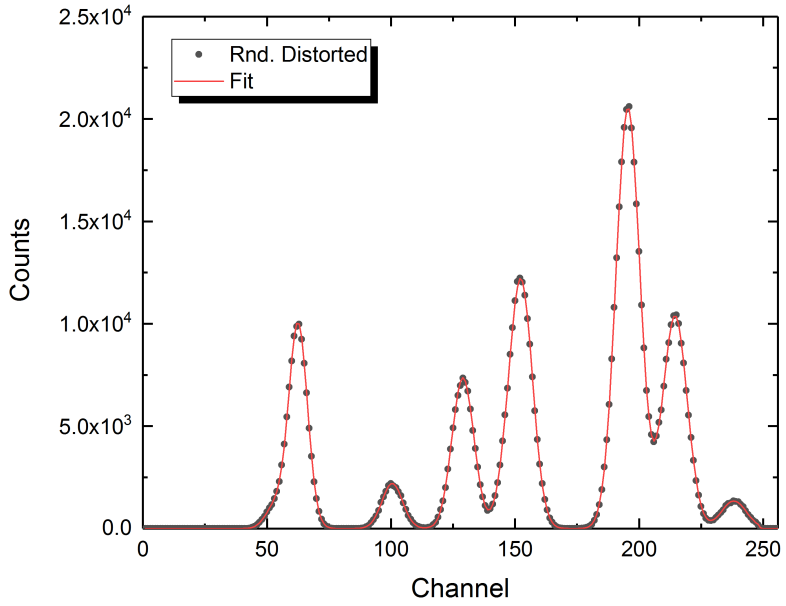

Figure 4.14 Comparison of the distorted and randomized composite spectrum and the fitted spectrum. The reduced χ^2 of the deconvolution is 0.7, which suggests a good fit.

Advantages

The introduction of the modification to the LM method brings two improvements:

1. All parameters fitted with the regular LM method require initial guesses. As shown in Section 4.3.4, bad initial guesses may lead to underoptimized parameters. The modified LM method treats linear and nonlinear separately in one algorithm, and does not require initial guesses for the linear parameters.

2. This modification significantly reduces the number of parameters to be iterated.

For complex models, such as adjusting elemental standards for gain shifting and resolution, the calculation of $\hat{\boldsymbol{Y}}$ in each iteration consumes a considerable amount of time. As the modification treats $\boldsymbol{\beta}$ separately, this dramatically reduces the CPU time on calculating the Jacobian matrices. In addition, reducing the number of nonlinearly searched parameters also reduces the number of iterations to meet the convergence criterion.

To test the performance of the modification, the dolomite (n, γ) measurement is used. The spectrum is deconvolved with 11 capture standards[3] using both the regular LM method, and the modified method. The deconvolution is repeated for 200 times each in order to emulate processing a large amount of measurements. On a typical laptop computer equipped with an Intel® Core™ i7-3720QM 2.60GHz CPU, the fitting using the regular LM method took 42 seconds, and that using the modified LM method took 8 seconds. The fitted spectrum provided by both methods are practically identical, as shown in Figure 4.15.

4.4 Elemental concentrations

4.4.1 Sensitivity factor

Definition and measurement

By conducting spectral deconvolutions, the direct results are elemental counts for (n, γ) capture spectrum and (n, n'γ) inelastic scattering spectrum. The results only represents the absolute contributions to the spectra by each element, in terms of gamma counts measured by the detector. These results need to be further converted to elemental weight concentrations to generate more meaningful results for well log analysts.

For one spectrum (either capture or inelastic), define C_i to be the absolute gamma counts contributed by the i^{th} element in the sample, C to be the total counts of the spectrum, y_i to be the yield of the i^{th} element, defined by

$$y_i = \frac{C_i}{C} \tag{4.27}$$

[3]Ca, Cl, Fe, Gd, H, K, Mg, Na, S, Si, Ti

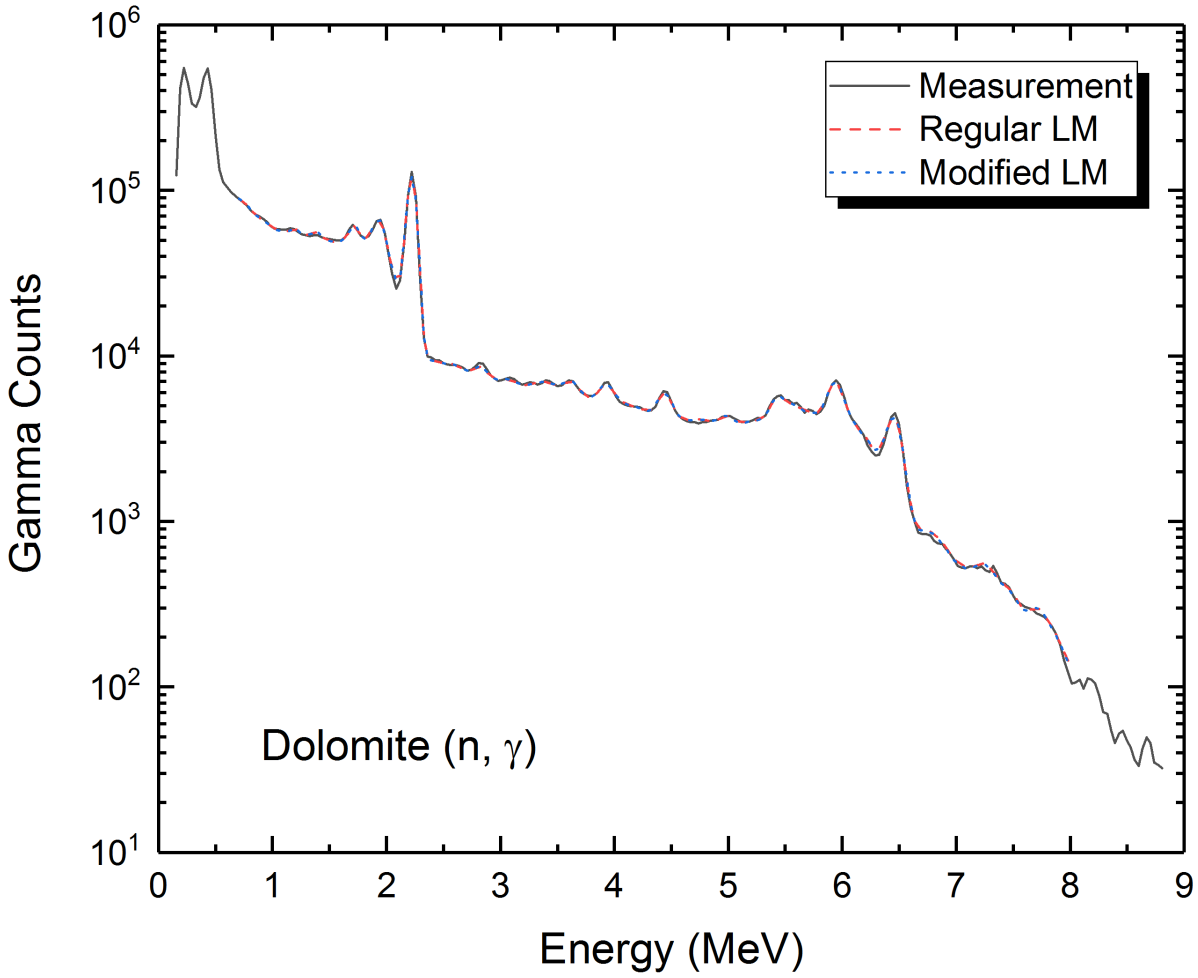

Figure 4.15 Comparison of the spectral deconvolution performed using the regular LM method and the modified LM method. The reduced χ^2 for both cases is ~ 15.1, with a difference of smaller than 10^{-3}.

In theory, y_i can be calculated by[40]:

$$y_i = \frac{C_i}{C} = N_A \frac{W_i \rho}{A_i} \frac{\bar{\Phi} \bar{\sigma}_i \bar{\Omega} M_i}{C} I \bar{V} \tag{4.28}$$

where N_A is the Avogadro's number, W_i is the weight concentration of the i^{th} element in the sample, ρ is the weight density of the sample, A_i is the atomic weight of the i^{th} element in the sample, $\bar{\Phi}$ is the average neutron flux in the effective volume of investigation, $\bar{\sigma}_i$ is the average gamma generating neutron interaction microscopic cross section of the i^{th} element, $\bar{\Omega}$ is the effective solid angle subtended by the detector, M_i is a factor that accounts for the average number of gamma emission per reaction, gamma transmission efficiency, and detection efficiency, C is the total number of gamma counts, I is the neutron source intensity, and $\bar{V}$ is the effective volume of investigation.

Notice that for a given sample, some of the variables in Equation 4.28 are properties of the element, and others are either the properties of the sample as a whole, or properties of the measurement device. Define the sensitivity factor S of the i^{th} element of the sample as

$$S_i = \frac{\bar{\sigma}_i M_i}{A_i} \tag{4.29}$$

and normalization factor

$$\frac{1}{F} = N_A I \bar{V} \frac{\rho \bar{\Phi} \bar{\Omega}}{C} \tag{4.30}$$

Then the elemental yield of the i^{th} element is

$$y_i = \frac{C_i}{C} = \frac{1}{F} W_i S_i \tag{4.31}$$

and consequently

$$W_i = F \frac{y_i}{S_i} \tag{4.32}$$

The sensitivity factor includes variables that are specific to the element, and the normalization factors include both constants and variables that are specific to the sample being measured. The factor M_i in the sensitivity factor does depend on the environment and the detector properties. However, for oil well logging applications, the types of rock formation that are regularly found are limited, and the physical properties that affect M_i, such as density, do not vary significantly from one formation to another[2]. In addition, for a specific tool, the detection efficiency is also determined, and therefore M_i can be

determined.

Ideally, if the information of the sample is completely known, then each variable in Equation 4.28 can be estimated, and the elemental yields of each element can be calculated. However, aside from being highly impractical to do so, the real problem that needs to be solved is quite the contrary: the properties of the sample, especially the weight concentrations of the mineral elements, are the variables that need to be determined.

Still, Equation 4.28 and Equation 4.31 provide a good starting point. Instead of pursuing the absolute elemental sensitivity factors and sample normalization factors, the relative factors are used. From Equation 4.32, it can be deduced that, for a given sample, the weight concentration ratio of two elements i and j is

$$\begin{aligned} \frac{W_i}{W_j} &= \frac{F\frac{y_i}{S_i}}{F\frac{y_j}{S_j}} \\ &= \frac{y_i}{S_i}\frac{S_j}{y_j} \\ &= \frac{y_i}{y_j}\frac{S_j}{S_i} \end{aligned} \tag{4.33}$$

By calculating the ratios, the normalization factor F is eliminated, and the relative weight can be calculated. The relative weights are to be used in combination with the oxide closure model, introduced in Section 4.4.2 to estimate absolute elemental concentrations.

The sensitivity factors are very important tool specific parameters that plays a critical role in converting the spectral deconvolution results to weight concentrations[2]. As the name implies, sensitivity factor reflects how 'sensitive' a tool is to an element. Higher sensitivity factors means that the element makes greater contribution to the overall gamma spectrum per unit weight in the sample. Notice that as the sensitivity factor accounts for the neutron interaction cross section, for each element, the sensitivity factor for capture and inelastic reactions are different.

The sensitivity factors are measured in the lab environment as part of the tool characterization process in the development phase. Instead of an absolute value, the sensitivity factor of an element S_i is measured relative to the sensitivity of a reference element S_R. The sensitivity of the reference element is always set to unity. To make the measurement, a sample with the reference element and an element of interest is prepared. The weight concentrations of both elements in the sample are measured accurately using other lab

measurement techniques, such as XRF. Then a measurement using the Tool is taken, and the spectrum is deconvolved for elemental yields. According to Equation 4.33, there is

$$\frac{W_R}{W_i} = \frac{y_R}{y_i}\frac{S_i}{S_R} \tag{4.34}$$

In this equation, the weight concentrations of the two elements are measured in the lab; the elemental yields are solved by the spectral deconvolution; the sensitivity factor of the reference element S_R is set to unity, thus the relative sensitivity factor of the element of interest S_i can be uniquely determined by

$$S_i = \frac{W_R}{W_i}\frac{y_i}{y_R} \tag{4.35}$$

In practice, silicon is often used as the reference element, because it is one of the most abundant elements in the earth formations, and has good sensitivities in both the capture and inelastic spectra. The sensitivity factors of hydrogen and oxygen are not of interest, as they are present in the borehole, formations, and formation pores. Characterizing hydrogen and oxygen is almost impossible. The other mineral elements of the formation matrix are of primary interest. Also notice that the spectral deconvolutions are performed on a portion of the spectrum, such as 1 MeV to 9 MeV. The sensitivity factors may change if a different deconvolution range is used, because the ratio of the elemental yield may change.

Figure 4.16 shows the capture sensitivity factors of the Tool over a typical fitting range. Figure 4.17 shows the inelastic sensitivity factors.

Example

This example shows how the calcium capture sensitivity factor S_{Ca} is measured.

First, the sample is prepared. The sample used for measuring the Ca capture sensitivity factor is a mixture of 486.8 lbs of quartz (SiO_2), 489.6 lbs of calcite ($CaCO_3$), and 395.8 lbs of water for moderation. After the sample is fully mixed, a small portion of the sample mixture is sent to the lab for characterization. The characterization measures the elemental weight concentration as shown in Table 4.3. In the sample, about 1.5% by weight are impurities, including U, Th, Al, Fe, Gd, K, Mg, Na, S. These amounts are insignificant, and have little influence on the sensitivity factor measurement. The oxygen concentration is not shown.

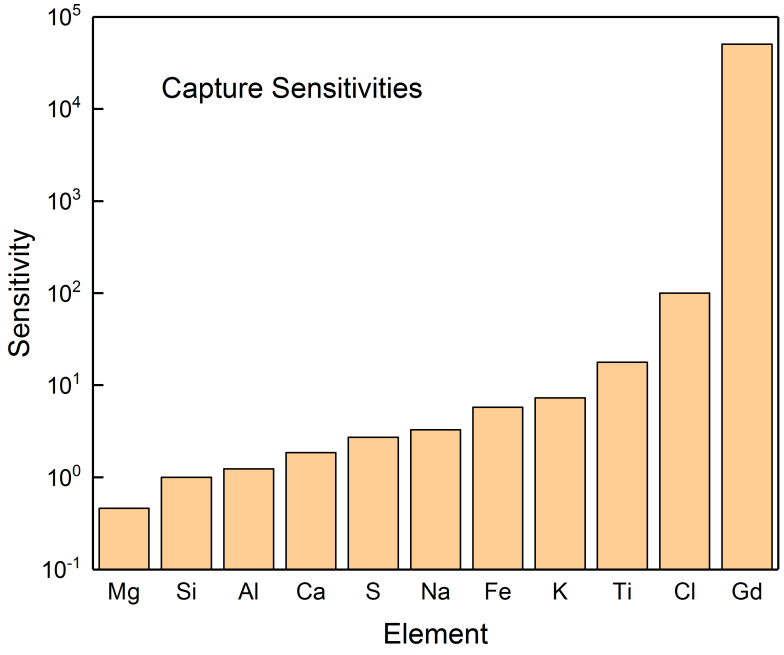

Figure 4.16 Capture sensitivity factors of the Tool.

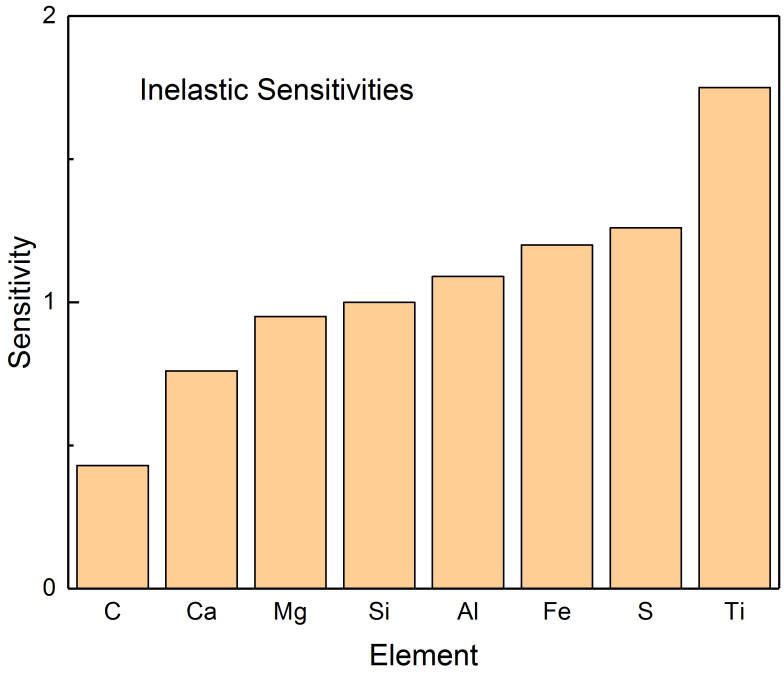

Figure 4.17 Inelastic sensitivity factors of the Tool.

Table 4.3 XRF measurement of quartz+calcite sample

Element	Weight concentration
C	5.8%
Ca	19.2%
Si	22.7%
Impurities	1.5%

The sample is placed inside a barrel made of aluminum, and the entire barrel is then placed in a tank filled with water for additional neutron moderation. Figure 4.18 shows the aluminum barrels used for characterization. Each barrel holds a different sample. Figure 4.19 shows the water tank in which the barrel and the logging tool are to be placed. The tank is constructed below the surface for maximum radiation protection. The hole at the center extends deeper to accommodate the logging tool, so that the neutron generator and the gamma detector can be placed at the vertical center of the sample. Figure 4.20 shows how the measurement is taken, when the barrel and the logging tool are both in place. Notice that more water is used to fill the tank for additional moderation.

Figure 4.18 Barrels used for calibration and characterizations.

Next, a capture measurement is taken and is deconvolved. At the time of deconvolu-

Figure 4.19 Empty water tank. The hole in the middle extends deeper, so that the neutron generator and gamma detector portion of the logging tool can be positioned at the center of the sample barrel.

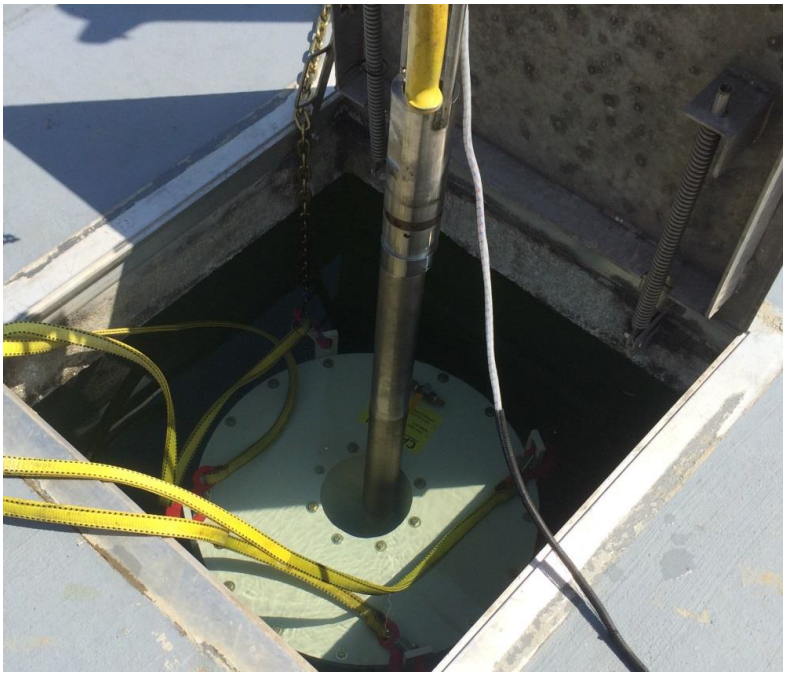

Figure 4.20 Logging tool and characterization barrel properly placed inside the tank.

tion, the elemental standards should have already been determined. As the composition of the sample is already known, only capture standards for Si, Ca, H, and Al are used for the deconvolution. O and C do not have capture standards, as their capture cross sections are extremely small thus inconsequential. The measured capture spectrum and the fit are shown in Figure 4.21. Table 4.4 shows the deconvolution results, in terms of elemental yields.

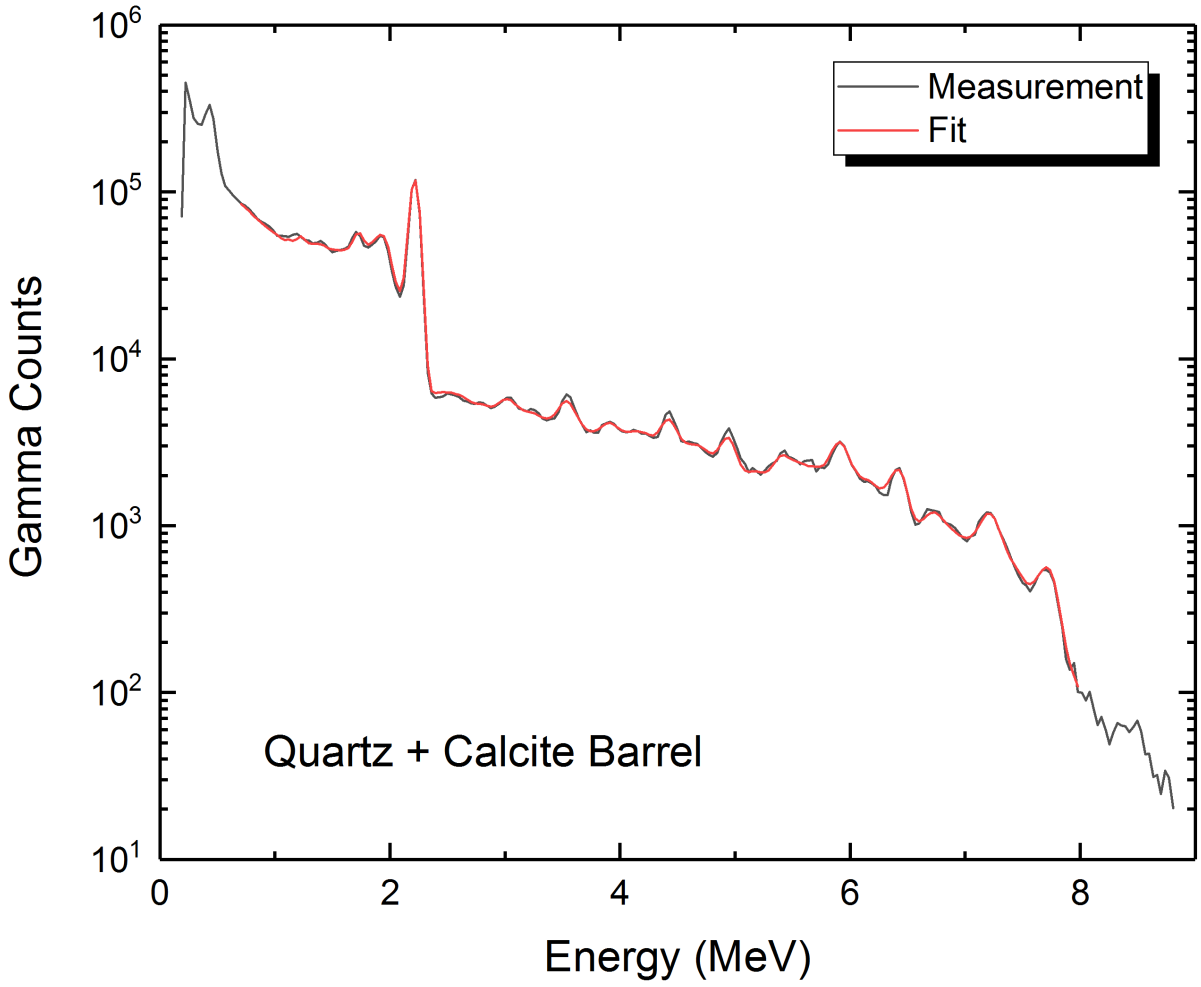

Figure 4.21 Measurement and fit of the quartz + calcite sample.

Finally, using Equation 4.35, Table 4.3, and Table 4.4, the capture sensitivity factor

Table 4.4 Deconvolution results of the quartz + calcite sample.

Element	Yield
H	69.96%
Si	8.87%
Ca	13.08%
Al	8.08%

of Ca relative to that of Si can be calculated:

$$\begin{aligned} S_{Ca} &= \frac{W_{Si}}{W_{Ca}} \frac{y_{Ca}}{y_{Si}} \\ &= \frac{22.7\%}{19.2\%} \frac{13.08\%}{8.87\%} \\ &= 1.74 \end{aligned} \tag{4.36}$$

4.4.2 Oxide closure model

Section 4.4.1 provides a method of calculating relative elemental weight concentrations. It is of practical interest to understand the mineral composition of the rock matrix (the portion excluding the pores), which requires knowledge of the elemental composition in absolute weight concentrations. The oxide closure model provides a method of estimating the absolute weight concentrations of the elements in the matrix, also known as dry weights.

For a matrix, if the relative weight of each element can be determined, then according to Equation 4.32, there is obviously

$$1 = \sum_{i=1}^{n} W_i = F \sum_{i=1}^{n} \frac{y_i}{S_i} \tag{4.37}$$

where n is the number of all the elements in the matrix. However, this is impractical, because oxygen exist in the matrix, the pores, and the borehole, and separating them is virtually impossible. Therefore the dry weight of oxygen cannot be directly measured in real time with the logging device.

The oxide closure model solves this by making an important simplification[2], which assumes that each of the measured mineral elements exists in the form of an oxide, and

the sum of these oxide minerals is unity. Equation 4.37 can therefore be rewritten as

$$1 = \sum_{i=1}^{m} X_i W_i = F \sum_{i=1}^{m} X_i \frac{y_i}{S_i} \tag{4.38}$$

where m is the number of measurable mineral elements in the matrix, and X_i is the oxidation factor of the i^{th} mineral element, which is the ratio of the weight of the oxide to the weight of the mineral element. In this equation, X_i, y_i, and S_i are know parameters, thus the value of F can be determined. Once the value of F is determined, the estimated absolute dry weight of any mineral element i can be calculated using Equation 4.32.

In some cases, the element may be part of a non-oxide mineral. For example, in the earth, Fe can exist as either Fe_2O_3 (iron oxide) or FeS_2 (pyrite). However, according to a study by Hertzog[2], where numerous core samples were analyzed, it was found that this model works fairly well in most cases, with only a small dispersion. Table 4.5 gives a list of minerals commonly associated with hydrocarbon-bearing formations. Table 4.6 gives a list of common oxides and their corresponding oxidation factors. Chapter 5 gives a complete example of calculating, including the application of oxide closure model.

Table 4.5 Mineral commonly associated with hydrocarbon-bearing formations

Category	Mineral	Compositional Elements	Chemical Formula
Silicates	Quartz	O, Si	SiO_2
	Mica	Al, F, K, Mg, O, Si	$K[Mg, Fe]_3(AlSi_3O_{10})[F, OH]_2$
	K-Felspar / Orthoclase	Al, K, O, Si	$KAlSi_3O_8$
	Na-Felspar / Plagioclase	Al, Na, O, Si	$NaAlSi_3O_8$
	Zeolite	Al, Ca, H, Na, O, Si	$Na_2Al_2Si_3O_{10}(2\,H_2O)$
Clay Groups	Illite	Al, H, K, O, Si	$K_{0.7}[Al, Mg, Fe]_2(Al_{0.67}Si_{3.33})O_{10}(OH)_2$
	Smectite	Al, H, Na, O, Si	$Na_{0.4}[Al, Mg, Fe]_2(Al, Si)_4O_{10}(OH)_2$
	Kaolinite	Al, H, O, Si	$Al_2Si_2O_5(OH)_4$
	Chlorite	Al, Fe, H, Mg, O, Si	$(Mg_{1.6}Fe_{3.2}Al_{1.2})(AlSi_3)O_{10}(OH)_8$
	Glauconite	Al, Fe, H, K, Mg, O, Si	$K_{0.8}[Fe_{1.2}Al_{0.4}Mg_{0.4}](Al_{0.35}Si_{3.65})O_{10}(OH)_2$
Carbonate	Calcite	C, Ca, O	$CaCO_3$
	Dolomite	C, Ca, Mg, O	$CaMg(CO_3)_2$
	Siderite	C, Fe, O	$FeCO_3$
Evaporites	Anhydrite	Ca, O, S	$CaSO_4$
	Halite	Cl, Na	$NaCl$
	Sylvite	Cl, K	KCl
Iron-Based	Pyrite	Fe, S	FeS_2
	Hematite	Fe, O	Fe_2O_3
Carbon-Based	Kerogen	C, H, O, N, S	$C_{215}H_{330}O_{12}N_5S$
	Anthracite Coal	C, H, O	$C_{93}H_3O_4$
	Bituminous Coal	C, H, O	$C_{82}H_5O_{13}$
Other	Apatite	Ca, F, O, P	$Ca_5(PO_4)_3[F, Cl, OH, Br]$

Table 4.6 Oxidation factors of elements commonly found in earth formations

Element	Oxide	Oxidation Factor
Al	Al_2O_3	1.8895
Ca	CaO	1.3992
	$CaCO_3$	2.4973
	$CaSO_4$	3.3669
C	C	1
	CO_2	3.6642
	$CaCO_3$	8.3331
	$MgCO_3$	7.0199
Gd	Gd	1
Fe	Fe_2O_3	1.4297
	FeS	1.5742
	$FeCO_3$	2.0746
	FeO	1.2865
Mg	MgO	1.6583
	$MgCO_3$	3.469
O	O	1
K	K_2O	1.2046
Si	SiO_2	2.1393
Na	Na_2O	1.3479
S	$CaSO_4$	4.2458
	S	1
	SO_3	2.4969
	FeS	2.7416
Ti	TiO_2	1.6685

Chapter 5

Complete Example

In this chapter, a full calculation example is given.

5.1 Sample measurements

In this example, measurements of a large cubic dolomite block are taken. The sample is about 5 feet long on each side, and is shown in Figure 5.1. The chemical composition of dolomite is $CaMg(CO_3)_2$. Smaller samples from the block were taken and analyzed in the lab. Table 5.1 shows the XRF analysis results of the rock. The oxygen concentration is not listed.

Table 5.1 XRF analyzed elemental concentrations of the dolomite block.

Element	Weight
Al	0.12%
C	12.7%
Ca	21.7%
Fe	0.1%
Gd	0.2 ppm
K	0.09%
Mg	12.5%
Na	0.01%
S	0.01%
Si	0.47%
Ti	0.01%

Figure 5.1 Dolomite rock sample.

To make the measurement, a hole was drilled at the center of the sample. The sample was placed in a tank, as shown in Figure 4.19, and the tank was then filled with water. The sample was measured for 20 minutes.

5.2 Spectral preprocessing

The raw measurements are shown in Figure 5.2. The measured spectra were manually aligned to the design specifications. A number of peaks have been identified and their centroids measured using the differentiation method described in Section 3.3.1. These measured peak centroids were then linearly fitted to their standard locations, and the fitted parameters were used as the parameters to realign the spectra. Table 5.2 lists all the characteristic peaks used for aligning the spectra. In the table, the column 'Peak Type' shows whether a peak is a primary peak, such as a full energy peak, or a secondary peak, such as a single escape peak. For these three spectra measured, the alignment parameters were $M = 0.957333$ and $A = 1.532867$, meaning the spectra are contracted by less than

5%, and shifted to the right by 1.53 channels. Figure 5.3 shows the aligned spectra.

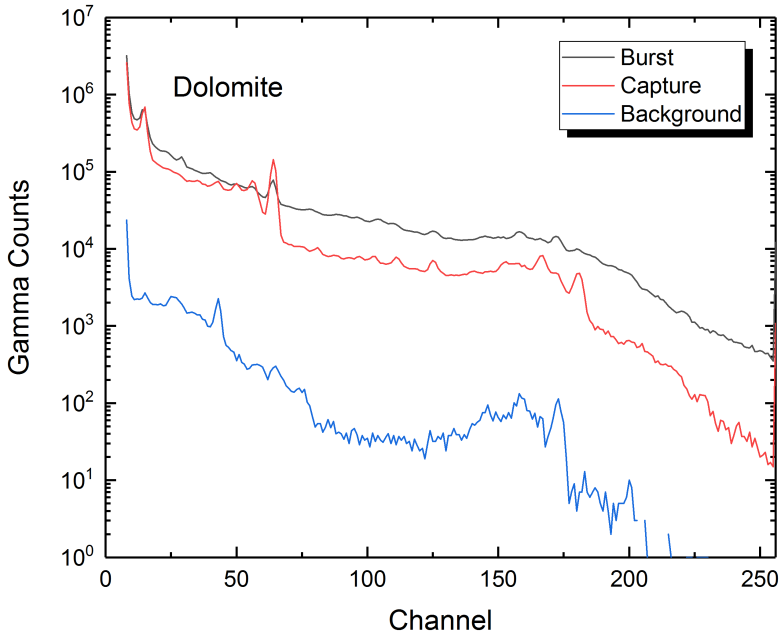

Figure 5.2 Raw measurements of the dolomite sample in water borehole.

After the spectra were aligned, the background spectrum was subtracted from the capture measurement and the burst measurement. The subtraction factors are 9.75 and 3 respectively, calculated based on the neutron generator firing scheme. Finally, the capture spectrum was subtracted from the burst spectrum to make the inelastic spectrum. The subtraction factor was determined empirically. Figure 5.4 shows the net burst, capture, and inelastic spectra. The capture and inelastic spectra were used in the final deconvolution process.

5.3 Spectral deconvolution

The deconvolution starts with the capture spectrum. It is assumed that no prior knowledge of the sample is available. The capture standards used to deconvolve the spectrum included Ca, Fe, Gd, H, K, Mg, Na, S, Si, and Ti. The deconvolution used gain shifting adjustments, but had resolution matching adjustments disabled. The fitting was per-

Table 5.2 Gain setting calibration parameters.

Energy (MeV)	Element	Gamma Spectrum	Peak Type	Std. Chn.	Measured Chn.	Aligned to
0.847	Fe	Bkgd.	secondary	24.58	24.95	25.06
1.369	Mg	Burst	primary	39.72	39.56	39.56
1.473	La	Bkgd.	secondary	42.74	42.11	42.45
1.943	Ca	Capture	primary	56.38	55.59	55.50
2.223	H	Capture	primary	64.50	63.42	63.28
2.223	H	Burst	primary	64.50	63.42	63.28
4.419	Ca	Capture	primary	128.22	124.49	124.28
4.438	C	Burst	primary	128.77	124.98	124.81
5.909	Ca	Capture	secondary	171.45	166.00	165.67
6.130	O	Burst	primary	177.86	171.52	171.81
6.130	O	Bkgd.	primary	177.86	171.54	171.81
6.420	Ca	Capture	primary	186.28	179.79	179.86

Gain shifting parameters:
Multiplicative factor $M = 0.957333$
Additive factor $A = 1.532867$

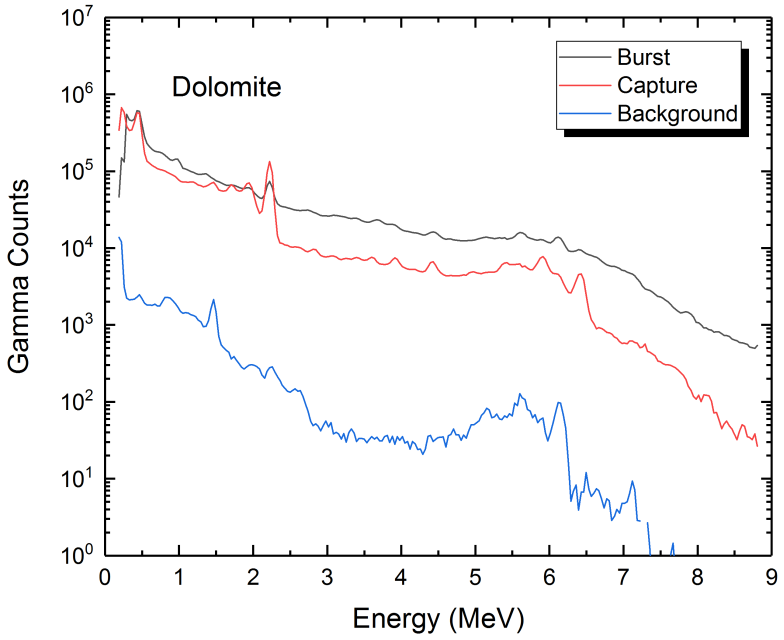

Figure 5.3 Raw measurements aligned to specification using parameters calculated in Table 5.2.

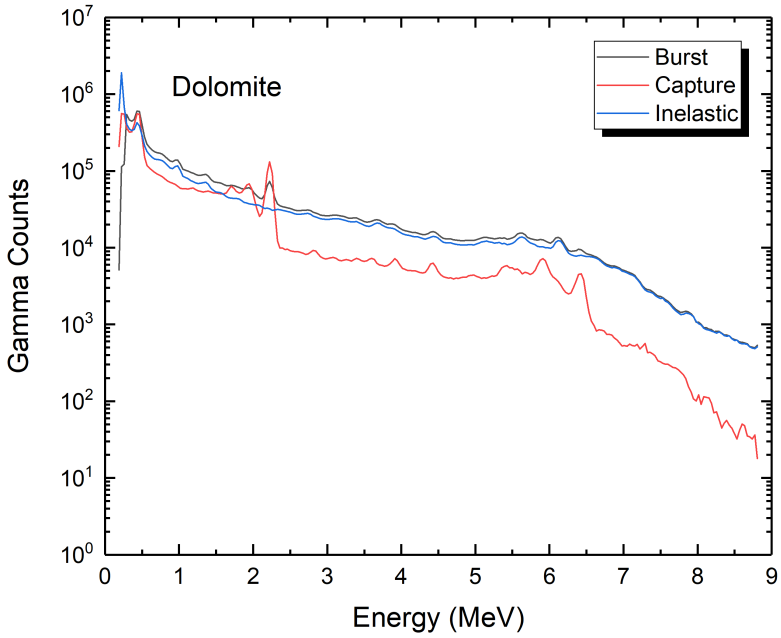

Figure 5.4 The net burst, capture, and inelastic spectra after background subtraction.

formed for the spectrum from 0.75 MeV to 8MeV. Figure 5.5 shows the fit. The reduced χ^2 of the fitting was 18.3, which is typical for capture spectra. The fitted gain shifting parameters are virtually $M = 1$ and $A = 0$, which indicate no shifting is necessary. The calculated elemental yields are shown in Table 5.3.

Next, the inelastic spectrum was deconvolved. Figure 5.6 shows the fit. The reduced $\chi^2 = 13.3$, which is typical for inelastic spectral deconvolutions. The fitted gain shifting adjustments are also virtually none, due to the manual alignments at the first place. The calculated elemental yields are listed in Table 5.4.

5.4 Weight calculation

By calculating Equation 4.38, using the elemental yields listed in Table 5.3, the capture sensitivity factors shown in Figure 4.16, and the oxidation factors listed in Table 4.6, the normalization factor for the capture spectrum is calculated to be $F = 1.07$. The elemental dry weights based on the capture spectrum, calculated using Equation 4.32, is listed in Table 5.5.

Similarly, by calculating Equation 4.38, using the elemental yields listed in Table 5.4,

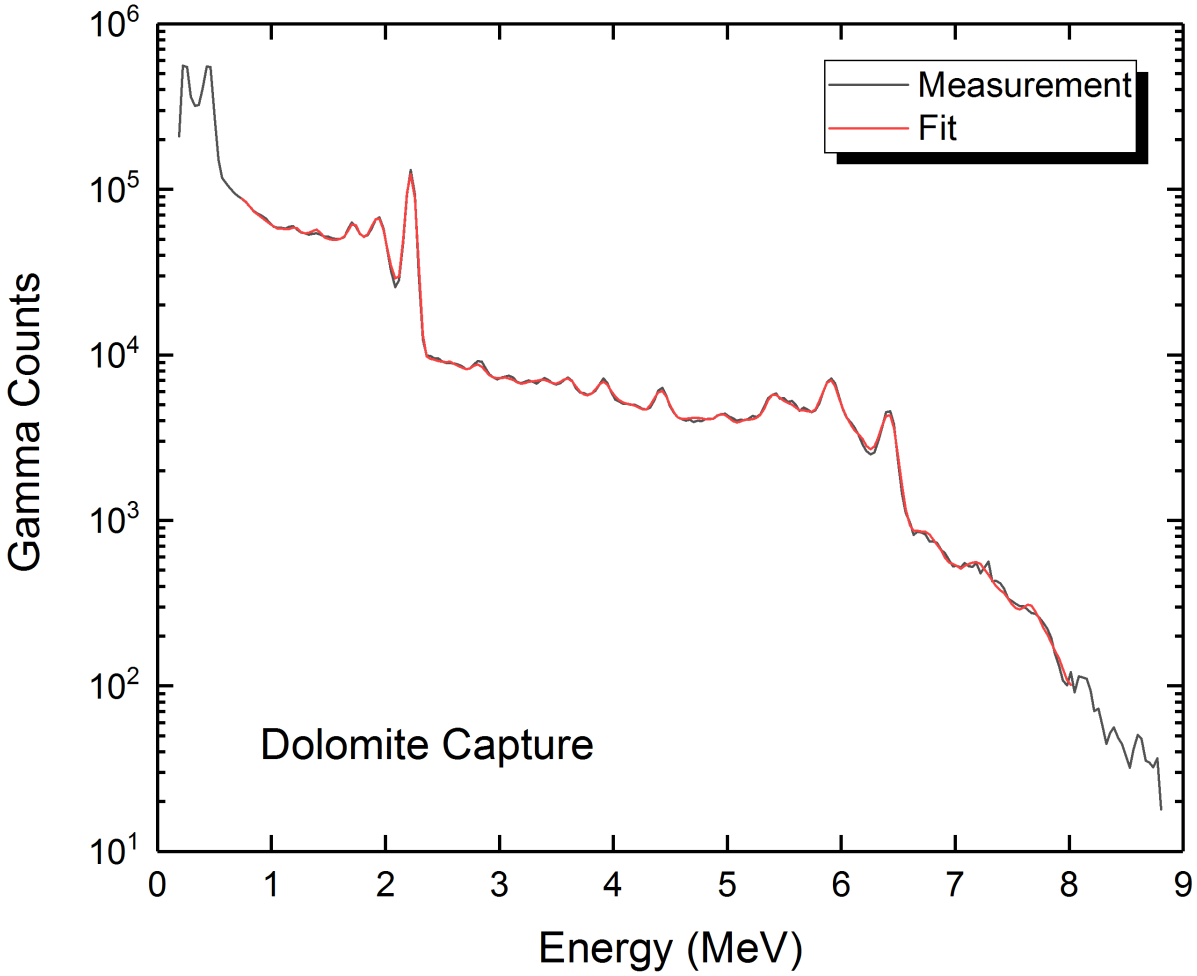

Figure 5.5 Deconvolution of the capture spectrum. Reduced $\chi^2 = 18.3$.

Table 5.3 Calculated capture elemental yields.

Element	Yield
Ca	35.80%
Fe	0.19%
Gd	0.36%
H	56.95%
K	0%
Mg	5.93%
Na	0.55%
S	0.22%
Si	0%
Ti	0%

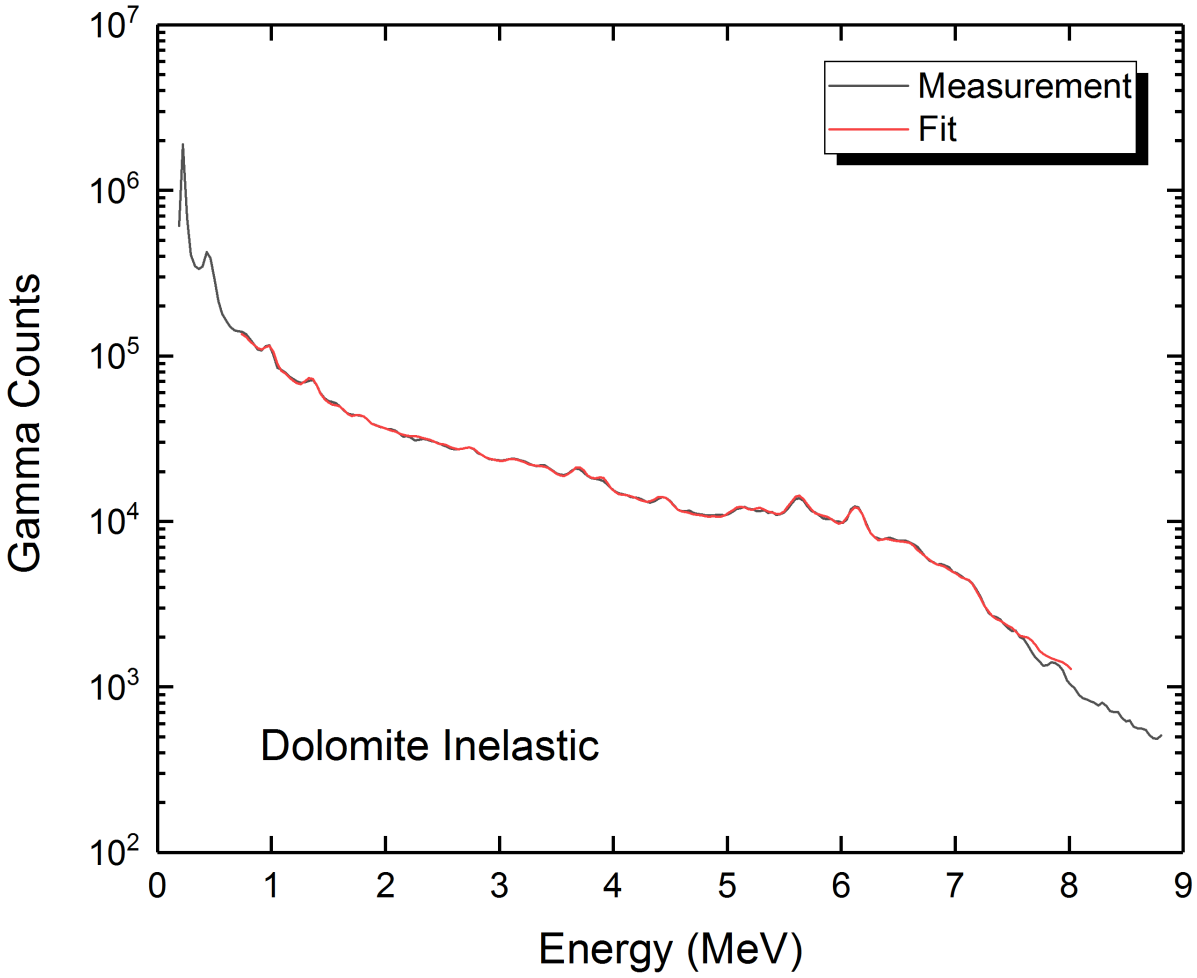

Figure 5.6 Deconvolution of the inelastic spectrum. Reduced $\chi^2 = 13.3$.

Table 5.4 Calculated inelastic elemental yields.

Element	Yield
Al	0%
C	7.40%
Ca	27.24%
Fe	3.73%
Mg	16.44%
O	45.18%

Table 5.5 Elemental concentrations of the formation matrix calculated using the capture standard.

Element	Weight
Ca	20.69%
Fe	0.04%
Gd	0.08 ppm
K	0%
Mg	13.78%
Na	0.18%
S	0.09%
Si	0%
Ti	0%

the inelastic sensitivity factors shown in Figure 4.17, and the oxidation factors listed in Table 4.6, the normalization factor for the inelastic spectrum is calculated to be $F = 0.678$. The elemental dry weights based on the inelastic spectrum, calculated using Equation 4.32, is listed in Table 5.6.

Table 5.6 Elemental concentrations of the formation matrix calculated using the inelastic standard.

Element	Weight
Al	0%
C	11.95%
Ca	24.32%
Fe	2.11%
Mg	11.74%

Finally, averaging the results in Table 5.5 and Table 5.6, obtaining the final results shown in Table 5.7. The results show that the tool is able to resolve majore elements with good accuracy. The tool fails to identify a few elements with low concentrations in the formation. The most significant discrepancy occurs on iron, which is predicted to have 1% concentration in the formation, but actually is only 0.1%. This indicates that the elemental standard of Fe requires further scrutiny.

Table 5.7 Elemental concentrations of the formation matrix averaged over the capture and inelastic spectra.

Element	Weight	XRF	Δ
Al	0%	0.12%	-0.12%
C	11.95%	12.7%	-0.75%
Ca	22.51%	21.7%	0.81%
Fe	1.08%	0.1%	0.98%
Gd	0.08 ppm	0.2 ppm	-0.12 ppm
K	0%	0.09%	-0.09%
Mg	12.76%	12.5%	0.26%
Na	0.18%	0.01%	0.17%
S	0.09%	0.01%	0.08%
Si	0%	0.47%	-0.47%
Ti	0%	0.01%	-0.01%

Chapter 6

Discussion and Conclusions

This dissertation presents research on the development of sensor physics for a nuclear well logging device. The primary focus of this research is on deconvolving the measured spectra, in order to solve for the dry weights of the mineral elements in the formation. This research successfully developed a fitting algorithm that works very well in spectral deconvolution.

The spectral fitting algorithm accounts for gain shifting and resolution degradation. For BGO detectors this is not needed, as the resolution of BGO detector is much worse (about 10% at 662 KeV), and a slight shift is generally not noticeable. However, for $LaBr_3$, the situation is different. The higher resolution necessitates the use of such adjustments.

One advantage of the algorithm developed in this research is that it treats the spectral adjustments parameters as nonlinear parameters, and employs the Levenberg-Marquardt method to fit these parameters. As to the elemental yields, the algorithm treats them as linear parameters, and uses a much faster Non-Negative Least Squares method to solve them. This change considerably accelerates the spectral deconvolution calculations. In the development phase, a typical capture spectral deconvolution involves about 10 elemental standards, and the deconvolution usually has the gain shifting adjustment enabled, and the resolution matching disabled. This makes a total of 12 parameters to fit, including 10 elemental yields and 2 gain shifting parameters. By treating the elemental yields as linear parameters, the algorithm eliminates 5/6 of the model evaluations. This method also avoids requiring initial guesses for the elemental yields, which could range from several ppm to more than 50%.

Currently, the prototype of this algorithm is implemented in Fortran. Throughout the calculations, multiple steps require matrix transposition, multiplication, inversion, and solving systems of linear equations. It is found that, instead of using the intrinsic procedures, using a third party optimized numerical library, such as Intel®MKL, significantly improves the execution efficiency. On a typical modern laptop computer[1], by employing such optimizations, the code is capable of performing more than twenty separate calculations each second, which is more than enough for real time logging analysis.

In the future, this algorithm can be further optimized. The development of this code started with an intention of creating a generic method that could work with any fitting model. One implicit limitation of the code is that, it only accepts $\boldsymbol{X}$, $\boldsymbol{Y}$, $\boldsymbol{\alpha}$ as input, and works towards the direction that minimizes the $\chi^2 = \sum_{i=1}^{n}(y_i - \hat{y}_i(\boldsymbol{X};\boldsymbol{\alpha}))^2/\sigma^2(y_i)$. Specific to the spectral deconvolution model, this means that the gain shifting adjustment parameters have to be applied to each of the elemental standards $\boldsymbol{X}_i$. It is obviously more efficient to apply the gain shifting parameters to the measured spectrum $\boldsymbol{Y}$, and calculate the χ^2 using $\chi^2 = \sum_{i=1}^{n}(y_i(\boldsymbol{\alpha}) - \hat{y}_i(\boldsymbol{X};\boldsymbol{\beta}))^2/\sigma^2(y_i(\boldsymbol{\alpha}))$, where $\boldsymbol{\alpha}$ is the spectral adjustments parameter vector, and $\boldsymbol{\beta}$ is the elemental coefficient vector.

Another critical component to the spectral deconvolution are the elemental standards. As of now, a set of standards have already been created empirically for testing. Another set modeled using MCNP is also available for benchmarking purpose. Tests with the empirical set have been mostly successful, with some problems with elements that are not abundant in the sample being overestimated or underestimated. This is likely caused by the lack of attention to the less abundant elements when creating the standards. For example, the sandstone formation, which is used for creating the Si standard, was shown by core analysis to contain 0.81% Al. Currently, the capture Si standard is obtained by simply taking a capture spectrum of the sample, and subtracting the hydrogen contribution. The Si standard created using this method inherently includes a small fraction of Al contribution. If the rock formation to be deconvolved is dominated by Si and contains a small amount of Al, the Al fraction may or may not be resolved correctly. In the future, it is planned to have the elemental standards fine tuned to correct the inclusions of impurities.

A set of sensitivity factors has also been constructed. As the elemental standards change, the sensitivity factors may also change in the future. The measurements of

[1]In the year of 2017.

sensitivity factors are straightforward, and primarily rely on a good deconvolution method and a good set of elemental standards.

Another plan for the future work concerns the measurement precision. As of now, the measurements made are for experimental purposes, and include stationary measurements for various samples. Each sample has been measured long enough that the statistics of the measurement is not an issue. In the field application, this is no longer true. At the fastest designed logging speed, the Tool dwells at each measurement depth for only a matter of seconds, and the measured spectrum may need to be averaged with the adjacent measurements. This slightly changes the counting statistics, and the Poisson statistics assumption $\sigma(y) \approx \sqrt{y}$ is no longer true. A separate subroutine needs to be developed to weigh in the averaging, and to calculate the $\sigma(y)$ for calculating χ^2 correctly.

BIBLIOGRAPHY

[1] O. Serra. *Fundamentals of well-log interpretation, 1. The acquisition*. Elsevier Science Publishers, 1984.

[2] R. Hertzog, L. Colson, O. Seeman, et al. "Geochemical Logging With Spectrometry Tools". In: *SPE Formation Evaluation* 4.02 (June 1989), pp. 153–162.

[3] F. Zhang, J. Liu, X. Ji, et al. "Development of Formation Element Logging Technique and Its Application". In: *Journal of Isotopes* 24.Suppl. (2011), pp. 21–28.

[4] M. M. Herron. "Mineralogy from Geochemical Well Logging". In: *Clays and Clay Minerals* 34.2 (1986), pp. 204–213.

[5] R. R. Pemper, A. Sommer, P. Guo, et al. "A New Pulsed Neutron Sonde for Derivation of Formation Lithology and Mineralogy". In: *SPE Annual Technical Conference and Exhibition*. Society of Petroleum Engineers, Apr. 2006.

[6] J. Galford, J. Truax, A. Hrametz, et al. "A New Neutron-Induced Gamma-Ray Spectroscopy Tool For Geochemical Logging". In: *SPWLA 50th Annual Logging Symposium*. 2009.

[7] R. J. Radtke, M. Lorente, B. Adolph, et al. "A new capture and inelastic spectroscopy tool takes geochemical logging to the next level". In: *SPWLA 53rd Annual Logging Symposium*. 2012.

[8] E. V. D. Van Loef, P. Dorenbos, C. W. E. Van Eijk, et al. "High-energy-resolution scintillator: Ce3+ activated LaBr3". In: *Applied Physics Letters* 79.10 (Sept. 2001), pp. 1573–1575.

[9] C. Stoller, B. Adolph, M. Berheide, et al. "Use of LaBr 3 for downhole spectroscopic applications". In: *2011 IEEE Nuclear Science Symposium Conference Record*. IEEE, Oct. 2011, pp. 191–195.

[10] G. F. Knoll. *Radiation Detection and Measurement*. 4th Editio. John Wiley & Sons, Inc, 2011.

[11] X. Han. "Development of Monte Carlo Code for Coincidence Prompt Gamma-ray Neutron Activation analysis". PhD thesis. North Carolina State University, 2005.

[12] R. D. Evans. *The Atomic Nucleus*. McGraw-Hill, 1955.

[13] M. Shamsuzzoha Basunia. "Nuclear data sheets for A = 28". In: *Nuclear Data Sheets* 114.10 (Oct. 2013), pp. 1189–1291.

[14] M. Chadwick, M. Herman, P. Obložinský, et al. "ENDF/B-VII.1 Nuclear Data for Science and Technology: Cross Sections, Covariances, Fission Product Yields and Decay Data". In: *Nuclear Data Sheets* 112.12 (Dec. 2011), pp. 2887–2996.

[15] X-5 Monte Carlo Team. *MCNP - A General Monte Carlo N-Particle Transport Code, Version 5*. Tech. rep. Los Alamos National Laboratory, 2005.

[16] J. K. Shultis and R. E. Faw. *An MCNP Primer*. 2011.

[17] *Scintillation Materials and Assemblies*. Tech. rep. Saint-Gobain Ceramics & Plastics, Inc., 2016.

[18] J. Wang, Z. Wang, J. Peeples, et al. "Development of a simple detector response function generation program: The CEARDRFs code". In: *Applied Radiation and Isotopes* 70.7 (July 2012), pp. 1166–1174.

[19] *Database of Prompt Gamma Rays from Slow Neutron Capture for Elemental Analysis*. Tech. rep. International Atomic Energy Agency, 2007.

[20] R. C. Reedy and S. C. Frankle. "Prompt Gamma Rays From Radiative Capture of Thermal Neutrons By Elements From Hydrogen Through Zinc". In: *Atomic Data and Nuclear Data Tables* 80.1 (Jan. 2002), pp. 1–34.

[21] J. K. Tuli. "Evaluated nuclear structure data file". In: *Nuclear Instruments and Methods in Physics Research, Section A: Accelerators, Spectrometers, Detectors and Associated Equipment* 369.2-3 (Feb. 1996), pp. 506–510.

[22] M. R. Ahmed, S. Al-Najjar, M. A. Al-Amili, et al. *Atlas of Gamma-ray Spectra from the Inelastic Scattering of Reactor Fast Neutrons*. Tech. rep. Moscow Atomizdat, 1978.

[23] D. E. Cullen. *PREPRO 2015, ENDF/B Pre-processing Codes*. Tech. rep. International Atomic Energy Agency, 2015.

[24] D. E. Cullen, J. H. Hubbell, and L. Kissel. *EPDL97: The Evaluated Photon Data Library '97 Version*. Tech. rep. Livermore, CA: Lawrence Livermore National Laboratory (LLNL), Sept. 1997.

[25] M. Berger, J. Hubbell, S. Seltzer, et al. *XCOM: Photon Cross Section Database*. Tech. rep. Gaithersburg, MD: National Institute of Standards and Technology, 2010.

[26] *Neutron Generators for Analytical Purposes*. Tech. rep. International Atomic Energy Agency, 2012, p. 145.

[27] G. H. Miley, J. Javedani, Y. Yamamoto, et al. "Inertial-Electrostatic Confinement Neutron/Proton Source". In: *AIP Conference Proceedings*. AIP, 1994, pp. 675–689.

[28] *BrilLanCe Scintillators Performance Summary*. Tech. rep. Saint-Gobain Ceramics & Plastics, 2009.

[29] F. G. A. Quarati, I. V. Khodyuk, C. W. E. Van Eijk, et al. "Study of 138La radioactive decays using LaBr 3 scintillators". In: *Nuclear Instruments and Methods in Physics Research, Section A: Accelerators, Spectrometers, Detectors and Associated Equipment* 683 (2012), pp. 46–52.

[30] R. P. Gardner and A. Sood. "A Monte Carlo simulation approach for generating NaI detector response functions (DRFs) that accounts for non-linearity and variable flat continua". In: *Nuclear Instruments and Methods in Physics Research, Section B: Beam Interactions with Materials and Atoms* 213 (Jan. 2004), pp. 87–99.

[31] A. Sood and R. P. Gardner. "A new Monte Carlo assisted approach to detector response functions". In: *Nuclear Instruments and Methods in Physics Research, Section B: Beam Interactions with Materials and Atoms* 213 (Jan. 2004), pp. 100–104.

[32] R. Forster, L. J. Cox, R. F. Barrett, et al. "MCNP Version 5". In: *Nuclear Instruments and Methods in Physics Research Section B: Beam Interactions with Materials and Atoms* 213 (Jan. 2004), pp. 82–86.

[33] R. Hertzog. "Laboratory and Field Evaluation of an Inelastic Neutron Scattering and Capture Gamma Ray Spectrometry Tool". In: *Society of Petroleum Engineers Journal* 20.05 (Oct. 1980), pp. 327–340.

[34] R. R. Pemper, M. J. Flecker, V. C. McWhirter, et al. "Hydraulic fracture evaluation with multiple radioactive tracers". In: *Geophysics* 53.10 (Oct. 1988), pp. 1323–1333.

[35] H. P. Gavin. *The Levenberg-Marquardt method for nonlinear least squares curve-fitting problems*. 2017.

[36] C. L. Lawson and R. J. Hanson. *Solving Least Squares Problems*. May 2012. Society for Industrial and Applied Mathematics, Jan. 1995.

[37] P. R. Bevington and D. K. Robinson. *Data reduction and error analysis for the physical sciences*. McGraw-Hill, 1969.

[38] H. B. Nielsen. *Damping Parameter in Marquardt's Method*. Tech. rep. IMM, 1999.

[39] R. P. Gardner and C. W. Mayo. "NaI detector nonlinearity for PGNAA applications". In: *Applied Radiation and Isotopes* 51.2 (Aug. 1999), pp. 189–195.

[40] W. Wu, A. Yue, M. Tong, et al. "The calculation and characteristic of elemental sensitivity factor in geochemical logging". In: *Petroleum Geoscience* 21.1 (Feb. 2015), pp. 74–80.